Aspects of Constraining Dark Energy

A Dissertation Presented

by

Jonathan Gordon

to

The Graduate School

in Partial Fulfillment of the Requirements

for the Degree of

Doctor of Philosophy

in

Physics

Stony Brook University

December **2024**

Stony Brook University

The Graduate School

Jonathan Gordon

We, the dissertation committee for the above candidate for the Doctor of Philosophy degree, hereby recommend acceptance of this dissertation.

Vivian Miranda – Dissertation Advisor
Assistant Professor, Yang Institute of Theoretical Physics

George Sterman – Chairperson of Defense
Distinguished Professor, Yang Institute of Theoretical Physics

Neelima Sehgal
Associate Professor, Department of Physics and Astronomy

Hans Winther
Associate Professor
Institute of Theoretical Astrophysics, University of Oslo

This dissertation is accepted by the Graduate School.

Celia Marshik
Dean of the Graduate School

Abstract of the Dissertation

Aspects of Constraining Dark Energy

by

Jonathan Gordon

Doctor of Philosophy

in

Physics

Stony Brook University

2024

In this thesis, I discuss aspects of constraining cosmological models beyond the Λ Cold Dark Matter (ΛCDM) framework, with data. Despite the success of ΛCDM in providing a close fit to a variety of datasets, inconsistencies have arisen as the precision of cosmological experiments has evolved. Most notably, determination of the Hubble constant H_0 from the Cosmic Microwave Background (CMB) assuming the ΛCDM model produces a value 5σ lower than indicated by local measurements, suggesting the possibility of new physics. Less well-known is the S_8 tension, in which large-scale structure (LSS) measurements yield a value up to 3σ lower than the CMB under ΛCDM.

While systematics of the experiments are a possible explanation for such tensions, another appealing avenue of research is to explore alternative models to ΛCDM that may correct the inference of cosmological parameters from data. The idea of Early Dark Energy (EDE) was proposed for this purpose. The EDE model posits that a source of energy was present in the period immediately preceding recombination, before rapidly dissipating. This additional energy

lowers the inferred size of the sound horizon from CMB data, increasing the measurement of H_0. However, analyses of the EDE model have suggested that while it can alleviate the H_0 tension, it can also exacerbate the S_8 tension. Therefore, this thesis begins with an exploration of whether the combination of early and late dark energy can restore cosmological concordance, by marginalizing over the behavior of a smooth late dark energy.

Although there are a variety of appealing beyond-ΛCDM models, the majority of them lack a fast and accurate prescription to predict observables from the cosmological parameters of the model on small scales where linear perturbation theory is not valid. With the next generation of Stage IV LSS surveys beginning to release data deeper into this nonlinear regime than ever before, modeling tools must be enhanced to meet the challenge. Therefore, the second part of this thesis tests one proposed prescription to generate fast predictions of the nonlinear matter power spectrum. In particular, I test the Co-moving Lagrangian Acceleration (COLA) method as a means of generating training sets for an emulator, which I use in an LSST-Y1 simulated cosmic shear analysis. I perform this test using the wCDM model, a minimal extension to ΛCDM, for which high-resolution N-body simulation benchmarks exist and can be used to assess performance.

Contents

List of Figures **vii**

Acknowledgements **x**

1 Introduction **1**
1.1 General Relativity and the FLRW Metric 1
1.2 Standard Model of Cosmology 4
1.3 Basic Extensions to ΛCDM 5
1.4 Distances 7
1.5 Eulerian Perturbation Theory 8
1.5.1 Scalar, Vector, Tensor Decomposition 9
1.5.2 Gauges 12
1.6 Lagrangian Perturbation Theory 16
1.7 Observables 19
1.7.1 Supernovae 19
1.7.2 Cosmic Microwave Background 21
1.7.3 Large Scale Structure 24
1.8 Tensions in ΛCDM 31
1.8.1 The Hubble Tension 31
1.8.2 The S_8 Tension 33

2 Computational Tools **36**
2.1 Bayesian Inference and MCMCs 36
2.2 N-body Simulations 39
2.2.1 Algorithms and Techniques 40
2.2.2 COLA simulations 42
2.3 Emulators of the Power Spectrum 43
2.3.1 Pre-processing 44
2.3.2 Gaussian Process Regression 46

3 Early Dark Energy with Late-Time Marginalization **48**
3.1 Dark Energy Models 49
3.2 Datasets 51
3.3 Analysis 52
3.4 Results 53
3.4.1 Early Dark Energy Only 53
3.4.2 Adding Late-Time Modifications 56

4 Nonlinear modeling with COLA **61**
4.1 Post-Processing COLA 65
4.2 Comparisons to EE2 at the Boost Level: 1, 26, 101 references 67
4.3 Emulator Validation 69
4.4 Analysis of LSST-Y1 Simulated Data 72
4.5 Results of Simulated LSST-Y1 Analysis for $N_{\rm refs} = 1, 26, 101$. 74
4.6 Emulating $B_{\rm COLA}(k, z)$: $N_{\rm refs}^{\Lambda{\rm CDM}} = 500, \infty$ 79

5 Conclusion **84**

Bibliography **87**

List of Figures

1.1 The temperature power spectrum from Planck 2018 [1]. Here $\mathcal{D}_\ell^{TT} \equiv \frac{\ell(\ell+1)}{2\pi} C_\ell^{TT}$ are plotted in the top panel, and their residuals $\Delta\mathcal{D}_\ell^{TT}$ relative to their best-fit. 23

1.2 Compilation of various H_0 constraints published between 2012-2021, taken from [2]. The cyan band is the 2020 SH0ES constraint from [3], and the pink band is the 2018 Planck constraint [1]. 32

1.3 Compilation of various S_8 constraints from CMB and LSS probes, taken from [4]. 34

2.1 Comparison between the linear and nonlinear matter power spectrum at $z = 0$ for a ΛCDM cosmology. The linear solution underestimates power on small scales. 40

3.1 ΛCDM and EDE only constraints, when using DC1 and DES-Y3 datasets. 55

3.2 The 1D tension metric of Eq. 3.9 under different models, relative to the SH0ES H_0 constraint, and the DES-Y3 S_8 constraint. Under DC1, EDE models lower the H_0 tension to less than 1, while slightly increasing the S_8 tension. However, when DES-Y3 cosmic shear data is added, the S_8 tension lowers slightly at the cost of a lesser reduction in the H_0 tension. 56

3.3 Histograms of $\chi^2_{\rm CMB}$ showing the goodness-of-fit of EDE with modified late-time behavior to the CMB. 57

3.4 Mean and 68% bounds on H_0, S_8, Ω_m, and $f_{\rm EDE}$ using a fluid EDE model with modified late-time behavior $w(z)$. We use datasets DC1 and DC2, and repeat the analysis with DES-Y1 and DES-Y3 cosmic shear and 3x2pt data. 59

3.5 Continuation of Fig. 3.4 using the DC3, DC4, and DC5 datasets. 60

4.1 Bounds on the lowest error 50%, 90%, and 100% of training simulations, computed at $z = 0$ and each wavenumber k. The error is evaluated as the fractional difference between the post-processed boosts from the COLA simulations and the boosts from EE2. Each panel is identified by the cosmological model in which the simulations span, the precision settings, and the number of references, with the left panels corresponding to $N_{\rm refs} = 1$. 69
4.2 Emulation errors at $z = 0$ for our DP simulations with $N_{\rm refs} = 1$. We test three different emulation methods GP, NN, and PCE, while also comparing the effect of using the BAO-smearing procedure of the BACCO emulator. 70
4.3 Emulation errors at $z = 0$ for our EP simulations with $N_{\rm refs} = 1$. The emulation errors reach about $\sim 1\%$ at $k = 1h{\rm Mpc}^{-1}$, an increase compared to the $\sim 0.5\%$ error in the DP case in Fig. 4.2 for GP, NN, and PCE emulators. However, the NPCE method appears to recover the lower errors. 71
4.4 2D contours comparing the DP $N_{\rm refs} = 1$ COLA emulator and EE2 parameter constraints, applying the most aggressive Cutoff 3. In the left panel the fiducial cosmology is equal to the reference cosmology of the emulator, while in the right panel the fiducial cosmology has shifted parameters $(\Omega_m^{\uparrow}, A_s^{\uparrow})$ leading to a value of $\sigma_8 = 0.93$ much higher than the reference $\sigma_8 = 0.82$. 75
4.5 1D biases using the DP $N_{\rm refs} = 1$ emulator, computed for a variety of fiducial cosmologies and all three scale cuts tested in this project. Fiducial cosmologies are ordered by value of σ_8, showing a clear correlation with bias. 76
4.6 1D biases for selected fiducial cosmologies with high Ω_m. The top panel displays the biases of the emulators trained on DP and EP settings, while the bottom panel displays the biases from the two multiple reference emulators with $N_{\rm refs}^{w{\rm CDM}} = 26$ and $N_{\rm refs}^{\Lambda{\rm CDM}} = 101$. 77
4.7 1D biases for the $N_{\rm refs}^{w{\rm CDM}} = 26$ and $N_{\rm refs}^{\Lambda{\rm CDM}} = 101$ emulators for fiducial cosmologies outside of the ΛCDM region. These tests are intended to assess whether the previous results showing lower bias from the $N_{\rm refs}^{\Lambda{\rm CDM}} = 101$ emulator were due to an unfair advantage produced by placing the fiducial cosmologies inside ΛCDM. 79

4.8 Repeating the comparisons shown in Fig. 4.1 between boosts from the post-processed COLA simulations and EE2 at $z = 0$, now using the $N_{\rm refs}^{\Lambda{\rm CDM}} = 500$ and $N_{\rm refs}^{\Lambda{\rm CDM}} = \infty$ approaches. The COLA boost for $N_{\rm refs}^{\Lambda{\rm CDM}} = 500$ is computed using $\tilde{B}(k, z)$ (Eq. 4.3) while for $N_{\rm refs}^{\Lambda{\rm CDM}} = \infty$ it is computed as $\bar{B}(k, z)$ (Eq. 4.9). For these comparisons the COLA boosts at the references are emulated. 80
4.9 1D biases using the $N_{\rm refs}^{\Lambda{\rm CDM}} = 500$ and $N_{\rm refs}^{\Lambda{\rm CDM}} = \infty$ methods at some of the most biased fiducial cosmologies from previous tests. 81

Acknowledgements

First and foremost, I want to thank my extended family and friends for their unwavering support and for always having my back. I am especially grateful to my parents for working tirelessly to provide me with the best opportunities and for pushing me to strive toward becoming a better version of myself. I also thank my sisters for their constant support and encouragement. I'd like to pay tribute to my brother Sean-Paul as well, who was such an integral part of my upbringing. Though he did not get to see me complete this journey, I carry his memory every day.

I must also thank all of the educators that have guided me towards, and through, this degree. I could not do so without thanking my advisor Vivian Miranda, who gave me an opportunity when I was new to the field and worked with me through rough pandemic times. I thank her not only for all of her close collaboration and mentorship these past three years, but also for the resources and opportunities she provided for myself and other students to attend conferences and further our development.

Just as important to my progress were the students I collaborated with these past years. I thank João Rebouças, Diogo Souza, Lucas Faga, Kunhao Zhong, Evan Saraivanov, Bernardo F. de Aguiar, Huangfei Xiao, Yijie Zhu, Mark Vincent Guevarra, Victoria Lloyd, and many others, for helpful conversations and insights. I must also thank the postdocs, Joshua Kable and Guilherme Brando, for playing key roles in deepening my understanding of many topics. While completing this thesis will ascend me to post-doctoral nirvana as well, I will still be very far from sharing their hard-earned expertise. I particularly have to thank Gui, as well as Felipe Falciano and Bruno Moraes, for hosting me in Rio de Janeiro, the consequences of which include my current intermediate proficiency in Portuguese.

There are a number of other members of the university whose work has helped me succeed here at Stony Brook, including Donald Sheehan, Dawn Huether, Helen Carrano, Brett Kaplan, Richard Lefferts, Bent Nielsen, the SeaWulf team, and many others.

Chapter 1

Introduction

1.1 General Relativity and the FLRW Metric

The development of Einstein's theory of General Relativity in 1915 revolutionized the study of cosmology. General Relativity provided a geometric description of gravity, redefining it as the curvature of spacetime, shaped by the distribution of mass and energy. This theory challenged the Newtonian notion of a static Universe, instead positing that the Universe is inherently dynamical, having profound implications for cosmology.

In General Relativity, the geometry of spacetime determines the motion of particles and light. If we parameterize their paths with some affine parameter $\lambda \in [0, 1]$, the proper time τ along the path is then represented by:

$$\tau = \int_0^1 \sqrt{-g_{\mu\nu} \frac{dx^\mu}{d\lambda} \frac{dx^\nu}{d\lambda}} d\lambda. \tag{1.1}$$

Here $g_{\mu\nu}$ is called the metric tensor which encapsulates the geometry of spacetime and determines how distances are measured. Extremal paths in this geometry are then determined by varying Eq. 1.1 with respect to the coordinates $x^\mu(\lambda)$, giving the equation:

$$\frac{d^2x^\mu}{d\lambda^2} + \Gamma^\mu_{\rho\sigma} \frac{dx^\rho}{d\lambda} \frac{dx^\sigma}{d\lambda} = 0. \tag{1.2}$$

This is known as the geodesic equation and it determines the trajectories of freely moving particles and light, that is, subject only to the influence of gravity.

While the geodesic equation determines how particles move within a given spacetime, we now consider how matter and energy determine the geometry

of spacetime. This is provided by the Einstein field equation, the centerpiece of the theory:

$$G_{\mu\nu} + \Lambda g_{\mu\nu} = \frac{8\pi G}{c^4} T_{\mu\nu}. \tag{1.3}$$

Here, $G_{\mu\nu}$, $T_{\mu\nu}$ are the Einstein and energy-momentum tensors respectively, and we also have the cosmological constant Λ, the speed of light c, and the gravitational constant G. While the left hand side of the equation relates to the geometry of spacetime, the right hand side encodes information about its energy contents.

As in many areas of physics, it is useful to first study the Einstein equation in an idealized scenario. In this case, we assume that the Universe is homogeneous and isotropic. These assumptions are expected to be a closer approximation to reality on the larger scales of the Universe, a rationale referred to as the Cosmological Principle. The most general form of the metric tensor which accommodates these properties is the Friedmann–Lemaître–Robertson–Walker (FLRW) metric:

$$ds^2 = -dt^2 + a^2(t)\Big[\frac{dr^2}{1 - kr^2/R_0^2} + r^2 d\Omega^2\Big], \tag{1.4}$$

where $k \in \{-1, 0, 1\}$ is a dimensionless parameter that sets the geometry of the spatial slices, and R_0 sets the scale of the curvature. The spatial dimensions are scaled by a function of time, called the scale factor $a(t)$. I have also set the speed of light $c = 1$, and will maintain this throughout the rest of the text. Eq. 1.4 is equivalent under a simultaneous rescaling by a constant λ: $a \to \lambda a$, $r \to r/\lambda$, and $R_0 \to R_0/\lambda$. This allows us to set the scale factor today to $a(t_0) = 1$, which gives R_0 the interpretation of the curvature scale today. We will use the subscript 0 to denote any quantity evaluated today.

It is sometimes insightful to define new variables so that we may rewrite the metric. There is the conformal time, defined by:

$$d\eta \equiv \frac{dt}{a(t)}, \tag{1.5}$$

and the comoving radial component:

$$d\chi \equiv \frac{dr}{\sqrt{1 - kr^2/R_0^2}}. \tag{1.6}$$

The line element in Eq 1.4 can then be written as:

$$ds^2 = a^2(\eta)\big[-d\eta^2 + (d\chi^2 + S_k^2(\chi) d\Omega^2)\big], \tag{1.7}$$

where

$$S_k(\chi) \equiv R_0 \times \begin{cases} \sinh(\chi/R_0) & \text{if } k = -1 \text{ (open universe)}, \\ \chi/R_0 & \text{if } k = 0 \text{ (flat universe)}, \\ \sin(\chi/R_0) & \text{if } k = 1 \text{ (closed universe)}. \end{cases}$$

The metric in Eq. 1.7 is now factorized into a static portion, and the time-dependent $a(\eta)$.

The properties of isotropy and homogeneity also imply that the energy-momentum tensor of a given matter species should be that of a perfect fluid:

$$T_{\mu\nu} = (\rho(t) + P(t))u_\mu u_\nu + P(t)g_{\mu\nu}, \tag{1.8}$$

where u is the 4-velocity of the fluid, $P(t)$ is the pressure, and $\rho(t)$ is the energy density. The energy-momentum tensor for each species of matter is conserved $\nabla^\mu T_{\mu\nu} = 0$, yielding the continuity equation for a particular species of matter:

$$\dot{\rho}_i + 3H(\rho_i + P_i) = 0. \tag{1.9}$$

Here $H(t) \equiv \frac{\dot{a}}{a}$ is called the Hubble parameter and is fundamental in tracking the expansion of the Universe. We can also write the continuity equation in conformal time:

$$\frac{d\rho_i}{d\eta} + 3\mathcal{H}(\rho_i + P_i) = 0, \tag{1.10}$$

where $\mathcal{H} \equiv \frac{1}{a}\frac{da}{d\eta}$ is the *conformal* Hubble parameter.

Eq. 1.9 can be solved by proposing a relationship between the energy density and pressure. This is accomplished by defining the following parameter $w_i \equiv P_i/\rho_i$, called the equation of state parameter, which is taken to be constant for many energy species. From this we obtain the result that the energy density of the species changes over time via the relationship:

$$\rho_i(t) \propto a^{-3(1+w_i)}. \tag{1.11}$$

With the form of the metric and energy-momentum tensors now specified, the Einstein field equation (Eq. 1.3) relates their components. The Einstein equation also gives rise to what are known as the Friedmann equations, though they are not both independent of Eq. 1.9:

$$H^2(t) = \frac{8\pi G}{3}\rho_{\text{tot}}(t) - \frac{k}{a^2 R_0^2}, \tag{1.12}$$

$$\frac{\ddot{a}}{a} = -\frac{4\pi G}{3}(\rho_{\text{tot}}(t) + 3P(t)), \tag{1.13}$$

where $\rho_{\rm tot}(t)$ is now the total energy density of all species combined. Though our universe is not homogeneous or isotropic, these equations capture the essence of the dynamics of an expanding universe and provide many important insights. From the first Friedmann equation it can be seen that a flat Universe where $k = 0$, is achieved with a critical value of the density $\rho_{\rm crit} = \frac{3H^2}{8\pi G}$. In particular, today $\rho_{\rm crit,0} = \frac{3H_0^2}{8\pi G}$ where the Hubble constant $H_0 \equiv H(t_0)$ is the Hubble parameter today. The energy density of each species can then be normalized by the critical density:

$$\Omega_i \equiv \frac{\rho_i}{\rho_{\rm crit}}. \tag{1.14}$$

We see that in a flat Universe the sum over the various species gives $\sum_i \Omega_i = 1$, and it is common to define the curvature density parameter $\Omega_k \equiv 1 - \sum_i \Omega_i$. Using Eq. 1.12, this implies $\Omega_k = -\frac{k}{a^2 R_0^2 H^2}$ which scales as a^{-2}.

1.2 Standard Model of Cosmology

In the Friedmann equations the dynamics of the universe depend on the total energy density, hence it is essential to consider the particular species of matter and energy present in a given cosmological model. The ΛCDM model is considered the Standard Model of cosmology, providing a good fit to a variety of datasets with only 6 free parameters. It posits that the Universe is comprised of these primary species:

- Cold Dark Matter (CDM): A non-relativistic form of matter which does not interact with electromagnetic radiation. Plays a critical role in the formation of large-scale structure.
- Baryons: Ordinary matter made up of protons, neutrons, electrons, which comprise atoms, and hence stars and galaxies.
- Radiation: Relativistic particles such as photons or neutrinos in the early Universe.
- Neutrinos: Light, weakly-interacting particles. In the early Universe they behaved relativistically. However, due to their nonzero mass, as the Universe cooled they transitioned to non-relativistic behavior, influencing the growth of structure.
- Dark Energy (Λ): Modeled as a constant form of energy density filling all of space, causing the accelerated expansion of the Universe.

I will use the subscripts $i = c, b, \gamma, \nu, \Lambda$ to denote these species respectively. Eq. 1.11 shows that the energy density of a species decays more quickly over time with a larger value of the equation of state parameter. The largest equation of state parameter among the aforementioned species occurs for radiation, which has $w_\gamma = \frac{1}{3}$ so that $\rho_\gamma(t) \propto a^{-4}$. This implies that at a sufficiently early epoch radiation was the most abundant species, called the era of radiation domination.

Baryonic matter and cold dark matter both are characterized by a pressure much lower than their energy density $|P| << \rho$ so that we set $w_b = w_c = 0$. Hence, by Eq. 1.11 their energy density decreases over time as $\rho_m(t) \propto a^{-3}$ where the subscript m refers to any species of matter which has a vanishing equation of state parameter. Therefore, once the radiation energy density dissipates the Universe enters the era of matter domination where matter is the most abundant species.

Finally, from Eq. 1.11 it can be seen that a constant form of energy density has equation of state $w_\Lambda = -1$. Once the matter energy density declines such a constant form of dark energy becomes the most abundant species bringing the Universe into an era of dark energy domination, which we are in today. The notion of a nonzero vacuum energy also arises in Quantum Field Theory, however it predicts an energy density $\mathcal{O}(10^{60})$ times greater than modern cosmological measurements indicate [5], leading to a crisis that is known as the cosmological constant problem.

1.3 Basic Extensions to ΛCDM

In this section, I briefly discuss some minor extensions to the ΛCDM model which will be mentioned in later chapters. One simple extension is the wCDM model, where dark energy is taken to be a perfect fluid with an equation of state $w_{\rm DE}$ that is constant, but is allowed to vary from -1. Therefore, the dark energy density no longer remains constant over time, but evolves as:

$$\rho_{\rm DE}(t) \propto a^{-3(1+w_{\rm DE})}. \tag{1.15}$$

Hence, for $w_{\rm DE} > -1$ dark energy decays over time, but for $w_{\rm DE} < -1$ it would increase over time, called phantom dark energy.

This model can be further extended by allowing for a dynamical equation of state which varies over time. A common example is the $w_0 w_a$ model [6, 7], where the dark energy equation of state is parameterized by:

$$w_{\rm DE}(a) = w_0 + w_a(1 - a). \tag{1.16}$$

Therefore, in the early universe where $a \to 0$ dark energy has an equation of state $w_0 + w_a$, which then transitions to w_0 by today. From Eq. 1.9, the dark energy density under this parameterization evolves as:

$$\rho_{\rm DE}(t) \propto a^{-3(1+w_0+w_a)} e^{-3w_a(1-a)}. \tag{1.17}$$

Another interesting class of dark energy models are the quintessence models, in which dark energy is modeled as a canonical scalar field, $\phi(\boldsymbol{x}, t)$, which interacts with other matter constituents only through gravity. The Lagrangian density for the field is:

$$\mathcal{L}_\phi = -\frac{1}{2} g^{\mu\nu} \partial_\mu \phi \partial_\nu \phi - V(\phi), \tag{1.18}$$

where $V(\phi)$ is the potential energy density. The energy-momentum tensor of the quintessence field is then obtained by varying the action with respect to the metric:

$$T^{(\phi)}_{\mu\nu} = -\frac{2}{\sqrt{-g}} \frac{\delta(\sqrt{-g}\mathcal{L}_\phi)}{\delta g^{\mu\nu}} \tag{1.19}$$

$$= \partial_\mu \phi \partial_\nu \phi - g_{\mu\nu} \left[\frac{1}{2} g^{\rho\sigma} \partial_\rho \phi \partial_\sigma \phi + V(\phi) \right]. \tag{1.20}$$

We then can obtain the energy density and pressure of the quintessence field by:

$$\rho_\phi = -T^{0(\phi)}_0 = \frac{1}{2}\dot{\phi}^2 + V(\phi), \tag{1.21}$$

$$P_\phi = \frac{1}{3} T^{i(\phi)}_i = \frac{1}{2}\dot{\phi}^2 - V(\phi). \tag{1.22}$$

The equation of state of dark energy is then:

$$w_\phi \equiv \frac{P_\phi}{\rho_\phi} = \frac{\dot{\phi}^2 - 2V(\phi)}{\dot{\phi}^2 + 2V(\phi)}. \tag{1.23}$$

The continuity equation (Eq. 1.9) for this field along with Eqs. 1.21-1.22 can be combined to yield the Klein-Gordon equation for the scalar field:

$$\ddot{\phi} + 3H\dot{\phi} + V_{,\phi} = 0, \tag{1.24}$$

where $V_{,\phi} \equiv \mathrm{dV}/\mathrm{d}\phi$. This can also be obtained by varying the action with respect to ϕ. The $\dot{\phi}$ term is known as the Hubble friction, slowing the evolution

of the field as the universe expands.

In order for the scalar field energy density to become appreciable at late times, it is common to seek potentials that allow the scalar field energy density to track the density of another matter species. For this behavior, the potential must not be too steep, otherwise $\dot{\phi}^2 >> V(\phi)$ and $w_\phi \approx 1$ which leads to a decay much faster than matter $\rho_\phi \propto a^{-6}$. To achieve late time acceleration, we must have $w_\phi < -1/3$, which by Eq. 1.23 implies $\dot{\phi}^2 < V(\phi)$. Scalar fields can also be used to realize inflation, as well as dark energy that is more appreciable at earlier times, discussed more in Sec. 3.1.

1.4 Distances

Inferring distances in cosmology is essential for understanding the structure and history of the Universe. However, this procedure is complicated due to the expansion of the Universe, relativity, and the finite time required for light to reach an observer. First, let us consider how the expansion of the Universe affects the light we measure. If light is emitted from a source at time t_1 and observed today at time t_0, the Universe will have expanded by a factor $a(t_0)/a(t_1)$, or $1/a(t_1)$ using $a(t_0) = 1$. Then the wavelength of the light will have been stretched by the same amount, which we quantify with the redshift parameter z:

$$1 + z \equiv \frac{\lambda_0}{\lambda_1} = \frac{1}{a(t_1)}. \tag{1.25}$$

Thus, light emitted today will have $z = 0$, increasing the farther in the past it was emitted.

One quantity related to distance that astronomers can observe is the flux F, or power per unit area, of light being received from a source. This can be related to the total power being emitted by the source, or the luminosity L. This is useful because astronomers can use standard candles, or objects of known brightness, to predict luminosity. We then simply need to relate the luminosity to the flux. We can first imagine a static Euclidean universe, in which the radiation is emitted isotropically from a source. If we consider all the light which was emitted at some time t_1, it would have traveled a distance χ in all directions uniformly, being evenly spread over a sphere of radius $4\pi\chi^2$. Therefore, the observed flux will be:

$$F = \frac{L}{4\pi\chi^2}. \tag{1.26}$$

However, there are several modifications we must make in our Universe. First,

if the universe is not flat and the curvature $k \neq 0$, then we must generalize $\chi \to S_k(\chi)$ by Eq. 1.1. Second, the longer wavelength of the light implies the photons will arrive at a rate suppressed by $1/a(t_1)$, and hence reducing the observed flux by this factor. And finally, the longer wavelength of the light also reduces the energy of each photon suppressing the observed flux by another factor of $1/a(t_1)$. Correcting Eq. 1.26 for these factors, and applying Eq. 1.25, we have:

$$F = \frac{L}{4\pi S_k^2(\chi)(1+z)^2}. \tag{1.27}$$

Therefore, we see that the squared distance in flat space has effectively been replaced by $S_k^2(\chi)(1+z)^2$, hence use this to define the luminosity distance, d_L:

$$d_L(z) \equiv S_k(\chi)(1+z). \tag{1.28}$$

Another set of useful objects in observation are standard rulers, or objects of known size D. Such objects can be related to their distance from the observer by trigonometry. Assuming the object subtends a small angle $\delta\theta$ in the sky, we can make the small angle approximation. In a static Euclidean space, the relation would then be:

$$\delta\theta = \frac{D}{\chi}. \tag{1.29}$$

However, as before we must account for other geometries by generalizing $\chi \to S_k(\chi)$. We must also account for the fact that the comoving size of the object is actually $D/a(t_1)$, where t_1 is the time that the light was emitted from the object. Again, using Eq. 1.25 and correcting Eq. 1.29 for these effects, we obtain:

$$\delta\theta = \frac{D(1+z)}{S_k(\chi)}. \tag{1.30}$$

Therefore, by comparison with Eq. 1.29 we see the distance is now replaced by $S_k/(1+z)$, and thus we call this the angular diameter distance, d_A:

$$d_A(z) \equiv \frac{S_k(\chi)}{1+z}. \tag{1.31}$$

1.5 Eulerian Perturbation Theory

The dynamics in Sec. 1.1 only apply to a Universe which is homogeneous and isotropic. While they provide insight to many of the features of our Universe, we must figure out a way to grapple with the structure in our Universe, which

provides a wealth of data that can be used to constrain models. In order to study the formation of structure, we introduce cosmological perturbation theory which studies small deviations in the Universe from a homogeneous and isotropic background.

In the Eulerian formulation of perturbation theory, these deviations are considered at the level of the metric and energy-momentum tensors, and the fields that parameterize them. Eulerian perturbation theory can then be used to determine the dynamics of these fields as functions of spacetime coordinates, using the Einstein equation. Carrying the inhomogeneities as $\boldsymbol{x}$-dependence in the perturbations, the perturbed tensors will take the following form at first order:

$$g_{\mu\nu}(\eta, \mathbf{x}) = \bar{g}_{\mu\nu}(\eta) + \delta g_{\mu\nu}(\eta, \boldsymbol{x}) \,, \tag{1.32}$$
$$T_{\mu\nu}(\eta, \mathbf{x}) = \bar{T}_{\mu\nu}(\eta) + \delta T_{\mu\nu}(\eta, \boldsymbol{x}) \,, \tag{1.33}$$

where the bar explicitly denotes unperturbed quantities.

1.5.1 Scalar, Vector, Tensor Decomposition

We take the flat FLRW metric as the background metric, but written in the following form:

$$ds^2 = a^2(\eta)[-d\eta^2 + \gamma_{ij} dx^i dx^j] \,, \tag{1.34}$$

where γ_{ij} contains the spatial metric, having a constant curvature which I will use $K \equiv k/R_0^2$ to quantify[1]. We may then perform a decomposition of $\delta g_{\mu\nu}$ and write the perturbed metric in the form [8]:

$$g^{00} = -a^{-2}(1 - 2A) \,, \tag{1.35}$$
$$g^{0i} = -a^{-2} B^i \,, \tag{1.36}$$
$$g^{ij} = -a^{-2}(\gamma^{ij} - 2H_L \gamma^{ij} - 2H_T^{ij}) \,, \tag{1.37}$$

where A is a scalar perturbation to the potential, and B^i is a vector shift perturbation. We decomposed the spatial metric perturbation into a scalar H_L which serves as a perturbation to the curvature, and a traceless H_T^{ij} term. We also further decompose B^i by using the fact that any vector can be decomposed as $B^i = \nabla^i B + \hat{B}^i$ where B is a scalar, and the hat denotes a divergenceless quantity. Therefore, the 3 scalars, the divergenceless 3-vector, and the traceless, symmetric 3x3 rank-2 tensor comprise the $3 + 2 + 5 = 10$ degrees of freedom of the metric perturbation.

[1] This is to avoid confusion with wavenumbers k used later in this section.

The unperturbed stress energy tensor, we take to be that of a perfect fluid. Then we may write the perturbed stress energy tensor as:

$$T^0_0 = -\bar{\rho} - \delta\rho \,, \tag{1.38}$$
$$T^0_i = (\rho + P)(v_i - B_i) \,, \tag{1.39}$$
$$T^i_0 = -(\bar{\rho} + \bar{P})v_i \,, \tag{1.40}$$
$$T^i_j = (\bar{P} + \delta P)\delta^i_j + \bar{P}\Pi^i_j \,, \tag{1.41}$$

where $\delta\rho$ is a density perturbation, δP is a perturbation to the pressure, v_i is the peculiar bulk velocity, and Π_{ij} is a traceless tensor called the anisotropic stress perturbation. We sometimes discuss the density contrast $\delta \equiv \frac{\rho(\eta,\boldsymbol{x})-\bar{\rho}}{\bar{\rho}}$ which measures the fractional difference in the density from the homogeneous solution. Hence, we the stress perturbations may also be specified with $1 + 1 + 3 + 5 = 10$ parameters. With 10 Einstein equations, and 20 parameters, it appears we have $20-10 = 10$ degrees of freedom at this stage. We will later see that 4 more degrees of freedom can be removed by a change of coordinates[2].

The Einstein equations give rise to a coupled set of partial differential equations and can prove difficult to solve, therefore it is typical to make use of normal modes. We have scalar, divergenceless vector, and transverse traceless tensor eigenmodes, which are eigenfunctions of the Laplacian:

$$\nabla^2 Q^{(0)} = -k^2 Q^{(0)} \tag{1.42}$$
$$\nabla^2 Q^{(\pm1)}_i = -k^2 Q^{(\pm1)}_i \tag{1.43}$$
$$\nabla^2 Q^{(\pm2)}_{ij} = -k^2 Q^{(\pm2)}_{ij} \tag{1.44}$$

where ∇ is the covariant derivative, and it is understood that these eigenfunctions depend on the particular mode. In flat space these can be represented with:

$$Q^{(0)} = e^{i\mathbf{k}\cdot\mathbf{x}} \,, \tag{1.45}$$
$$Q^{(\pm1)}_i = \frac{-i}{\sqrt{2}}(\hat{\mathbf{e}}_1 \pm i\hat{\mathbf{e}}_2)_i e^{i\mathbf{k}\cdot\mathbf{x}} \,, \tag{1.46}$$
$$Q^{(\pm2)}_{ij} = -\sqrt{\frac{3}{8}}(\hat{\mathbf{e}}_1 \pm i\hat{\mathbf{e}}_2)_i(\hat{\mathbf{e}}_1 \pm i\hat{\mathbf{e}}_2)_j e^{i\mathbf{k}\cdot\mathbf{x}} \,, \tag{1.47}$$

where $\hat{\boldsymbol{e}}_1$ and $\hat{\boldsymbol{e}}_2$ are transverse to $\mathbf{k}$, however, the eigenfunctions will be different in curved space. The divergenceless vector modes capture the vorticity, and the transverse traceless tensor modes represent gravitational waves. We

[2]For the remainder of this section I suppress the bar over background quantities.

also have curl-free vector modes and longitudonal tensor modes:

$$Q_i^{(0)} = -k^{-1}\nabla_i Q^{(0)} \,, \tag{1.48}$$

$$Q_{ij}^{(0)} = (k^{-2}\nabla_i\nabla_j + \frac{1}{3}\gamma_{ij})Q^{(0)} \,, \tag{1.49}$$

$$Q_{ij}^{(\pm 1)} = -\frac{1}{2k}[\nabla_i Q_j^{(\pm 1)} + \nabla_j Q_i^{(\pm 1)}] \,, \tag{1.50}$$

which are built from the other scalar and vector eigenmodes.

Hence, any scalar, vector, or tensor can be expanded over all eigenmodes, with each eigenmode expanded over its various forms (divergenceless and curl-free for vectors, and transverse traceless and longitudonal for tensors). More concretely, for a given eigenmode the perturbations can be written for scalars as:

$$A = \hat{A}\, Q^{(0)} \,, \tag{1.51}$$

$$H_L = \hat{H}_L\, Q^{(0)} \,, \tag{1.52}$$

$$\delta\rho = \hat{\delta\rho}\, Q^{(0)} \,, \tag{1.53}$$

$$\delta P = \hat{\delta P}\, Q^{(0)} \,, \tag{1.54}$$

for vectors as:

$$B_i = \sum_{m=-1}^{1} \hat{B}^{(m)}\, Q_i^{(m)} \,, \tag{1.55}$$

$$v_i = \sum_{m=-1}^{1} \hat{v}^{(m)}\, Q_i^{(m)} \,, \tag{1.56}$$

and for tensor perturbations:

$$H_{Tij} = \sum_{m=-2}^{2} \hat{H}_T^{(m)}\, Q_{ij}^{(m)} \,, \tag{1.57}$$

$$\Pi_{ij} = \sum_{m=-2}^{2} \hat{\Pi}^{(m)}\, Q_{ij}^{(m)} \,. \tag{1.58}$$

We will now suppress the superscript (0) for scalars, the hat, and the bar for unperturbed quantities.

There are now 2 conservation, and 4 Einstein equations on the scalar per-

turbations, which hold for each mode:

$$\Big[\frac{d}{d\eta}+3\mathcal{H}\Big]\delta\rho+3\mathcal{H}\delta P=-(\rho+P)(kv+3\dot{H}_L)\,, \tag{1.59}$$

$$\Big[\frac{d}{d\eta}+4\mathcal{H}\Big][(\rho+P)\frac{(v-B)}{k}]=\delta P-\frac{2}{3}(1-3\frac{K}{k^2})P\Pi+(\rho+P)A\,, \tag{1.60}$$

$$(k^2-3K)[H_L+\frac{1}{3}H_T+\frac{\mathcal{H}}{k^2}(kB-\dot{H}_T)]=4\pi Ga^2\Big[\delta\rho+3\mathcal{H}(\rho+P)\frac{(v-B)}{k}\Big]\,, \tag{1.61}$$

$$k^2(A+H_L+\frac{1}{3}H_T)+\Big(\frac{d}{d\eta}+2\mathcal{H}\Big)(kB-\dot{H}_T)=-8\pi Ga^2P\Pi\,, \tag{1.62}$$

$$\mathcal{H}A-\dot{H}_L-\frac{1}{3}\dot{H}_T-\frac{K}{k^2}(kB-\dot{H}_T)=4\pi Ga^2(\rho+P)\frac{(v-B)}{k}\,, \tag{1.63}$$

$$\Big[2\dot{\mathcal{H}}+\mathcal{H}\frac{d}{d\eta}-\frac{k^2}{3}\Big]A-\Big[\frac{d}{d\eta}+\mathcal{H}\Big](\dot{H}_L+\frac{1}{3}kB)=4\pi Ga^2(\delta P+\frac{1}{3}\delta\rho)\,, \tag{1.64}$$

where dots are derivatives with respect to conformal time[3]. Note that only 4 of these equations are functionally independent. We also have 1 conservation and 2 Einstein equations on the vector perturbations:

$$\Big[\frac{d}{d\eta}+4\mathcal{H}\Big]\Big[(\rho+P)\frac{(v^{(\pm1)}-B^{(\pm1)})}{k}\Big]=-\frac{1}{2}(1-\frac{2K}{k^2})P\Pi^{(\pm1)}\,, \tag{1.65}$$

$$\Big(1-\frac{2K}{k^2}\Big)(kB^{(\pm1)}-\dot{H}_T^{(\pm1)})=16\pi Ga^2(\rho+P)\frac{(v^{(\pm1)}-B^{(\pm1)})}{k}\,, \tag{1.66}$$

$$\Big[\frac{d}{d\eta}+2\mathcal{H}\Big](kB^{(\pm1)}-\dot{H}_T^{(\pm1)})=-8\pi Ga^2P\Pi^{(\pm1)}\,, \tag{1.67}$$

where only 2 of these equations are independent. And finally, a single Einstein equation for the tensor perturbations:

$$\Big[\frac{d^2}{d\eta^2}+2\mathcal{H}\frac{d}{d\eta}+(k^2+2K)\Big]H_T^{(\pm2)}=8\pi Ga^2P\Pi^{(\pm2)}\,. \tag{1.68}$$

1.5.2 Gauges

In general, perturbations will take different forms depending on the choice of time-slicing and spatial-threading, which we call the gauge. It is possible to formulate perturbation theory using gauge invariant quantities, however we

[3]I will use this notation for this section.

can also fix the gauge to make certain perturbations vanish, or appear in a desired form. We can change gauges via a change of coordinates of the form:

$$\tau = \tilde{\tau} + TQ^{(0)} \,, \tag{1.69}$$

$$x_i = \tilde{x}_i + LQ_i^{(0)} + L^{(-1)}Q_i^{(-1)} + L^{(+1)}Q_i^{(+1)} \,, \tag{1.70}$$

where the parameters T, L, $L^{(-1)}$, and $L^{(+1)}$ are small. These 4 degrees of freedom can be used to eliminate 4 degrees of freedom from the perturbations. Here I will only focus on scalar gauges which only require fixing L and T.

Using the invariance of the metric line element we can solve for the transformation of the metric perturbations yielding:

$$A = \tilde{A} - \dot{T} - \mathcal{H}T \,, \tag{1.71}$$

$$B = \tilde{B} + \dot{L} + kT \,, \tag{1.72}$$

$$H_L = \tilde{H}_L - \frac{k}{3}L - \mathcal{H}T \,, \tag{1.73}$$

$$H_T = \tilde{H}_T + kL \,. \tag{1.74}$$

Similarly we get for the matter perturbations, for each species:

$$\delta\rho_i = \tilde{\delta\rho}_i - \dot{\rho}_i T \,, \tag{1.75}$$

$$\delta P_i = \tilde{\delta P}_i - \dot{P}_i T \,, \tag{1.76}$$

$$v_i = \tilde{v}_i + \dot{L} \,. \tag{1.77}$$

Comoving Gauge

Noticing that the combination $v - B$ appears throughout the Einstein and conservation equations, suggests that the choice $v = B$ would simplify the equations greatly. We also impose $H_T = 0$. Using our transformation rules this implies:

$$\tilde{H}_T + kL = 0 \,, \tag{1.78}$$

$$\tilde{B} + \dot{L} + kT = \tilde{v} + \dot{L} \,, \tag{1.79}$$

which fixes $L = -\tilde{H}_T/k$ and $T = (\tilde{v} - \tilde{B})/k$. We then rename the remaining variables $\xi \equiv A$ and $\zeta \equiv H_L$. Then Eq. 1.63 simplifies to:

$$\dot{\zeta} - \mathcal{H}\xi = 0 \,, \tag{1.80}$$

and Eq. 1.60 gives:

$$\delta P - \frac{2}{3}(1 - 3\frac{K}{k^2})P\Pi + (\rho + P)\xi = 0\,. \tag{1.81}$$

Together these combine to give:

$$\dot{\zeta} = \mathcal{H}\left[\frac{-1}{\rho + P}\delta P + \frac{2(1 - \frac{3K}{k^2})}{3(\rho + P)}P\Pi\right]. \tag{1.82}$$

Hence, we see that changes to the comoving curvature ζ are produced only by pressure perturbations and anisotropic stresses.

Newtonian Gauge

Newtonian gauge is defined by demanding $B = H_T = 0$, and then one typically renames $\Psi \equiv A$ and $\Phi \equiv H_L$. Hence we must solve:

$$\tilde{H}_T + kL = 0\,, \tag{1.83}$$

$$\tilde{B} + \dot{L} + kT = 0\,, \tag{1.84}$$

which is satisfied with $L = -\tilde{H}_T/k$ and $T = \dot{\tilde{H}}_T/k^2 - \tilde{B}/k$. This reduces the Einstein equations (Eq. 1.61 and Eq. 1.62) to:

$$(k^2 - 3K)\Phi = 4\pi G a^2[\delta\rho + 3\mathcal{H}(\rho + P)\frac{v}{k}]\,, \tag{1.85}$$

$$k^2(\Phi + \Psi) = -8\pi G a^2 P\Pi\,, \tag{1.86}$$

which generalize the Poisson equation of Newtonian gravity, hence the name of the gauge.

Synchronous Gauge

In synchronous gauge we impose that any time components of the metric perturbation vanish so that $A = B = 0$, and then rename $\eta_T \equiv -\frac{1}{3}H_T - H_L$ and $h_L \equiv 6H_L$. Then we have the conditions:

$$\tilde{A} - \dot{T} - \mathcal{H}T = 0\,, \tag{1.87}$$

$$\tilde{B} + \dot{L} + kT = 0\,, \tag{1.88}$$

which can be solved with:

$$T = \frac{1}{a}\int a\tilde{A}d\eta\,, \tag{1.89}$$

$$L = -\int(\tilde{B} + kT)d\eta\,. \tag{1.90}$$

Note that these definitions of L and T are not unique and will require specifying initial conditions to fix the integration constants. Typically, they are chosen so that the initial CDM velocity is 0. This gauge provides numerically stable equations which make it a popular choice for numerical solvers.

N-Body Gauge

We now discuss the N-body gauge originally introduced in [9], a useful gauge for N-body simulations, which are discussed more in Sec. 2.2. Similar to the comoving gauge, we set $B = v$, which fixes $T = (\tilde{v} - \tilde{B})/k$, and therefore by Eq. 1.75 fixes the density contrast δ. This reduces Eq. 1.61 in flat space to:

$$k^2[H_L + \frac{1}{3}H_T + \frac{\mathcal{H}}{k^2}(kB - \dot{H}_T)] = 4\pi G a^2\delta\rho\,. \tag{1.91}$$

However we may identify the gauge-invariant quantity known as one of the Bardeen potentials [10]:

$$\Phi \equiv H_L + \frac{1}{3}H_T + \frac{\mathcal{H}}{k^2}(kB - \dot{H}_T)\,, \tag{1.92}$$

so that we have:

$$k^2\Phi = 4\pi G a^2\delta\rho\,, \tag{1.93}$$

which resembles the Newtonian Poisson equation. In order to fix the spatial gauge L, we consider the fact that the trace of the spatial metric scales the volume element by a factor of $(1 + 3H_L)$ which causes a position dependent deformation of space. This is problematic for N-body simulations which measure the matter density from the simulations by counting particles in uniform volume elements. Hence, the spatial gauge is defined by demanding $H_L = 0$, which is satisfied by $L = 3[k\tilde{H}_L - \mathcal{H}(\tilde{v} - \tilde{B})]/k^2$, fixing the scalar portion of the gauge.

I will now focus exclusively on matter as this is the species evolved by N-body simulations. Using the conservation equation (Eq. 1.59) and the background continuity equation (Eq. 1.10) which hold for individual species, we get:

$$\dot{\delta}_m + kv_m = 0\,, \tag{1.94}$$

which is identical to the Newtonian continuity equation. We also get combining Eq. 1.60 and Eq. 1.62:

$$\dot{v}_m + \mathcal{H} v_m = -k(\Phi + \gamma) \,, \tag{1.95}$$

where we see that γ is a correction to the potential defined by:

$$k^2 \gamma \equiv 8\pi G a^2 P \Pi - \mathcal{H} H_T - \ddot{H}_T \,. \tag{1.96}$$

This agrees with the form of the Newtonian momentum conservation law when γ vanishes, which indeed is the case in matter-dominated or Λ-dominated universes [9].

Combining Eqs. 1.93-1.95 yields the following relationship:

$$\ddot{\delta}_m + \mathcal{H}\dot{\delta}_m - 4\pi G a^2 \delta\rho_m = 4\pi G a^2 \delta\rho_{\rm GR} \,, \tag{1.97}$$

where

$$\delta\rho_{\rm GR} \equiv \delta\rho_\gamma + \delta\rho_\nu + \delta\rho_{\rm DE} + \frac{k^2}{4\pi G a^2}\gamma \,. \tag{1.98}$$

We denote this $\delta\rho_{\rm GR}$, as the right hand side of Eq. 1.97 would vanish in a Newtonian Universe. Hence, Eqs. 1.93-1.95 and Eq. 1.97 show that the N-body gauge allows for a fully relativistic treatment of perturbations while being consistent with the form of equations evolved in Newtonian simulations.

1.6 Lagrangian Perturbation Theory

As opposed to Eulerian perturbation theory, which perturbed fluid-level quantities, Lagrangian perturbation theory (LPT) is a formulation of perturbation theory that considers the trajectories of *elements* of the fluid, or particles. One of the major uses of LPT is to set the initial conditions for N-body simulations.

We consider the dynamics of a matter particle in the Newtonian approximation in an expanding universe with geodesic equation [11, 12]:

$$\frac{d^2\boldsymbol{x}}{dt^2} + 2H\frac{d\boldsymbol{x}}{dt} = -\frac{1}{a^2}\nabla_{\boldsymbol{x}}\Phi \,, \tag{1.99}$$

where Φ satisfies the Poisson equation:

$$\nabla^2_{\boldsymbol{x}}\Phi = 4\pi G a^2 \bar{\rho}_m \delta_m \,. \tag{1.100}$$

We can write this using superconformal time τ defined by $d\tau = dt/a^2$, which

reduces the geodesic equation to:

$$\frac{d^2\boldsymbol{x}}{d\tau^2} = -a^2\nabla_{\boldsymbol{x}}\Phi \,. \tag{1.101}$$

The central quantity in LPT is the displacement field $\boldsymbol{\Psi}(\boldsymbol{q},\tau)$, which maps the initial position of a particle $\boldsymbol{q}$, to its final position $\boldsymbol{x}$:

$$\boldsymbol{x}(\boldsymbol{q},\tau) = \boldsymbol{q} + \boldsymbol{\Psi}(\boldsymbol{q},\tau) \,. \tag{1.102}$$

We then invoke a conservation of mass under this change of coordinates:

$$(1+\delta_m(\boldsymbol{x},\tau))d^3x = d^3q \,. \tag{1.103}$$

The Jacobian of this transformation is:

$$\mathcal{J} = \left|\frac{d^3x}{d^3q}\right|, \tag{1.104}$$

which combining with Eq. 1.103 gives:

$$\delta_m(\boldsymbol{x},\tau) = \frac{1}{\mathcal{J}} - 1 \,. \tag{1.105}$$

Taking the divergence of Eq. 1.101 and combining with Eq. 1.100 gives:

$$\nabla_{\boldsymbol{x}}\cdot\ddot{\boldsymbol{x}} = -4\pi G a^4\bar{\rho}_m\delta_m \,, \tag{1.106}$$

where dots represent derivatives with respect to τ. This simplifies to:

$$\mathcal{J}(\boldsymbol{q},\tau)\nabla_{\boldsymbol{x}}\cdot\ddot{\boldsymbol{x}} = 4\pi G a^4\bar{\rho}_m(\mathcal{J}(\boldsymbol{q},\tau)-1) \,. \tag{1.107}$$

Now we may solve this perturbatively, letting:

$$\boldsymbol{\Psi} = \epsilon\boldsymbol{\Psi}^{(1)} + \epsilon^2\boldsymbol{\Psi}^{(2)} + \epsilon^3\boldsymbol{\Psi}^{(3)} + \cdots \,. \tag{1.108}$$

Using Eq. 1.102, the determinant of the Jacobian is then:

$$\mathcal{J} = 1 + \epsilon K^{(1)} + \epsilon^2(K^{(2)} + L^{(2)}) + \epsilon^3(K^{(3)} + L^{(3)} + M^{(3)}) + \mathcal{O}(\epsilon^4) \,, \tag{1.109}$$

where $K^{(m)}$, $L^{(m)}$, and $M^{(m)}$ are the m-th order terms from:

$$K \equiv \sum_i \boldsymbol{\Psi}_{i,i} \,, \tag{1.110}$$

$$L \equiv \frac{1}{2} \sum_{i \neq j} (\boldsymbol{\Psi}_{i,i} \boldsymbol{\Psi}_{j,j} - \boldsymbol{\Psi}_{i,j} \boldsymbol{\Psi}_{j,i}) \,, \tag{1.111}$$

$$M \equiv \det(\Psi_{i,j}) \,. \tag{1.112}$$

The commas denote derivatives with respect to the components of $\boldsymbol{q}$. Therefore to first order we get $\mathcal{J}^{(1)} = \epsilon \nabla_{\boldsymbol{q}} \cdot \boldsymbol{\Psi}^{(1)}$.

In order to compute $\nabla_{\boldsymbol{x}} \cdot \ddot{\boldsymbol{x}}$ we notice $\nabla_{\boldsymbol{x}} \cdot \ddot{\boldsymbol{x}} = \nabla_{\boldsymbol{x}} \cdot \ddot{\boldsymbol{\Psi}}$. We can apply chain rule:

$$\nabla_{\boldsymbol{x}} \cdot \boldsymbol{\Psi} = \frac{d\boldsymbol{q}_i}{d\boldsymbol{x}_j} \frac{d}{d\boldsymbol{q}_i} \boldsymbol{\Psi}_j \,, \tag{1.113}$$

and then use Eq. 1.102 to see that at first order:

$$\frac{d\boldsymbol{q}_i}{d\boldsymbol{x}_j} = \delta_{ij} - \epsilon \boldsymbol{\Psi}^{(1)}_{i,j} \,. \tag{1.114}$$

Therefore, Eq. 1.107 becomes at first order:

$$\nabla_{\boldsymbol{q}} \cdot \ddot{\boldsymbol{\Psi}}^{(1)} = 4\pi G a^2 \bar{\rho}_m \nabla_{\boldsymbol{q}} \cdot \boldsymbol{\Psi}^{(1)} \,. \tag{1.115}$$

We factorize $\Psi^{(1)}(\boldsymbol{q}, \tau) = D_1(\tau) \boldsymbol{\Psi}^{(1)}(\boldsymbol{q}, \tau_{\rm ini})$, referring to D_1 as the linear growth factor. Using our result for $\mathcal{J}^{(1)}$ combined with Eq. 1.105, we get the initial condition:

$$\nabla_{\boldsymbol{q}} \cdot \boldsymbol{\Psi}^{(1)}(\boldsymbol{q}, \tau_{\rm ini}) = -\delta_{m,\rm ini} \,. \tag{1.116}$$

Plugging the factorized $\boldsymbol{\Psi}$ into Eq. 1.107 separates the equation into a time-dependent and a $\boldsymbol{q}$-dependent piece:

$$\nabla_{\boldsymbol{q}} \boldsymbol{\Psi}^{(1)}(\boldsymbol{q}, \tau_{\rm ini}) = \boldsymbol{\Psi}^{(1)}(\boldsymbol{q}, \tau_{\rm ini}) \,, \tag{1.117}$$

$$\ddot{D}_1(\tau) = 4\pi G a^2 \bar{\rho}_m D_1(\tau) \,. \tag{1.118}$$

Thus, Eq. 1.118 can be solved analytically, and Eq. 1.117 can be rewritten into the Laplace equation and solved with Fourier transforms, if we set $\boldsymbol{\Psi}^{(1)} = \nabla \phi^{(1)}$ for some scalar function ϕ. This is sensible provided the fact that vector perturbations decay with the Universe's expansion in the absence of anisotropic stress, meaning $\boldsymbol{\Psi}^{(1)}$ is irrotational. The initial conditions for the growing

solution during matter-domination are [12]:

$$D_1(\tau_{\rm ini}) = 1, \qquad \left(\frac{dD_1}{d\tau}\right)\bigg|_{\tau=\tau_{\rm ini}} = \left(\frac{1}{a}\frac{da}{d\tau}\right)\bigg|_{\tau=\tau_{\rm ini}}. \tag{1.119}$$

Going to second order yields that for the growing solution $D_2 = -\frac{3}{7}D_1^2$ [12], so that:

$$D_2(\tau_{\rm ini}) = -\frac{3}{7}, \qquad \left(\frac{dD_2}{d\tau}\right)\bigg|_{\tau=\tau_{\rm ini}} = -\frac{6}{7}\left(\frac{1}{a}\frac{da}{d\tau}\right)\bigg|_{\tau=\tau_{\rm ini}}. \tag{1.120}$$

1.7 Observables

In this section, I discuss some essential observable quantities that help link theoretical models and the measurable properties of the Universe. These include supernovae, the Cosmic Microwave Background (CMB), galaxy surveys, and many others not discussed here. Collectively, measuring these observables allows us to probe the expansion history of the Universe, the growth of its structure, and the nature of dark energy and dark matter.

1.7.1 Supernovae

Supernovae (SNe), the explosive deaths of massive stars, are a cornerstone in modern cosmology due to their ability to serve as standard candles. They can be classified by the processes that gave rise to the supernovae, and the spectra they emit:

- Type Ia: Result from thermonuclear explosion of white dwarf star in a binary system when it reaches the Chandrasekhar limit (~ 1.4 solar masses). Lack hydrogen lines in their spectra.
- Type Ib: Result from core-collapse of massive stars which have lost their outer hydrogen envelope. Lack hydrogen lines in their spectra.
- Type Ic: Result from core-collapse of massive stars which have lost both their outer hydrogen and helium envelopes. Lack hydrogen lines in their spectra.
- Type II: Result from core-collapse of massive stars which have retained their hydrogen envelope. They contain hydrogen lines in their spectra.

Unlike core-collapse supernovae, type Ia supernovae have a very consistent intrinsic peak luminosity, due to their formation via reaching the Chandrasekhar mass. Small variations in their peak brightness can be corrected using the Philips relation [13], making them standardizable candles. Cepheid variable stars, whose brightness varies periodically, are used to determine distances to nearby galaxies because their average brightness is related to this period by the Leavitt Law. These distances can then be used to calibrate the relationship between the intrinsic and observed luminosities of the supernovae. Once calibrated, these supernovae can be used to measure luminosity distances (Eq. 1.28) in Mpc via:

$$m - M_B = 5\log(d_L) + 25\,, \tag{1.121}$$

where m is the apparent magnitude and M_B is the intrinsic magnitude, which are related to luminosity.

The luminosity distance can also be predicted by ΛCDM. To compute Eq. 1.28 we need the comoving radius χ, which can be obtained by:

$$\chi(z) = \int_0^z \frac{1}{H(z')} dz'\,. \tag{1.122}$$

Then the Hubble parameter can be obtained by using Eqs. 1.11, 1.14, and 1.25, to rewrite the first Friedmann equation (Eq. 1.12) as:

$$H(z) = H_0\sqrt{\Omega_{m,0}(1+z)^3 + \Omega_{r,0}(1+z)^4 + \Omega_{k,0}(1+z)^2 + \Omega_{\Lambda,0}}\,. \tag{1.123}$$

At low redshifts, the radiation term is negligible. We may then use Eq. 1.28 to write the luminosity distance as:

$$d_L(z) = (1+z)S_k\left[\int_0^z \frac{dz'}{H_0\sqrt{\Omega_{m,0}(1+z')^3 + \Omega_{k,0}(1+z')^2 + \Omega_{\Lambda,0}}}\right]. \tag{1.124}$$

Inserting this into Eq. 1.121 allows values of the cosmological parameters to be inferred from supernovae, however there are degeneracies between the magnitudes and H_0. In 1998 two independent teams studying type Ia supernovae, the Supernova Cosmology Project [14] and the High-Z Supernova Search Team [15], found $\Omega_\Lambda \sim 0.7$, uncovering evidence of dark energy and implying that the Universe was experiencing accelerated expansion.

A more modern exploration of supernovae, the SH0ES program (Supernovae and H0 for the Equation of State of dark energy) [16] uses data from the Hubble Space Telescope and the Gaia mission to measure H_0. SH0ES uses

an approach called the local distance ladder, whereby a series of objects are used to calibrate distances. The first step uses geometric distances, independent of assumptions about brightness. These include using parallax, a method of measuring local distances by observing the shift in a star's position as Earth orbits the Sun, as well as observing more distant water masers orbiting black holes which provide precise angular scales and velocities. The next step uses Cepheid variable stars as standard candles to calibrate the Leavitt relation, which can then be extended to Cepheids in other galaxies. As mentioned, these Cepheids in other galaxies can be used to determine the distances to Type Ia supernovae, which in turn serve as standardizable candles to measure distances to very distant galaxies. The Hubble constant can then be measured by the distance-redshift relation:

$$cz \approx H_0 d \,, \tag{1.125}$$

which holds at low redshifts. Another notable recent supernovae dataset is Pantheon+ [17], which contains over 1,500 Type Ia supernovae across a wide redshift range.

1.7.2 Cosmic Microwave Background

The CMB is one of the most important probes in cosmology, providing a window into the early Universe. It was created approximately 380,000 years after the Big Bang, during a period known as recombination. At this time, the Universe had cooled enough to allow free electrons to combine with protons, forming hydrogen atoms and allowing photons to travel freely for the first time. This transition is referred to as decoupling, marking the moment when the Universe became transparent to radiation. The photons released at decoupling have since traveled nearly unimpeded, forming the signal we observe today.

The CMB was first discovered in 1965 by Arno Penzias and Robert Wilson, who detected a faint, uniform signal coming from across the sky. In 1992, NASA's Cosmic Background Explorer (COBE) satellite made the first precise measurements of the CMB, measuring its anisotropies and confirming its near-perfect blackbody spectrum [18]. Then in 2001, the Wilkinson Microwave Anisotropy Probe (WMAP) provided high-resolution temperature maps of the sky, allowing for the measurement of cosmological parameters [19]. The Planck satellite, which was launched in 2009, offered an even higher resolution view of the CMB, delivering the most detailed maps of its temperature and polarization anisotropies to date [1]. There have also been ground-based experiments like the Atacama Cosmology Telescope (ACT) [20] and the South Pole Telescope (SPT) [21] which have focused on measuring smaller angular scales and

probing effects like the gravitational lensing of the CMB.

The CMB anisotropies are analyzed through power spectra that quantify the statistical properties of various fields, such as temperature and polarization. Considering the case of temperature, we let $T(\hat{\boldsymbol{n}})$ be the measured temperature from the CMB in a direction $\hat{\boldsymbol{n}}$, and let $\bar{T}_0$ be the average CMB temperature today. We define the temperature fluctuation:

$$\Theta(\hat{\boldsymbol{n}}) \equiv \frac{T(\hat{\boldsymbol{n}}) - \bar{T}_0}{\bar{T}_0} \,. \tag{1.126}$$

We can take the correlation with another direction in the sky $\hat{\boldsymbol{n}}'$, giving the two-point correlation function:

$$C(\theta) = \langle \Theta(\hat{\boldsymbol{n}}) \Theta(\hat{\boldsymbol{n}}') \rangle \,, \tag{1.127}$$

where θ is defined by $\cos\theta \equiv \hat{\boldsymbol{n}} \cdot \hat{\boldsymbol{n}}'$.

Since we observe the CMB throughout the sky, its natural to expand the field in terms of spherical harmonics:

$$\Theta(\hat{\boldsymbol{n}}) = \sum_{\ell=2}^{\infty} \sum_{m=-\ell}^{\ell} a_{\ell m} Y_{\ell m}(\hat{\boldsymbol{n}}) \,, \tag{1.128}$$

where the $\ell = 0$ term vanishes due to the mean fluctuation $\langle \Theta \rangle = 0$, and the $\ell = 1$ term is considered a foreground effect, primarily arising from the peculiar motion of the observer relative to the CMB rest frame.

The multipole moments $a_{\ell m}$ have a two-point correlation:

$$\langle a_{\ell m} a^*_{\ell' m'} \rangle = C_\ell^{TT} \delta_{\ell \ell'} \delta_{m m'} \,, \tag{1.129}$$

where C_ℓ^{TT} is called the temperature angular power spectrum. We may then substitute this expansion into Eq. 1.127 and use Eq. 1.129 to yield:

$$C(\theta) = \sum_\ell C_\ell^{TT} \sum_m Y_{\ell m}(\hat{\boldsymbol{n}}) Y^*_{\ell m}(\hat{\boldsymbol{n}}') \,, \tag{1.130}$$

which can be written in terms of Legendre polynomials:

$$C(\theta) = \sum_\ell \frac{2\ell + 1}{4\pi} C_\ell^{TT} P_\ell(\cos\theta) \,. \tag{1.131}$$

Therefore, the C_ℓ^{TT} contain all the information about the temperature angular power spectrum. In addition to temperature, modern CMB experi-

ments measure the angular power spectrum of polarizations, broken into the E-mode (scalar-like) and B-mode (curl-like) polarizations, with their auto-correlations denoted by C_ℓ^{EE} and C_ℓ^{BB} respectively. They also measure the cross-correlations C_ℓ^{TE}, C_ℓ^{TB}, and C_ℓ^{EB}. Fig 1.1 shows the temperature power spectrum measured from the release by Planck in 2018 [1].

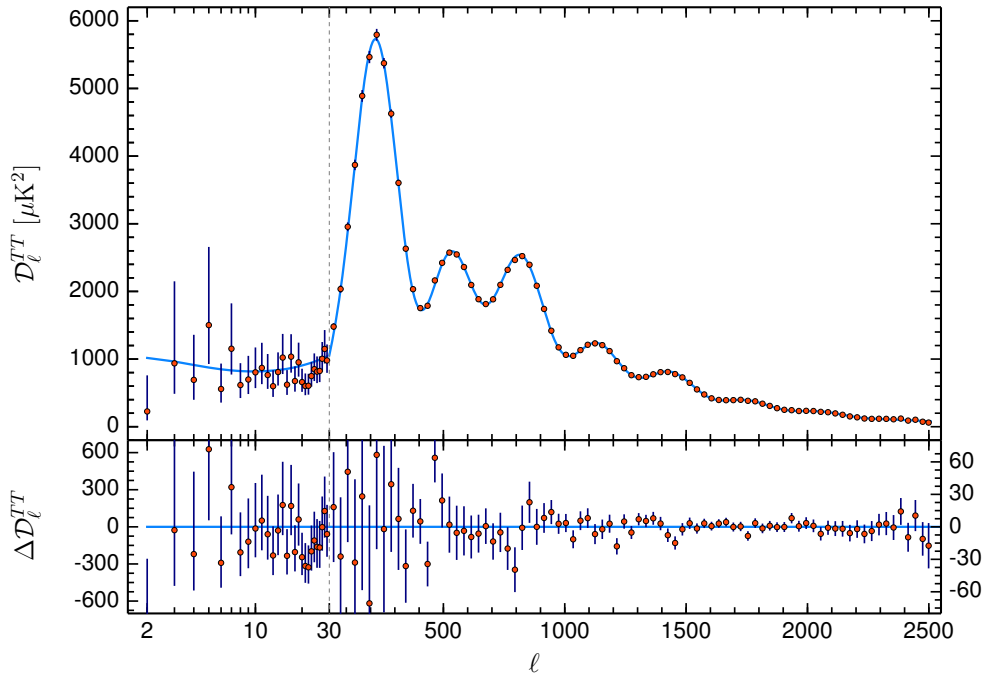


Figure 1.1: The temperature power spectrum from Planck 2018 [1]. Here $\mathcal{D}_\ell^{TT} \equiv \frac{\ell(\ell+1)}{2\pi} C_\ell^{TT}$ are plotted in the top panel, and their residuals $\Delta\mathcal{D}_\ell^{TT}$ relative to their best-fit.

In addition, modern CMB probes like Planck, ACT, and SPT measure what is called CMB lensing. While CMB photons travel, the large-scale structure of the Universe slightly interferes with their trajectory, an effect generally known as lensing. Therefore, there is a signature of large-scale structure encoded in the CMB power spectra. This lensing has the effect of smoothing the CMB power spectra on small angular scales, as well as converting E-mode polarization into B-mode polarization.

1.7.3 Large Scale Structure

Large-scale structure (LSS) refers to the distribution of matter on the largest observable scales in the Universe, comprised of galaxy clusters, filaments, and voids. These structures formed due to initial density perturbations in the early Universe, which grew over billions of years.

Matter Power Spectrum

In order to study the statistics of the matter density fluctuations we consider the two-point correlation function:

$$\xi(r) \equiv \langle \delta_m(\boldsymbol{x}) \delta_m(\boldsymbol{x}') \rangle = \frac{1}{V} \int d^3\boldsymbol{x} \delta_m(\boldsymbol{x}) \delta_m(\boldsymbol{x} - \boldsymbol{r}) \,, \tag{1.132}$$

where V is the real space volume and $\boldsymbol{r} \equiv \boldsymbol{x} - \boldsymbol{x}'$. The correlation function is only a function of the separation $\boldsymbol{r}$ because the statistical homogeneity of the Universe implies translational invariance, and furthers reduces to a function of only the magnitude $r = |\boldsymbol{r}|$ because statistical isotropy implies rotational invariance.

We may also consider the two-point correlation in Fourier space:

$$\langle \delta_m(\boldsymbol{k}) \delta_m^*(\boldsymbol{k}') \rangle = \left\langle \int \delta_m(\boldsymbol{x}) e^{-i\boldsymbol{k}\cdot\boldsymbol{x}} d^3\boldsymbol{x} \int \delta_m^*(\boldsymbol{x}') e^{i\boldsymbol{k}'\cdot\boldsymbol{x}'} d^3\boldsymbol{x}' \right\rangle \,, \tag{1.133}$$

$$= \int d^3\boldsymbol{x} d^3\boldsymbol{x}' e^{-i\boldsymbol{k}\cdot\boldsymbol{x}} e^{i\boldsymbol{k}'\cdot\boldsymbol{x}'} \langle \delta_m(\boldsymbol{x}) \delta_m(\boldsymbol{x}') \rangle \,, \tag{1.134}$$

$$= \int d^3\boldsymbol{r} d^3\boldsymbol{x}' e^{-i\boldsymbol{k}\cdot\boldsymbol{r}} e^{-i(\boldsymbol{k}-\boldsymbol{k}')\cdot\boldsymbol{x}'} \xi(r) \,, \tag{1.135}$$

where in the last equality we changed variables from $\boldsymbol{x}$ to $\boldsymbol{r}$. We then integrate over $\boldsymbol{x}'$:

$$\langle \delta_m(\boldsymbol{k}) \delta_m^*(\boldsymbol{k}') \rangle = (2\pi)^3 \delta_D(\boldsymbol{k} - \boldsymbol{k}') \int d^3r e^{-i\boldsymbol{k}\cdot\boldsymbol{r}} \xi(r) \,. \tag{1.136}$$

The factor of the Dirac delta function implies that Fourier modes evolve independently. Finally we identify the matter power spectrum $P(k)$ as the Fourier transform of $\xi(r)$ so that:

$$\langle \delta_m(\boldsymbol{k}) \delta_m^*(\boldsymbol{k}') \rangle = (2\pi)^3 \delta_D(\boldsymbol{k} - \boldsymbol{k}') P(k) \,. \tag{1.137}$$

Similar to $\xi(r)$, $P(k)$ does not depend on the direction of $\boldsymbol{k}$ due to statistical isotropy. The matter density evolves over time hence the power spectrum

does as well, therefore in general we write it as a function of wavenumber and redshift $P(k, z)$.

Galaxy Clustering

While the matter power spectrum is a fundamental quantity in the study of LSS, dark matter is not directly observable which complicates any attempt to measure it. One way to probe the matter field is to map the distribution of galaxies across the sky, which trace the underlying distribution of matter. Galaxy surveys, which catalog the positions, shapes, and redshifts of galaxies, have become indispensable in cosmology in the past few decades, with a level of precision that matches those of CMB measurements [22–35]. By measuring both the background expansion and the growth of structure, they can break degeneracies plaguing other cosmological probes [36–38]. I will now discuss some observables measured by galaxy surveys, and will assume a flat Universe for the remainder of this section.

One observable that galaxy surveys can measure is the correlation in galaxy positions. This is known as galaxy clustering, due to the tendency of galaxies to cluster together under the gravitational influence of the underlying matter distribution. We can define a galaxy overdensity in analogy with the matter case $\delta_g = (\rho_g - \bar{\rho}_g)/\bar{\rho}_g$, which we can then relate to the underlying matter field by defining the galaxy bias b:

$$\delta_g(\boldsymbol{x}, z) = b(z)\delta_m(\boldsymbol{x}, z) \, . \tag{1.138}$$

In general b can be a function of space as well but for simplicity I will treat it as only $b = b(z)$. Galaxy catalogs are typically broken down into tomographic redshift bins, which we will label with a superscript. In each bin there is a density of galaxies $n_g^i(z)$, which we write in normalized form as:

$$\bar{n}_g^i(z) = \frac{n^i(z)}{\int n^i(z')dz'} \, . \tag{1.139}$$

We also define the radial weight function:

$$q_{\delta_g}^i(\chi) \equiv b(z(\chi))\bar{n}_g^i(z)\frac{dz}{d\chi}, \tag{1.140}$$

which we have written as a function of the comoving distance χ.

Whereas Eq. 1.138 holds locally, the radial weight function can be used to relate δ_g to δ_m as a function of angular position on the sky. This is done by integrating along the line of sight, with $q_{\delta_g}^i(\chi)$ weighting δ_m by the galaxy bias

and galaxy population characteristics within the limits of the tomographic bin:

$$\delta_g^i(\hat{\boldsymbol{n}}) = \int_{\chi_{\rm min}}^{\chi_{\rm max}} d\chi q_{\delta_g}^i(\chi)\delta_m(\chi\hat{\boldsymbol{n}}) \,. \tag{1.141}$$

Here $\delta_g^i(\hat{\boldsymbol{n}})$ is now the angular galaxy density contrast for the i-th tomographic redshift bin.

We can now compute the angular two-point correlation of the galaxy density, considering two directions in the sky $\hat{\boldsymbol{n}}$ and $\hat{\boldsymbol{n}}'$ with separation θ, as in Eq. 1.127:

$$w^i(\theta) \equiv \langle \delta_g^i(\hat{\boldsymbol{n}})\delta_g^i(\hat{\boldsymbol{n}}')\rangle \,. \tag{1.142}$$

Following a similar decomposition into spherical harmonics as in the CMB temperature angular power spectrum, we get in analogy with Eq. 1.131 a simplified expression for the galaxy clustering observable:

$$w^i(\theta) = \sum_\ell \frac{2\ell+1}{4\pi} C^{ii}_{\delta_g\delta_g}(\ell) P_\ell(\cos\theta) \,, \tag{1.143}$$

where we only consider correlations within the same tomographic bin to localize the measurement. The coefficients $C^{ii}_{\delta_g\delta_g}(\ell)$ can be obtained using Eq. 1.141 and the Limber approximation [39]:

$$C^{ij}_{\delta_g\delta_g}(\ell) = \int d\chi \frac{q^i_{\delta_g}(\chi) q^j_{\delta_g}(\chi)}{\chi^2} P\left(k = \frac{\ell+\frac{1}{2}}{\chi}, z(\chi)\right) \,, \tag{1.144}$$

where the matter power spectrum $P(k,z)$ appears.

On small scales we can use the flat-sky approximation, where assuming $\hat{\boldsymbol{z}}$ points along the line of sight, we write the angular position in the sky in 2D Cartesian coordinates as $\boldsymbol{\alpha} = (\alpha_x, \alpha_y)$ in radians, with magnitude $\alpha = |\boldsymbol{\alpha}| = \sqrt{\alpha_x^2 + \alpha_y^2}$. In the present context, θ is then the magnitude of the separation vector between the angular positions of the two directions in the sky $\boldsymbol{\theta} = \boldsymbol{\theta}_{\hat{\boldsymbol{n}}} - \boldsymbol{\theta}_{\hat{\boldsymbol{n}}'}$. This allows us to treat $C^{ii}_{\delta_g\delta_g}(\ell)$ as the 2D Fourier transform of $w^i(\theta)$ with wavevector $\boldsymbol{\ell}$:

$$w^i(\theta) = \int \frac{d^2\ell}{(2\pi)^2} e^{i\boldsymbol{\ell}\cdot\boldsymbol{\theta}} C^{ii}_{\delta_g\delta_g}(\ell) \,. \tag{1.145}$$

We can perform this integral in 2D polar coordinates and integrate out the

angular coordinate giving:

$$w^i(\theta) = \int \frac{\ell d\ell}{2\pi} C^{ii}_{\delta_g \delta_g}(\ell) J_0(\ell\theta) \,, \tag{1.146}$$

where $J_n(x)$ is the n-th order Bessel function of the first kind.

Cosmic Shear

In addition to galaxy clustering, many galaxy surveys measure the distortion of the appearance of galaxy shapes due to gravitational lensing produced by LSS. This effect manifests as correlations between the shapes of galaxies, called cosmic shear, which are induced by gravitational potentials along the line of sight. Still working in the flat-sky approximation, gravitational lensing will distort the true angular position of the source galaxy $\boldsymbol{\theta}_S$, causing it to appear at an observed angular position $\boldsymbol{\theta}$. Assuming a small deflection, the comoving positions are then $\boldsymbol{x}_S = (\chi\boldsymbol{\theta}_S, \chi)$ and $\boldsymbol{x}_{\rm obs} = (\chi\boldsymbol{\theta}, \chi)$ respectively, where χ is the radial distance.

The deflection angle can then be written as the gradient with respect to $\boldsymbol{\theta}$ of a 2D potential, called the lensing potential ψ [40]:

$$\boldsymbol{\theta} - \boldsymbol{\theta}_S = \nabla_{\boldsymbol{\theta}} \psi(\boldsymbol{\theta}, \chi) \,, \tag{1.147}$$

where:

$$\psi(\boldsymbol{\theta}, \chi) \equiv 2 \int_0^\chi d\chi' \frac{\chi - \chi'}{\chi\chi'} \Phi(\chi'\boldsymbol{\theta}, \chi') \,, \tag{1.148}$$

and $\Phi(\boldsymbol{x})$ is the Newtonian potential. We define the following second derivatives of the lensing potential:

$$\kappa \equiv \frac{1}{2}(\partial_1\partial_1 + \partial_2\partial_2)\psi = \frac{1}{2}\nabla^2_{\boldsymbol{\theta}}\psi \,, \tag{1.149}$$

$$\gamma_1 \equiv \frac{1}{2}(\partial_1\partial_1 - \partial_2\partial_2)\psi \,, \tag{1.150}$$

$$\gamma_2 \equiv \partial_1\partial_2\psi \,, \tag{1.151}$$

where the partial derivatives are with respect to the components of $\boldsymbol{\theta}$. The convergence κ is an isotropic magnification of the galaxy's image due to lensing, and the shear $\gamma \equiv \gamma_1 + i\gamma_2$ is the anisotropic distortion of the galaxy's image, changing its observed ellipticity. Using Eq. 1.149, and applying the Poisson

equation, we may write the convergence as [40]:

$$\kappa(\boldsymbol{\theta},\chi) = \frac{3H_0^2\Omega_m}{2}\int_0^{\chi}\frac{d\chi'}{a(\chi')}\frac{\chi-\chi'}{\chi}\chi'\delta_m(\chi'\boldsymbol{\theta},\chi')\,. \tag{1.152}$$

We now consider a population of source galaxies, which are galaxies in the background whose images are being distorted by the large-scale structure, in a particular tomographic redshift bin. Let $n_\kappa^i(z)$ be their number density, which is defined in the the same way as the galaxy number density $n_g^i(z)$ but the subscript κ is used only for source galaxies. We may obtain the mean convergence from this population, by weighting Eq. 1.152 by the normalized $\bar{n}_\kappa^i(z)$:

$$\kappa^i(\boldsymbol{\theta}) = \int_{\chi_{\rm min}}^{\chi_{\rm max}} d\chi \bar{n}_\kappa^i(z(\chi))\kappa(\boldsymbol{\theta},\chi)\,, \tag{1.153}$$

where $\chi_{\rm min}$ and $\chi_{\rm max}$ are the limiting comoving distances of the *source* sample in the tomographic bin. This yields a relation similar to Eq. 1.141:

$$\kappa^i(\boldsymbol{\theta}) = \int_{\chi_{\rm min}}^{\chi_{\rm max}} d\chi q_\kappa^i(\chi)\delta_m(\chi\boldsymbol{\theta},\chi)\,, \tag{1.154}$$

where $q_\kappa^i(\chi)$ is the lensing efficiency, which quantifies the combined strength of the lensing at a distance χ:

$$q_\kappa^i(\chi) = \frac{3H_0^2\Omega_m}{2}\frac{\chi}{a(\chi)}\int_{\max(\chi,\chi_{\rm min})}^{\chi_{\rm max}} d\chi' \bar{n}_\kappa^i(z(\chi'))\frac{dz}{d\chi'}\frac{\chi'-\chi}{\chi}\,. \tag{1.155}$$

The shear $\gamma^i(\boldsymbol{\theta})$ can be obtained from $\kappa^i(\boldsymbol{\theta})$ easily in Fourier space:

$$\gamma^i(\boldsymbol{\ell}) = \frac{(\ell_1+i\ell_2)^2}{\ell^2}\kappa^i(\boldsymbol{\ell}) = e^{2i\phi_\ell}\kappa^i(\boldsymbol{\ell})\,, \tag{1.156}$$

where $\boldsymbol{\ell}$ is the 2D wavevector, and ϕ_ℓ is the polar angle of $\boldsymbol{\ell}$ in Fourier space. This relationship reveals that the power spectrum of the shear is equal to that of the convergence.

We are now ready to discuss the cosmic shear observables. In cosmic shear, the shear field $\gamma(\boldsymbol{\theta})$ is decomposed into a tangential component γ_t and a cross component $\gamma_\times$. Taking the direction vector $\boldsymbol{\theta}$, and letting ϕ_θ denote its polar angle, we can compute $\gamma_t(\boldsymbol{\theta})$ and $\gamma_\times(\boldsymbol{\theta})$ by:

$$\gamma_t = -\mathfrak{Re}(\gamma e^{-2i\phi_\theta}), \gamma_\times = -\mathfrak{Im}(\gamma e^{-2i\phi_\theta})\,. \tag{1.157}$$

Finally, the cosmic shear observables are:

$$\xi_{\pm}(\theta) \equiv \langle \gamma_t \gamma_t \rangle(\theta) \pm \langle \gamma_\times \gamma_\times \rangle(\theta) \,. \tag{1.158}$$

We can decompose $\kappa^i(\boldsymbol{\theta})$ into spherical harmonics and take the two-point correlation. Then, $C^{ij}_{\kappa\kappa}(\ell)$ is computed similarly to Eq. 1.144, using Eq. 1.154 and the Limber approximation, giving:

$$C^{ij}_{\kappa\kappa}(\ell) = \int d\chi \frac{q^i_\kappa(\chi) q^j_\kappa(\chi)}{\chi^2} P\left(k = \frac{\ell + \frac{1}{2}}{\chi}, z(\chi)\right) . \tag{1.159}$$

Then $\xi_{\pm}(\theta)$ can be computed in the flat sky as [41]:

$$\xi^{ij}_{+/-}(\theta) = \int \frac{d\ell \ell}{2\pi} J_{0/4}(\ell\theta) C^{ij}_{\kappa\kappa}(\ell) \,. \tag{1.160}$$

The full sky solution is [42]:

$$\xi^{ij}_{\pm}(\theta) = \sum_{\ell=0}^{\infty} \frac{2\ell+1}{4\pi} \frac{2(G^+_{\ell,2}(\cos\theta) \pm G^-_{\ell,2}(\cos\theta))}{\ell^2(\ell+1)^2} C^{ij}_{\kappa\kappa}(\ell) \,, \tag{1.161}$$

where $G^{\pm}_{\ell,2}$ are given by:

$$G^+_{\ell,2}(x) \pm G^-_{\ell,2}(x) = P^2_\ell(x) \left[\frac{4 - \ell \pm 2x(\ell-1)}{1-x^2} - \frac{\ell(\ell-1)}{2} \right] + P^2_{\ell-1}(x) \frac{(\ell+2)(x \mp 2)}{1-x^2} \,. \tag{1.162}$$

Galaxy-Galaxy Lensing

Lastly, galaxy surveys often measure the lensing effect produced by lens galaxies in the foreground on source galaxies at higher redshift. This is referred to as galaxy-galaxy lensing and it manifests as a cross-correlation between the lens galaxy positions and the tangential distortion to the observed source galaxy shapes. Studying this effect provides information about the mass profiles of the lens galaxies as well as their surrounding dark matter halos.

The galaxy-galaxy lensing observable is the angular cross-correlation between lens galaxy density and the source tangential shear field. Taking the direction of the lens galaxy to be $\hat{\boldsymbol{n}}$ in the i-th tomographic redshift bin, and the direction of the source galaxy $\hat{\boldsymbol{n}}'$ in the j-th redshift bin, with the directions

separated by an angle θ, the cross-correlation[4] is:

$$\gamma_t^{ij}(\theta) \equiv \langle \delta_g^i(\hat{\boldsymbol{n}})\gamma_t^j(\hat{\boldsymbol{n}}')\rangle \,. \tag{1.163}$$

Again, assuming the flat sky approximation we can perform a 2D Fourier decomposition as in Eq. 1.145:

$$\gamma_t^{ij}(\theta) = \int \frac{d^2\ell}{(2\pi)^2} e^{i\boldsymbol{\ell}\cdot\boldsymbol{\theta}} C^{ij}_{\delta_g\gamma_t}(\ell) \,. \tag{1.164}$$

From the definition of the tangential shear field $\gamma_t(\boldsymbol{\theta})$ in Eq. 1.157, and Eq. 1.156, we can compute the Fourier transform of $\gamma_t(\boldsymbol{\theta})$, which gives:

$$\gamma_t(\boldsymbol{\ell}) = -\kappa(\boldsymbol{\ell})\cos(2\phi_\ell) \,. \tag{1.165}$$

Therefore, $C^{ij}_{\delta_g\gamma_t}(\ell)$ can be computed by instead taking the cross-correlation with the convergence field κ^j:

$$C^{ij}_{\delta_g\gamma_t}(\ell) = -C^{ij}_{\delta_g\kappa}(\ell)\cos(2\phi_\ell) \,. \tag{1.166}$$

Substituting Eq. 1.166 into Eq. 1.164 and integrating over the polar angle ϕ_ℓ yields:

$$\gamma_t^{ij}(\theta) = -\int \frac{\ell d\ell}{2\pi} J_2(\ell\theta) C^{ij}_{\delta_g\kappa}(\ell) \,, \tag{1.167}$$

with $C^{ij}_{\delta_g\kappa}(\ell)$ given again using the Limber approximation, as well as Eq. 1.141 and Eq. 1.154:

$$C^{ij}_{\delta_g\kappa}(\ell) = \int d\chi \frac{q^i_{\delta_g}(\chi) q^j_\kappa(\chi)}{\chi^2} P\left(k = \frac{\ell+\frac{1}{2}}{\chi}, z(\chi)\right) . \tag{1.168}$$

In the full sky [42]:

$$\gamma_t^{ij}(\theta) = \sum_{\ell=0}^{\infty} \frac{2\ell+1}{4\pi} \frac{P^2_\ell(\cos\theta)}{\ell(\ell+1)} C^{ij}_{\delta_g\kappa}(\ell) \,. \tag{1.169}$$

Together, the three two-point correlation functions $w^i(\theta)$, $\xi^{ij}_\pm(\theta)$, and $\gamma_t^{ij}(\theta)$ are called 3x2-point data. The current generation of surveys, called Stage-III, that are contributing to gathering 3×2-point correlation data, include the

[4] I emphasize the difference between the correlation function and the tangential shear field (Eq. 1.157) which differ in notation by the arguments passed into the functions, or the tomographic superscripts.

Dark Energy Survey (DES), which has completed collecting data, and ongoing projects such as the Kilo-Degree Survey (KiDS) and the Hyper Suprime-Cam Subaru Strategic Program (HSC-SSP). The next generation of Stage-IV surveys has also begun, with the Dark Energy Spectroscopic Instrument (DESI) providing its first release in 2024 [43], and the Euclid mission having begun its operations in 2023. Upcoming Stage-IV projects include the Legacy Survey of Space and Time (LSST) and the Nancy Grace Roman Space Telescope.

1.8 Tensions in ΛCDM

1.8.1 The Hubble Tension

While the ΛCDM model has provided a good fit to a variety of data sets with only six free parameters, when held to precision tests there are signs of possible incompleteness. One of the starkest examples of this is the Hubble tension problem. Measurements of H_0 inferred from a ΛCDM fit to the CMB, such as Planck ($H_0 = 67.36 \pm 0.54$ km s^{-1}Mpc^{-1} [1]), are significantly lower than those from the local distance ladder, such as from SH0ES ($H_0 = 73.17 \pm 0.86$ km s^{-1}Mpc^{-1} [16]). This clears the 5σ threshold, suggesting that it is extremely unlikely this discrepancy is due to random statistical fluctuations. Fig. 1.2 compares a variety of H_0 constraints from recent years.

One potential explanation for the tension is the presence of unaccounted for experimental systematics that may bias the constraints. Some CMB systematics that could be contributing to the tension are obstructions in the foreground not being properly subtracted, or flawed instrument calibration. However, known CMB systematics are not expected to raise the inferred value of H_0 by more than ~ 1 km s^{-1}Mpc^{-1} within ΛCDM [2]. There is also the possibility of unaccounted for systematics in the distance ladder such as intervening dust or the varying metallicity of Cepheids which can affect their luminosities. However, several independent systematic errors would likely have to be present to resolve the tension, as it persists even with the removal of measurements of any particular object such as type Ia SNe or Cepheids [2].

There is also the possibility of new physics that may resolve the tension. Because the local distance ladder measurements are model-independent, we must consider how H_0 is constrained by the CMB. The first peak of the CMB power spectra corresponds to the angular scale of the sound horizon, θ_s, which represents the ratio of the comoving sound horizon at last scattering $r_s(z_*)$, to the comoving angular diameter distance to surface of last scattering, $D_A(z_*)$.

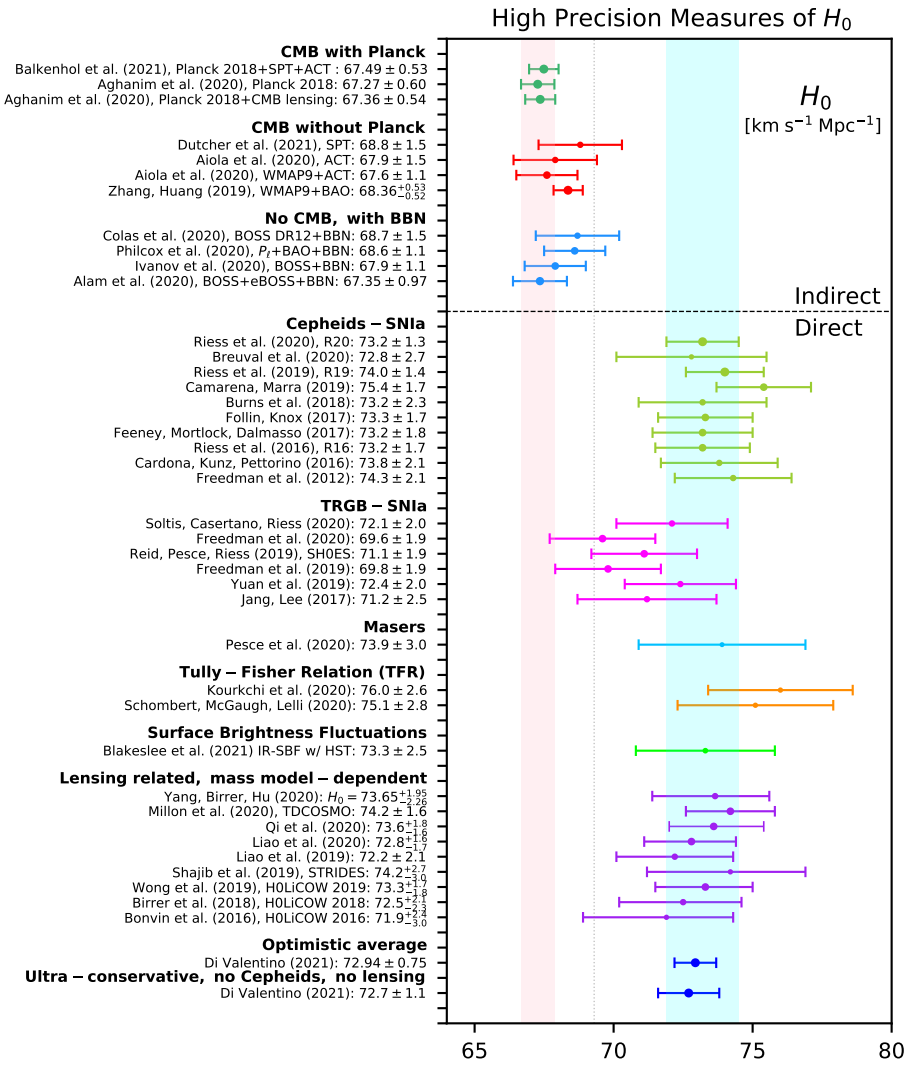


Figure 1.2: Compilation of various H_0 constraints published between 2012-2021, taken from [2]. The cyan band is the 2020 SH0ES constraint from [3], and the pink band is the 2018 Planck constraint [1].

This can be computed with integrals over the Hubble parameter:

$$\theta_s = \frac{r_s(z_*)}{D_A(z_*)} = \frac{\int_{z_*}^{\infty} dz' c_s(z')/H(z')}{\int_0^{z_*} dz'/H(z')}\,, \tag{1.170}$$

where c_s is the sound speed of the photon-baryon fluid, and $z_* \approx 1100$ is the

redshift at decoupling.

In order to solve the Hubble tension, any new model would have to yield a higher value of H_0 when fit to CMB data, bringing the value into closer agreement with the local distance ladder. However, θ_s is the most well-constrained quantity in the CMB, having been measured to within 0.03% precision by Planck 2018 [1], hence any new model cannot significantly alter θ_s. From Eq. 1.170 we see that the sound horizon is most sensitive to physics right before decoupling, while $D_A(z_*)$ only depends on physics after decoupling. Therefore, if we are to accommodate a higher value of H_0, we can most efficiently compensate by increasing $H(z)$ right before last scattering, preserving θ_s. This also prevents interfering with other ΛCDM successes. By the first Friedmann equation (Eq. 1.12) we see that we can increase the Hubble parameter by introducing additional sources of energy density. In Sec. 3 I will discuss a model that achieves this.

1.8.2 The S_8 Tension

A key parameter in studying the growth of large-scale structure is the parameter σ_8, defined as the RMS of the matter overdensity on scales of $8h^{-1}$Mpc today. This can be computed with an integral over the matter power spectrum:

$$\sigma_8^2 = \int_0^\infty \frac{k^2 dk}{2\pi^2} P(k)|W(k)|^2 \,, \tag{1.171}$$

where $W(k)$ is the Fourier transform of the real space "top hat" function, which filters the density field δ_m onto a scale of $8h^{-1}$Mpc. However, because this parameter is degenerate with $\Omega_{m,0}$, the parameter S_8 was defined to reduce the degeneracy:

$$S_8 \equiv \sigma_8 \sqrt{\frac{\Omega_m}{0.3}} \,, \tag{1.172}$$

where from this point forward I switch to notation where $\Omega_i \equiv \Omega_{i,0}$.

This parameter, S_8, has garnered significant attention in recent years due to a persistent discrepancy between its values inferred within ΛCDM from low redshift LSS probes, and high redshift CMB probes. This discrepancy reaches roughly $\sim 3\sigma$ depending on the datasets, falling short of the typical 5σ significance threshold leading to ongoing debate about whether it constitutes a genuine tension or normal statistical variation. Nevertheless, it has sparked considerable interest as a potential sign of new physics or unaccounted for experimental systematics. In Fig. 1.3 I show a summary of S_8 constraints, taken from [4], where it is clear that LSS measurements tend to deliver lower S_8 constraints than those from the CMB.

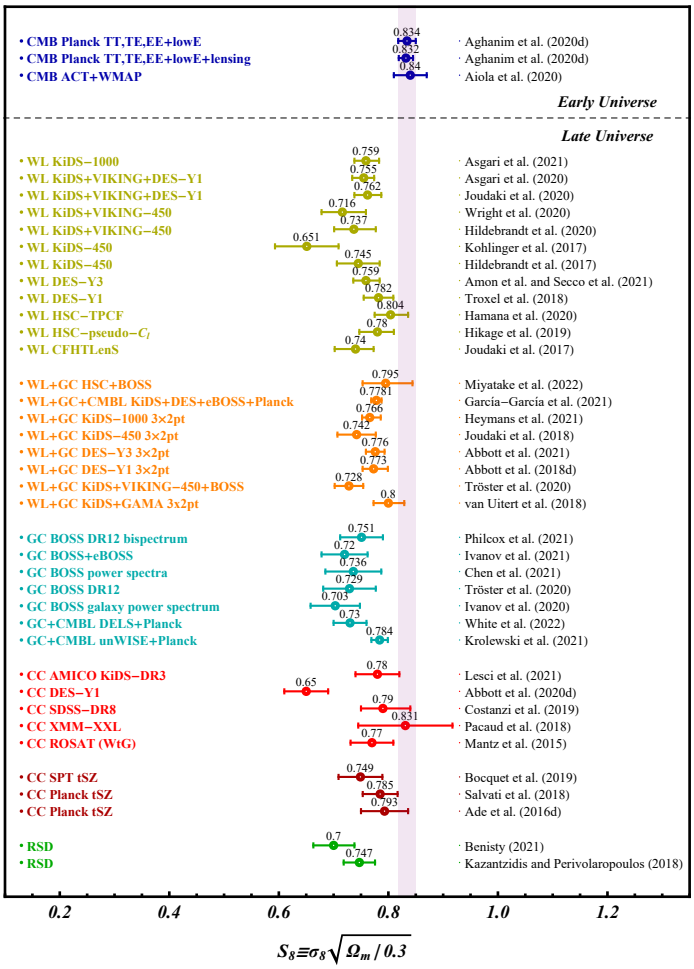


Figure 1.3: Compilation of various S_8 constraints from CMB and LSS probes, taken from [4].

There are a number of experimental systematics that could be affecting the determination of S_8 from galaxy surveys. These include systematics in cosmic shear, photometric redshift, intrinsic alignment, small-angle approximations, or in modeling baryonic feedback. Nevertheless, there are reasons to be skeptical that any of these explanations alone can account for the observed tension in S_8 [4]. Because the values of S_8 determined from the CMB are higher than those inferred from LSS data, models that hope to resolve the S_8 tension typically try to suppress the growth of structure at late times. One class of models frequently studied for this purpose are interacting dark energy models (IDE) which couple dark matter with dark energy, causing the dark energy to cut into the dark matter density at late times. In Sec. 3 we test

modifying late time dark energy behavior using a general smooth dark energy with equation of state $w(z)$.

Chapter 2

Computational Tools

In this section, I describe a few computational methods that are essential to the later work outlined in this thesis.

2.1 Bayesian Inference and MCMCs

Now that we have defined observable quantities that can be measured by experiments, and motivated the need to test many cosmological models, we must consider how to cross-reference experimental measurements with theoretical predictions and constrain model parameters. To formalize the desired goal, we invoke Bayesian statistics. The experimental data, stored in a vector $\boldsymbol{d}_{\rm exp}$, can be used to update a Bayesian "prior" distribution over the parameters $P(\boldsymbol{\theta})$, in order to obtain a "posterior" distribution given the new data $P(\boldsymbol{\theta}|\boldsymbol{d}_{\rm exp})$. By Bayes' Theorem, the posterior is related to the prior by:

$$P(\boldsymbol{\theta}|\boldsymbol{d}_{\rm exp}) = \frac{P(\boldsymbol{d}_{\rm exp}|\boldsymbol{\theta})P(\boldsymbol{\theta})}{P(\boldsymbol{d}_{\rm exp})} \,. \tag{2.1}$$

$P(\boldsymbol{d}_{\rm exp}|\boldsymbol{\theta})$ is called the likelihood function, often denoted $\mathcal{L}(\boldsymbol{\theta})$. Typically, flat priors are assumed in cosmology so that the likelihood is what determines the shape of the posterior. Operationally, the likelihood function is often provided by the experiment, requiring the user only to supply a prediction of a data vector based on the given parameters $\boldsymbol{d}_{\rm theo}(\boldsymbol{\theta})$ of their cosmological model of interest. $P(\boldsymbol{d}_{\rm exp})$, called the Bayesian evidence, effectively serves as a normalization constant as it does not vary as a function of $\boldsymbol{\theta}$. However, this normalization is notoriously difficult to compute as it typically requires integrating the likelihood in very high-dimensional parameter spaces, which is challenging as we will discuss.

In the case that the likelihood is Gaussian, the likelihood function takes

the form:

$$\mathcal{L}(\boldsymbol{\theta}) = \frac{1}{(2\pi)^{N/2}|C|^{1/2}} \exp\Big[-\frac{1}{2}(\boldsymbol{d}_{\rm theo}(\boldsymbol{\theta}) - \boldsymbol{d}_{\rm exp})^T C^{-1}(\boldsymbol{d}_{\rm theo}(\boldsymbol{\theta}) - \boldsymbol{d}_{\rm exp})\Big], \quad (2.2)$$

where N is the number of data points in each data vector, and C is the covariance matrix between the data points. Equivalently, we can identify the χ^2 statistic $\chi^2 \equiv (\boldsymbol{d}_{\rm theo}(\boldsymbol{\theta}) - \boldsymbol{d}_{\rm exp})^T C^{-1}(\boldsymbol{d}_{\rm theo}(\boldsymbol{\theta}) - \boldsymbol{d}_{\rm exp})$, so that $\boldsymbol{\mathcal{L}} \propto \exp[-\frac{1}{2}\chi^2]$. While many likelihoods are non-Gaussian, it still often provides a good approximation near the maximum.

The goal of finding the parameters that best fit the experimental data then becomes the problem of searching the parameter space for the region where the likelihood is maximized. This task becomes particularly difficult when the likelihood is multi-modal. In addition, measurements of observables generally depend not only on cosmological parameters but also on parameters related to the systematics of the experiment, known as nuisance parameters. Together, these parameters create a very high-dimensional space, rendering methods that sample the parameter space uniformly computationally intractable, such as grid-based approaches, or generic Monte Carlo methods that simply generate random samples. This is because under such methods, much time is spent exploring regions of the parameter space where the likelihood is negligible, and the number of points required to achieve a certain level of accuracy increases exponentially with the number of dimensions, a problem known as the curse of dimensionality.

This is the motivation for the use of Markov Chain Monte Carlo (MCMC) methods. MCMCs are Monte Carlo methods that allow one to effectively draw samples from a desired distribution, which we can apply in order to sample points directly from the posterior. This will ensure that minimal time is spent in low-likelihood regions of the parameter space, and allow us to directly measure the posterior. Underlying MCMC methods are Markov chains, which arise when one has a space of states which may each transition into any of the other states, with the probability of each transition depending only on the previous state and none visited prior. This naturally fits our Monte Carlo sampling approach as we may think of the different points in the parameter space $\boldsymbol{\theta}$ as states, which influence which point is next sampled. The Markov condition is then $p(\boldsymbol{\theta}_{i+1}|\boldsymbol{\theta}_i, ..., \boldsymbol{\theta}_1) = p(\boldsymbol{\theta}_{i+1}|\boldsymbol{\theta}_i)$.

For this continuous state space, we have a transition probability density between two states $T(\boldsymbol{\theta}'|\boldsymbol{\theta})$ that is normalized by $\int T(\boldsymbol{\theta}'|\boldsymbol{\theta})d\boldsymbol{\theta}' = 1$. A useful feature of Markov chains is that they often converge to a stationary distribution, such that after a certain number of steps in the chain the probability of visiting any given state follows the same distribution $\pi(\boldsymbol{\theta})$. In a stationary

state, an equilibrium is reached such that the flow of probability into a given state is equal to the flow out of it, known as the detailed-balance condition: $p(\boldsymbol{\theta}_{i+1}|\boldsymbol{\theta}_i) = p(\boldsymbol{\theta}_i|\boldsymbol{\theta}_{i+1})$. Assuming we are in a stationary state $\pi(\boldsymbol{\theta})$, we can break down this condition into:

$$T(\boldsymbol{\theta}_{i+1}|\boldsymbol{\theta}_i)\pi(\boldsymbol{\theta}_i) = T(\boldsymbol{\theta}_i|\boldsymbol{\theta}_{i+1})\pi(\boldsymbol{\theta}_{i+1}) \,. \tag{2.3}$$

We may then integrate over $\boldsymbol{\theta}_i$ on both sides giving:

$$\int T(\boldsymbol{\theta}_{i+1}|\boldsymbol{\theta}_i)\pi(\boldsymbol{\theta}_i)d\boldsymbol{\theta}_i = \pi(\boldsymbol{\theta}_{i+1}) \int T(\boldsymbol{\theta}_i|\boldsymbol{\theta}_{i+1})d\boldsymbol{\theta}_i \,. \tag{2.4}$$

Then we apply the normalization of T:

$$\int T(\boldsymbol{\theta}_{i+1}|\boldsymbol{\theta}_i)\pi(\boldsymbol{\theta}_i)d\boldsymbol{\theta}_i = \pi(\boldsymbol{\theta}_{i+1}) \,. \tag{2.5}$$

However, the left hand side is exactly the probability distribution for $\boldsymbol{\theta}_{i+1}$ assuming the previous sample was drawn from $\pi(\boldsymbol{\theta})$. Therefore, if a sample is drawn from a distribution $\pi(\boldsymbol{\theta})$ which satisfies the detailed-balance condition, any subsequent samples will also be drawn from $\pi(\boldsymbol{\theta})$.

Thus, in order for the Monte Carlo sampling to draw samples from the posterior, we need only to set up transition probabilities that, together with the posterior distribution, satisfy the detailed-balance and hence make the posterior a stationary state. The most commonly used algorithm that achieves this is the Metropolis-Hastings algorithm, which begins by decomposing the sampling into a proposal and an acceptance step:

$$T(\boldsymbol{\theta}_{i+1}|\boldsymbol{\theta}_i) = p_{\text{acc}}(\boldsymbol{\theta}_{i+1}|\boldsymbol{\theta}_i)P(\boldsymbol{\theta}_{i+1}|\boldsymbol{\theta}_i) \,. \tag{2.6}$$

The proposal distribution $P(\boldsymbol{\theta}_{i+1}|\boldsymbol{\theta}_i)$ is used to propose the next point sampled in the chain, however the proposed points are only accepted with a probability $p_{\text{acc}}(\boldsymbol{\theta}_{i+1}|\boldsymbol{\theta}_i)$. The proposal must be an easy to sample function in order to be computationally useful and not provide roadblocks itself.

The acceptance probability in the Metropolis-Hastings algorithm is given by:

$$p_{\text{acc}}(\boldsymbol{\theta}_{i+1}|\boldsymbol{\theta}_i) = \min\Big[\frac{\pi(\boldsymbol{\theta}_{i+1})P(\boldsymbol{\theta}_i|\boldsymbol{\theta}_{i+1})}{\pi(\boldsymbol{\theta}_i)P(\boldsymbol{\theta}_{i+1}|\boldsymbol{\theta}_i)}, 1\Big] \,, \tag{2.7}$$

where $\pi(\boldsymbol{\theta})$ is the distribution which we seek to make the steady state, i.e. the posterior. As this only requires knowing the *ratio* between two values of the posterior, it does not require knowing the normalization of the posterior. Often the proposal is chosen to be symmetric such that $P(\boldsymbol{\theta}_{i+1}|\boldsymbol{\theta}_i) = P(\boldsymbol{\theta}_i|\boldsymbol{\theta}_{i+1})$, in

which case it is known as simply the Metropolis algorithm. The acceptance probability then is:

$$p_{\text{acc}}(\boldsymbol{\theta}_{i+1}|\boldsymbol{\theta}_i) = \min\left[\frac{\pi(\boldsymbol{\theta}_{i+1})}{\pi(\boldsymbol{\theta}_i)}, 1\right], \tag{2.8}$$

which reveals some key features. When the posterior (which is proportional to the likelihood when flat priors are used) gives the next proposed point a higher or equal probability than the previous, then it will be accepted with probability 1. Hence, the algorithm will give preference to high posterior regions and optimize the Monte Carlo sampling. However, when the posterior gives less probability to the next proposed point, it will be still be given a non-zero probability of being accepted, which prevents the sampling from getting trapped at local maxima.

It is straightforward to check that with this choice of transition probabilities the detailed-balance condition Eq. 2.3 is satisfied and hence the chain is guaranteed to sample from the posterior after a certain number of steps. As the number of steps needed before the chain begins to follow the steady-state behavior is unknown, samples drawn before a certain step in the chain are usually discarded before measuring the posterior, known as the burn-in. There are a number of ways to establish convergence of the chain to the steady state, the most common being the Gelman-Rubin criteria [44] which involves running several independent chains with different initial states and comparing the within-chain variance to the between-chain variance.

2.2 N-body Simulations

The matter overdensity $\delta_m(k)$ was defined in Eq. 1.137 and equations to determine the matter density field to first order were shown in Sec. 1.5. The linear solution is valid as long as δ_m remains small so that perturbative techniques can be applied. Numerical Einstein-Boltzmann solvers exist such as CAMB[1] and CLASS[2] [45] which make solving for the overdensity to first order in practice quick and straightforward. However, at sufficiently small scales, especially at late times, gravitational collapse leads to regions of high concentrations of matter as well as empty voids. In this regime, the solution from linear perturbation theory loses accuracy, and hence the corresponding small scales are called "nonlinear". Without perturbative techniques, modeling the matter power spectrum can prove very challenging. Fig. 2.1 shows a compar-

[1] `github.com/cmbant/CAMB`

[2] `github.com/lesgourg/class_public`

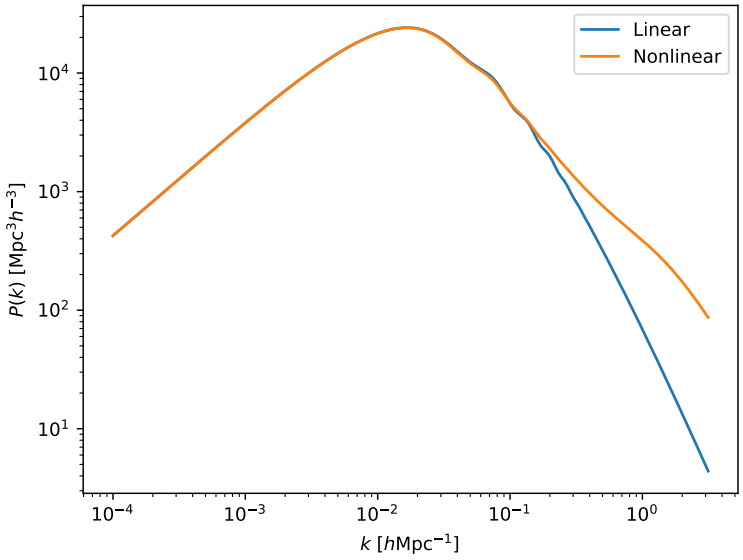


Figure 2.1: Comparison between the linear and nonlinear matter power spectrum at $z = 0$ for a ΛCDM cosmology. The linear solution underestimates power on small scales.

ison between the linear and nonlinear matter power spectrum at $z = 0$ for a reasonable ΛCDM cosmology, where it is clear that the linear solution is unable to adequately capture power on small scales.

The most accurate technique for modeling the nonlinear matter power spectrum is considered to be through the use of N-body simulations. The basic scheme of these simulations is to take a large number of matter particles $N_{\rm part}$ contained within a periodic box of side-length L at some initial redshift $z_{\rm initial}$, compute their respective gravitational forces, and evolve the particle positions over a number of time-steps. The matter density field and its statistics can then be measured by imposing a grid on the distribution of particles.

2.2.1 Algorithms and Techniques

The initial conditions of N-body simulations are typically generated using LPT, discussed in Sec. 1.6. Starting from an initial linear power spectrum $P_{\rm initial}(k) \equiv P_{\rm L}(k, z = z_{\rm initial})$, we can reconstruct the Fourier modes of the matter density field over the grid, ensuring its a Gaussian random field so that we can write $\delta_k = A_k e^{i\phi_k}$. We therefore draw the amplitudes from a Rayleigh distribution $A_k \sim \text{Rayleigh}(\sqrt{\text{P}_{\rm initial}(\text{k})}\,)$, and the phases are drawn from a

uniform distribution $\phi_k \sim \mathcal{U}(0, 2\pi)$. One must then impose the Hermitian condition $\delta_{-k} = \delta_k^*$ so that the real-space density field is real. Applying the methods of Sec. 1.6 we can use the density field to compute the displacement field $\boldsymbol{\Psi}(\boldsymbol{q}, t = t_{\text{initial}})$, and then displace some uniform distribution of particles by Eq. 1.102 giving the initial particles positions for the simulation. Finally, the initial particle velocities can be computed by $\boldsymbol{v} = \dot{\boldsymbol{x}} = \dot{\boldsymbol{\Psi}}$.

There are a number of different algorithms used to compute the gravitational force between particles, including but not limited to [46]:

- **Particle-Particle (PP)** - The gravitational force on ith particle is computed as:
$$\boldsymbol{F}_i = \sum_{j \neq i} \frac{Gm^2}{|\boldsymbol{r}_i - \boldsymbol{r}_j|^2 + \epsilon^2} \frac{(\boldsymbol{r}_i - \boldsymbol{r}_j)}{|\boldsymbol{r}_i - \boldsymbol{r}_j|}\,, \tag{2.9}$$
where ϵ is called the "softening" length and prevents the force from blowing up when particles are in close proximity. This algorithm carries a computational complexity of $\mathcal{O}(N_{\text{part}}^2)$ as the force between all pairs of particles must be considered at each time-step in order to move the particles. This method also requires a careful handling of the particles "outside" the box due to the periodic boundary conditions.

- **Particle-Mesh (PM)** - At each time-step the density field is measured using a mesh grid, then the Poisson equation in Fourier space allows the gravitational potential and its gradient to be easily computed, giving the force. This is summarized by the following equation:
$$\nabla\Phi = \mathcal{F}^{-1}\left[\frac{3}{2}\frac{\Omega_{m,0}\boldsymbol{k}}{ak^2}\mathcal{F}[\rho_m(\boldsymbol{x}) - 1]\right]\,, \tag{2.10}$$
where here $\mathcal{F}$ is the discrete Fourier transform. For a simulation with N_{mesh} cells in the mesh grid, the FFT algorithm reduces the computational complexity to $\mathcal{O}(N_{\text{mesh}} \log N_{\text{mesh}})$. Typically, $N_{\text{mesh}} \propto N_{\text{part}}$, so this is an improved scaling relative to PP simulations. However, this improvement comes at the cost of resolution at small scales due to the finite size of the cells.

- **Particle-Particle-Particle-Mesh ($\mathbf{P^3M}$)** - Separates the force into long-range and short-range components, and uses PM to evolve the former and PP to evolve the latter. By applying the PP algorithm only to the short-range forces it reduces the computational toll.

The minimum length scale in which the force between particles can be reliably calculated in a simulation is called the "force resolution" ℓ_{force}. In

PP simulations the softening length effectively sets a lower limit on the force resolution, particles closer than ϵ experience a significantly modified force. Meanwhile in PM simulations, the size of the mesh grids determines the force resolution. This poses a much more significant limitation as it is very computationally expensive to increase the number of mesh grids N_{mesh}.

A closely related quantity is the Nyquist frequency, which represents the highest frequency that can reliably be resolved in the simulation. For instance, for a simulation with cell grids of size Δx, the Nyquist frequency would be $k_{\text{Nyquist}} = \frac{\pi}{\Delta x}$. Another important measure of a simulation's resolution is the "mass resolution" M_{part}, which is the mass of each particle. By lowering M_{part} the simulation captures the behavior of less massive structures.

Another limitation affecting simulations is that of sample variance, as the simulation only provides one realization of the density field based on the initial conditions. Due to the finite size of the simulation box, the smallest modes in the box $k_{\text{min}} \sim \frac{2\pi}{L}$ are undersampled causing this issue to be most severe on these larger scales. This can be treated by running an ensemble of many simulations, varying the initial conditions, and taking an average [47], however this comes at a great computational expense. One technique for mitigating this is to average over only a pair of simulations, which have "paired-and-fixed" initial conditions. Essentially, the initial Gaussian random density fields that are used to generate the initial conditions of the pair of simulations are fixed to have the same amplitude A_k, but their phases ϕ_k shifted by π. While this technique requires the additional expense of a second simulation, it has been shown to deliver reliable predictions of a variety of quantities [48], and can achieve similar accuracy as averaging over as much as 50 simulations [49].

Because of the usage of a finite number of discrete particles, N-body simulations produce a small overestimation of the power spectrum that stems from the correlation of particles with themselves. This is called the "shot-noise" and it produces a scale-independent contribution to the power spectrum of $P_{\text{shot}}(k) = V/N_{\text{part}}$ where V is the volume of the simulation box. Hence, this shot-noise term must be subtracted from the power spectrum computed from the simulation. This becomes increasingly relevant on smaller scales when the power spectrum decreases to the same order of magnitude as this contribution.

2.2.2 COLA simulations

The Co-moving Lagrangian Acceleration (COLA) [50, 51] method is a fast N-body method in which the large scale evolution is determined by second order LPT (2LPT) and the smaller scales are evolved using the PM algorithm. This is accomplished by first decomposing the position of a particle into the LPT

solution and a residual piece:

$$\boldsymbol{x} = \boldsymbol{x}_{\rm LPT} + \boldsymbol{x}_{\rm res} \, . \tag{2.11}$$

The equations solved by a PM N-body code then consequently become:

$$\frac{{\rm d}\boldsymbol{x}}{{\rm d}t} = \frac{{\rm d}\boldsymbol{x}_{\rm LPT}}{{\rm d}t} + \boldsymbol{v}_{\rm res} \, , \tag{2.12a}$$

$$\frac{{\rm d}\boldsymbol{v}_{\rm res}}{{\rm d}t} = -\boldsymbol{\nabla}\Phi - \frac{{\rm d}^2\boldsymbol{x}_{\rm LPT}}{{\rm d}t^2} \, , \tag{2.12b}$$

where $\boldsymbol{v}_{\rm res} \equiv \dot{\boldsymbol{x}}_{\rm res}$. Therefore the code evolves $\boldsymbol{x}$ and $\boldsymbol{v}_{\rm res}$. The second term on the right hand side of Eq. 2.12b can be thought of as a fictitious force, measuring dynamics in the non-inertial frame of "LPT observers".

Eqs. 2.12a-2.12b are a perfectly exact decomposition, however they allow one to perform less time-steps in the simulation, giving COLA simulations a more "approximate" status. This is because normal N-body simulations rely on a large number of time-steps to build up the correct large scale structure. However, in the COLA method this is not necessary as we are directly feeding the simulation the correct large scale behavior via the 2LPT solution. The reduced number of time steps, together with the efficiency of the PM algorithm, are what make COLA simulations much more computationally affordable than high-resolution simulations[3].

2.3 Emulators of the Power Spectrum

We have determined that N-body simulations are an accurate tool for predicting the nonlinear power spectrum of a given cosmology. The question then arises how they could be incorporated into something like an MCMC where $\mathcal{O}(10^6)$ cosmologies are explored, or any other computational algorithm that requires a large search of the parameter space. Given the large computational expense of a high-resolution N-body simulation, it is unfeasible to perform one for every prediction needed in these analyses. Instead, a common approach is to run a much more manageable number of $\mathcal{O}(10^2)$ training simulations, and to utilize machine learning and regression techniques to build what are called emulators. Emulators allow for the quick inference of the power spectrum produced by a simulation at an arbitrary cosmology $\boldsymbol{\theta}$ based on the training set. Two of the most notable high-resolution N-body emulators currently available

[3]An estimate of the computational expense of some modern high-resolution simulation codes is provided in Sec. 2.1 of [52]. More on the expense of COLA is discussed in Sec. 4 of this thesis.

are the EuclidEmulator2 (EE2) [53] and the BACCO emulator [54]. Both of these emulators were trained for the $w_0 w_a$ model, discussed in Sec. 1.3. These two emulators distinguish themselves as they cover a wide range of the $w_0 w_a$ parameter space, as well as scales and redshifts.

Emulators can have many architectures and training choices, here we discuss some ideas which are later used in Sec. 4. The first decision one must confront in building an emulator of the power spectrum is how to choose the cosmologies at which to perform the training simulations, which can prove challenging due to the curse of dimensionality. A common method is to use Latin Hypercube (LH) sampling, which efficiently samples a space with a sparse number of points. An LH of N points is generated by dividing the range for each parameter in to N bins, and picking successive points randomly under the condition that no bin of any parameter is sampled from twice. This approach ensures a uniform sampling across each parameter individually, however the number of points sampled in a D-dimensional space is equal to the number sampled in each dimension N rather than N^D as in a grid.

2.3.1 Pre-processing

The next set of considerations in building an emulator are those concerning how to process the data prior to training. While the nonlinear power spectrum is the quantity of interest, it is advantageous to modify the variable slightly so as to reduce the features in the data that the emulator must learn. Therefore, a common starting point is to compute the boost factor $B(k, z)$ for each training cosmology, defined as the ratio of the nonlinear power spectrum to the linear version:

$$B(k, z) \equiv \frac{P_{\rm NL}(k, z)}{P_{\rm L}(k, z)} \,. \tag{2.13}$$

This variable has the advantage of being 1 on linear scales, isolating only the nonlinear behavior on small scales, while being easy to convert back to $P_{\rm NL}(k, z)$. Even more effective is to use the logarithm of the boost as is done in the EE2:

$$Q_{\rm EE2}(k, z) \equiv \log(B(k, z)) \,. \tag{2.14}$$

The BACCO emulator modifies this quantity by performing a smearing procedure on the baryonic acoustic oscillation (BAO) signal in the linear power spectrum. This is achieved by first computing a version of the linear power spectrum with the BAO signal removed $P_{\rm L}^{\rm NBAO}(k, z)$, which is essentially attained by identifying a bump in the sine-transform of the power spectrum and deleting it before inverse transforming back (see [54] and [55] for details). Then the smeared linear power spectrum is computed as a combination of the

linear power spectrum and the BAO-removed version by:

$$P_{\rm L}^{\rm S}(k,z) \equiv P_{\rm L}(k,z)G(k,z) + P_{\rm L}^{\rm NBAO}(k,z)(1-G(k,z))\,, \tag{2.15}$$

where

$$G(k,z) \equiv \exp(-0.5k^2/k_*^2(z))\,, \tag{2.16}$$

and

$$k_*^{-2}(z) \equiv (3\pi^2)^{-1}\int dk P_{\rm L}(k,z)\,. \tag{2.17}$$

The BACCO emulator then emulates the quantity:

$$Q_{\rm BACCO}(k,z) \equiv \log[P_{\rm NL}(k,z)/P_{\rm L}^{\rm S}(k,z)]\,. \tag{2.18}$$

It is then typical to normalize the input and output of the emulator to ensure no features are arbitrarily weighted more than others:

$$\hat{\theta}_j \equiv \frac{\theta_j - \theta_{j,\rm min}}{\theta_{j,\rm max} - \theta_{j,\rm min}}\quad, \tag{2.19}$$

$$\hat{Q}(k_i,z_j) \equiv \frac{Q(k_i,z_j) - Q_{\rm min}(k_i,z_j)}{Q_{\rm max}(k_i,z_j) - Q_{\rm min}(k_i,z_j)}\,, \tag{2.20}$$

where k_i and z_j are the bins in wavenumber and redshift that the emulation variable $Q(k,z)$ is stored in. In practice there are often $\mathcal{O}(10^3)$ different points in this $k-z$ grid that would each need to be emulated, leading to great computational cost. Therefore, another typical technique employed in emulators of the power spectrum is Principal Component Analysis (PCA) which can be used to reduce the dimensionality of the data. Principal components (PC) are eigenvectors of the sample covariance matrix. The principal components with the highest eigenvalues capture the directions of largest variance in the high-dimensional space. Typically a subspace formed by only a few PC's captures the vast majority of the variance of the data, hence projecting all data into this lower-dimensional space reduces computational complexity with minimal information loss.

Applying this technique to the training data, we first calculate the sample average across the training set:

$$\langle\hat{Q}\rangle(k_i,z_j) = \frac{1}{N_{\rm cosmo}}\sum_{\boldsymbol{\theta}} Q(k_i,z_j|\boldsymbol{\theta})\,, \tag{2.21}$$

where here we are briefly noting the dependence on the cosmological parame-

ters explicitly. We also compute the sample covariance $\mathcal{M}_j$:

$$(\mathcal{M}_j)_{ip} = \frac{1}{N_{\rm cosmo}-1}\sum_{\boldsymbol{\theta}}\Big[\big(\hat{Q}(k_i,z_j|\boldsymbol{\theta}) - \langle\hat{Q}\rangle(k_i,z_j)\big)\times \\ \big(\hat{Q}(k_p,z_j|\boldsymbol{\theta}) - \langle\hat{Q}\rangle(k_p,z_j)\big)\Big] \,. \quad (2.22)$$

The average is subtracted from the data in order to center it around zero. We then diagonalize each covariance matrix to obtain the $N_{\rm PC}$ eigenvectors $\mathcal{E}_{\ell j}(k_i)$ with the largest eigenvalues, and project the training data onto the subspace spanned by the PCs. Then the emulation variable can be written as:

$$\hat{Q}(k_i,z_j|\boldsymbol{\theta}) = \langle\hat{Q}\rangle(k_i,z_j) + \sum_{\ell=1}^{N_{\rm PC}}\alpha_{\ell j}(\boldsymbol{\theta})\mathcal{E}_{\ell j}(k_i)\,. \quad (2.23)$$

where the coefficients $\alpha_{\ell j}(\boldsymbol{\theta})$ are functions of the cosmological parameters that constitute the direct output of the emulator. The number of PC's utilized is determined by considering the trade off between computational expense and accuracy, due to the intrinsic information lost in the dimensionality reduction. The problem of emulating the power spectrum is then reduced to emulating the coefficients $\alpha(\boldsymbol{\theta})$ for each principal component and redshift.

2.3.2 Gaussian Process Regression

There are a number of machine learning and regression methods used to perform the task of emulation. Here I discuss Gaussian Process (GP) regression, used in the BACCO emulator, which is a non-parametric Bayesian method widely used due to its ability to handle high-dimensional inputs and to quantify prediction uncertainty. The fundamental assumption of GP regression is that any set of function values has a joint multivariate Gaussian distribution. In the present context the function of interest is an arbitrary principal component amplitude at an arbitrary redshift $\alpha(\boldsymbol{\theta})$ from Eq. 2.23. We may think of the training data as a vector $\boldsymbol{\alpha}_{\rm obs}$ of $N_{\rm train}$ observations of this function evaluated at the training inputs $\boldsymbol{\theta}_i$:

$$\alpha_{{\rm obs},i} = \alpha(\boldsymbol{\theta}_i) + \epsilon_i\,, \quad (2.24)$$

where ϵ_i is gaussian noise with noise variance σ_ϵ^2, so that $\epsilon_i \sim \mathcal{N}(0,\sigma_\epsilon^2)$. Without loss of generality we take the values of the function to be centered at 0.

The core of a GP regression model is the chosen kernel, which shapes the

covariance structure of the data. The most commonly used is the Radial Basis Function (RBF) kernel:

$$k(\boldsymbol{\theta}, \boldsymbol{\theta}') \equiv \sigma^2 \exp\left[-\frac{1}{2} \sum_{j=1}^{D} \frac{(\theta_j - \theta'_j)^2}{l_j^2} \right] . \tag{2.25}$$

which contains the hyperparameters σ^2 and the $\{l_j\}$, called the signal variance and the correlation lengths respectively. The training points provide a covariance matrix, $\boldsymbol{K}$, defined by $K_{pq} \equiv k(\boldsymbol{\theta}_p, \boldsymbol{\theta}_q)$. However, this matrix is modified to account for noise $\hat{\boldsymbol{K}} \equiv \boldsymbol{K} + \sigma_\epsilon^2 \boldsymbol{I}$, where $\boldsymbol{I}$ is the identity matrix. Maximizing the marginal likelihood fixes the hyperparameters σ^2, $\{l_j\}$, and σ_ϵ^2:

$$p(\boldsymbol{\alpha}_{\rm obs}|K) = \frac{1}{\sqrt{(2\pi)^{N_{\rm train}} \left|\hat{\boldsymbol{K}}\right|}} \exp\left[-\frac{1}{2} \boldsymbol{\alpha}_{\rm obs}^T \hat{\boldsymbol{K}}^{-1} \boldsymbol{\alpha}_{\rm obs} \right] . \tag{2.26}$$

We now consider a test point $\boldsymbol{\theta}^*$ at which we wish to infer the value of the function $\alpha(\boldsymbol{\theta}^*)$ based on the training points. Here we invoke the GP assumption that the value of the function at the test point is normally distributed along with the values at the training points:

$$\begin{bmatrix} \boldsymbol{\alpha}_{\rm obs} \\ \alpha(\boldsymbol{\theta}^*) \end{bmatrix} \sim \mathcal{N}\left(\begin{bmatrix} \mathbf{0} \\ 0 \end{bmatrix}, \begin{bmatrix} \hat{\boldsymbol{K}} & \boldsymbol{K}^* \\ \boldsymbol{K}^{*T} & K^{**} \end{bmatrix} \right) . \tag{2.27}$$

The vector $\boldsymbol{K}^*$ contains the covariances between the test point and training point function values $\boldsymbol{K}^*_p \equiv k(\boldsymbol{\theta}^*, \boldsymbol{\theta}_p)$. We also have $K^{**} \equiv k(\boldsymbol{\theta}^*, \boldsymbol{\theta}^*)$. The value of the function at $\boldsymbol{\theta}^*$, and the prediction uncertainty, are taken to be the mean and variance of the conditional distribution $p(\alpha(\boldsymbol{\theta}^*)|\{\boldsymbol{\theta}_i\}, \boldsymbol{\alpha}_{\rm obs})$ respectively:

$$\alpha_{\rm pred}(\boldsymbol{\theta}^*) = \boldsymbol{K}^{*T} \hat{\boldsymbol{K}}^{-1} \boldsymbol{\alpha}_{\rm obs} , \tag{2.28}$$

$$\sigma^2_{\rm pred} = K^{**} - \boldsymbol{K}^{*T} \hat{\boldsymbol{K}}^{-1} \boldsymbol{K}^* . \tag{2.29}$$

This regression is repeated for every principal component and redshift of interest, and one may recover the power spectrum from the set of $\alpha_{\ell j}$. In Sec. 4 we construct and validate GP emulators and compare to other methods.

Chapter 3

Early Dark Energy with Late-Time Marginalization

The Hubble tension is considered to be one of the most pressing problems in precision cosmology today. Exploring the possibility that it points to new physics remains a thriving area of research. In Sec. 1.8.1 I explained how an injection of an additional source of energy in the era before last scattering could bring the CMB inference of H_0 into agreement with local measurements. Indeed, this was the motivation for the proposal of Early Dark Energy (EDE) as a resolution to the Hubble tension in [56]. EDE corresponds to a class of models which consist of some added source of energy which peaks at a redshift z_c, reaching a fractional density $f_{\rm EDE}(z_c) \equiv \frac{\rho_{\rm EDE}(z_c)}{\rho_{\rm tot}(z_c)}$, before rapidly dissipating so as to not affect late-time cosmology. We sometimes write $f_{\rm EDE} \equiv f_{\rm EDE}(z_c)$ for simplicity.

In [56] it was shown that EDE was capable of resolving the Hubble tension. Using scalar fields to implement EDE, they found that under a combined dataset including data from Planck CMB as well as SH0ES, a better fit was obtained using EDE compared to ΛCDM. Interestingly, this result occurred for two different scalar field EDE models showing that the reduced tension was not strongly dependent on the particular model chosen, but more so on the general behavior of EDE. Additionally, CMB data from ACT showed a 3σ preference for EDE [57].

Following this, Ref. [58] explored whether EDE could serve as a cosmological concordance model, bringing the variety of cosmological measurements into agreement. The analysis added a number of other datasets, most notably LSS data from DES. Only a moderate preference for EDE was found when including the LSS data and SH0ES, however those results were in tension with the constraints provided by an analysis excluding SH0ES which did not show much preference for EDE. In addition, the analysis found that in order to

maintain a good fit to the CMB, EDE exacerbates the S_8 tension. Hence, the study did not find that EDE could restore cosmological concordance.

While those results challenge the viability of EDE, there have been a number of studies into supplementing EDE in order to handle both H_0 and S_8 tensions [59–68]. Therefore, this section covers our work presented in [69], which was aimed to test how a modified late-time expansion impacted the H_0 and S_8 tensions, and EDE parameter constraints overall. We use a piecewise constant equation of state $w(z)$ for the late ($z < 3$) dark energy modification, allowing for more general behavior. We employ a variety of datasets including CMB, BAO, SNe Ia, and LSS data from DES, including DES-Y3 which was recently released at the time of the project.

3.1 Dark Energy Models

In this work we tested two approaches to realizing EDE: with a scalar field and with an effective fluid. As discussed in Sec. 1.3, the scalar field dynamics are specified by the potential. For EDE it is desirable for the field to start in a "frozen" state, where the Hubble friction dominates, but then begins to evolve as H decreases with the universe's expansion. An "axion-like" potential is commonly used for such behavior:

$$V(\phi) = m^2 f^2 \Big[1 - \cos\Big(\frac{\phi}{f}\Big)\Big]^n . \tag{3.1}$$

The $n = 1$ case is a standard potential for axions, where m is the mass and f is the axion decay constant. At z_c, H and hence the Hubble friction decreases so that the field begins to oscillate. It then effectively behaves like a fluid with average equation of state:

$$w_n = \frac{n-1}{n+1} . \tag{3.2}$$

A closely related potential for scalar field EDE, which captures much of the behavior of the previous potential near the minimum, is the "Rock 'n' Roll" power law:

$$V(\phi) = V_0 \Big(\frac{\phi}{M_{\rm Pl}}\Big)^{2n} , \tag{3.3}$$

where $M_{\rm Pl}$ is the reduced Planck mass.

Due to the oscillatory behavior of the field near the minimum, numerically evolving the field can be cumbersome, hence it is common to use an effective fluid to mimic the behavior of these potentials. The energy density and

equation of state of this fluid can be represented as:

$$\rho_{\rm EDE}(z) = \frac{2\rho(z_c)}{1+([1+z_c]/[1+z])^{3(1+w_n)}}\,, \tag{3.4}$$

$$w_{\rm EDE}(z) = \frac{1+w_n}{1+([1+z]/[1+z_c])^{3(1+w_n)}} - 1\,. \tag{3.5}$$

At early times ($z >> z_c$), $w_{\rm EDE} \approx -1$ and the field acts as a cosmological constant, but once $z << z_c$ then $w_{\rm EDE}$ approaches w_n and the density decays as $a^{-3(1+w_n)}$, therefore exhibiting the desired EDE evolution.

We may compute the adiabatic sound speed of the fluid by:

$$c_a^2 \equiv \frac{\dot{P}_{\rm EDE}}{\dot{\rho}_{\rm EDE}} = w_{\rm EDE} - \frac{\dot{w}_{\rm EDE}}{3\mathcal{H}(1+w_{\rm EDE})}\,, \tag{3.6}$$

where here the dot is a derivative with respect to conformal time, and we have also used the conformal continuity equation (Eq. 1.10). The effective sound speed is computed following [70] with time-averaged quantities:

$$c_s^2(k,a) \equiv \frac{\langle \delta P_{\rm EDE}\rangle}{\langle \delta \rho_{\rm EDE}\rangle} = \frac{2a^2(n-1)\bar{\omega}^2 + k^2}{2a^2(n+1)\bar{\omega}^2 + k^2}\,, \tag{3.7}$$

where $\bar{\omega} = \bar{\omega}_0 a^{-3w_n}$ is the angular frequency of the oscillations, which decreases in time for $n > 1$. The frequency $\bar{\omega}_0$ depends on another parameter Θ_i (see [70]) which in the axion model corresponds to the initial field value $\Theta_i \leftrightarrow \phi_i/f$. Based on previous works [56, 71], in this project we only study $n = 3$. The effective fluid is then fixed by only three parameters: z_c, $f_{\rm EDE}$, and Θ_i. We set the initial field value while it is still frozen by the Hubble friction, at $a = 10^{-7}$.

Finally, as mentioned we use a piecewise constant equation of state $w(z)$ to modify the late-time expansion, starting at -1 with the subsequent epoch broken down into N redshift intervals, or bins:

$$w(z) = \begin{cases} w_0 & \text{if } 0 \le z < z_1\,, \\ \ldots & \\ w_{N-1} & \text{if } z_{n-1} \le z < z_N\,, \\ w_N = -1 & \text{if } z \ge z_N\,. \end{cases} \tag{3.8}$$

Smooth dark energy models only affect the background expansion history and are therefore specified by the equation of state $w(z)$. The piecewise constant function provides a good approximation of the equation of state for any dynamical dark energy provided that the bins are fine enough, so that our

results are general. We space the bins to capture mainly the late dark energy behavior in the Pantheon supernovae range $z \in [0.01, 2.3]$. We test using 3, 5, and 10 bins, with the $\{z_i\}$ from Eq. 3.8 being in each case:

- $\{0.7, 1.4, 2.1\}$;
- $\{0.5, 1.0, 1.5, 2.0, 3.0\}$;
- $\{0.3, 0.6, 0.9, 1.2, 1.5, 1.8, 2.1, 2.4, 2.7, 3.0\}$.

We use the parameterized post-Friedmann approach [72] to avoid instabilities due to crossing $w = -1$ or sharp discontinuities in our binned $w(z)$ function.

3.2 Datasets

Our analysis combines a variety of datasets, including data from the CMB, SNe Ia, LSS, and strong lensing. Here I outline each dataset with more details provided in our paper [69]:

- **CMB** - We primarily use ACT data [57], comprised of TT, EE, and TE power spectra, in the multipole range $\ell \in [600, 3000]$ for TT, and $\ell \in [350, 3000]$ for TE and EE. We impose the cut $\ell < 3000$ to prevent baryonic effects from impacting our results. We also use Planck 2018 [73] TT data for $\ell < 650$, and the EE spectrum for $\ell < 30$ in order to constrain τ. We refer to this combined dataset as "CMB", and we also supplement this with Planck 2018 CMB Lensing which we call "CMBL".

- **SNe Ia** - We use the Pantheon [74] SNe Ia sample with $z \in [0.01, 2.3]$, and refer to this dataset as "SNe".

- **LSS (Large-Scale Structure)** - We use a variety of BAO data, including the Six-degree Field Galaxy Survey (6dFGS) [75], the Sloan Digital Sky Survey (SDSS) Data Release 7 (DR7) main galaxy sample [76], and the SDSS Baryon Oscillation Spectroscopic Survey (BOSS) Data Release 12 (DR12) consensus sample [77], and refer to this dataset as "BAO". We also use DES 3x2pt data, sometimes only using cosmic shear, and use both DES-Year 1 (DES-Y1) [78] and DES-Year 3 (DES-Y3) [79].

- **Strong Lensing (SL)** - We opt to use strong lensing data from H0LiCOW (H_0 Lenses in COSMOGRAIL's Wellspring) [80–82] instead of SH0ES as it provides similar constraints on H_0 independently, while SH0ES is in strong tension with CMB constraints. We refer to this dataset as "SL".

Parameter	Min.	Max.
$\Omega_c h^2$	0.005	0.1
$\Omega_b h^2$	0.001	0.99
$100 \times \theta_*$	0.5	10
$\ln(10^{10} A_s)$	1.61	3.91
n_s	0.85	1.1
τ	0.01	0.8
$\log_{10}(z_c)$	3	4.3
$f_{\rm EDE}(z_c)$	0.001	0.5
Θ_i	0.1	3.1
w_0	-3	-0.1
w_n $(n \geq 1)$	-3	1

Table 3.1: The bounds on the priors of the cosmological parameters sampled in our analysis. Our priors are uniform distributions over each parameter within the specified ranges.

3.3 Analysis

In this section, I outline the methodology of our analysis of EDE with late-time modifications. We run MCMCs using the COCOA architecture [83] which combines the COBAYA code [84] for sampling and COSMOLIKE [85] for computing likelihoods. We use a modified version of the Einstein-Boltzmann solver CAMB along with HALOFIT [86], to obtain the nonlinear power spectrum, using the Casarini prescription [87, 88] to accommodate the late-time dark energy $w(z)$.

The cosmological parameters sampled in our analysis are θ_*, $\Omega_b h^2$, $\Omega_c h^2$, $\ln(10^{10} A_s)$, n_s, and τ; the EDE parameters $\log_{10}(z_c)$, $f_{\rm EDE}$, and Θ_i; and the binned $w(z)$ values. The priors on these cosmological parameters are listed in Table 3.1. We also sample over nuisance parameters from ACT and DES, with priors provided in their respective papers [20, 78, 79].

In order to isolate the effects of different datasets we run chains with five different dataset combinations:

- DC1 - CMB + BAO + SNe + CMBL;

Model/Dataset	H_0	$10 \times S_8$	$100 \times f_{\rm EDE}$
DC1			
ΛCDM	68.1 ± 0.50	8.20 ± 0.12	–
Axion-like	$71.6^{+1.3}_{-2.3}$	$8.35^{+0.17}_{-0.22}$	$10.6^{+2.7}_{-4.9}$
Rock 'n' Roll	$71.4^{+1.3}_{-2.0}$	$8.34^{+0.16}_{-0.19}$	$9.5^{+2.7}_{-3.6}$
Effective Fluid	$71.9^{+1.6}_{-2.1}$	$8.41^{+0.17}_{-0.20}$	$8.8^{+2.8}_{-3.5}$

Table 3.2: Cosmological parameter means and 68% bounds using our DC1 dataset, for three EDE models: Axion-like EDE, Rock 'n' Roll EDE and effective fluid EDE.

- DC2 - CMB + BAO + SNe;
- DC3 - CMB + BAO + SNe + CMBL + SL;
- DC4 - CMB + SNe + CMBL;
- DC5 - CMB + SNe + SL .

DC1 and DC4 differ only by the inclusion of BAO, while DC1 and DC2 differ by CMBL. DC3 contains SL which is in tension with CMB, and DC5 has SL and SNe which are in tension with CMB. We also test adding DES data to each of these datasets.

3.4 Results

I now present the results of our analysis of EDE models with late-time modifications. We begin the analysis by studying EDE-only constraints as a baseline, before proceeding to modify the late-time behavior with $w(z)$.

3.4.1 Early Dark Energy Only

Our first set of tests use EDE only to establish a baseline of comparison once we vary late-time behavior in the next section. We compare to previous results [57, 58] as well obtain new constraints due to our use of DES-Y3 data and restricting ACT power spectra to $\ell < 3000$.

Table 3.2 shows the mean and 68% limits on the parameters H_0, S_8, and $f_{\rm EDE}$ from an MCMC analysis of the DC1 dataset, for the Axion-like, Rock 'n' Roll, and fluid EDE models. We see that all three EDE models were successful in increasing the value of H_0. Furthermore, the constraints on $f_{\rm EDE}$

are consistent with the result from the ACT collaboration [57], which found $f_{\rm EDE} = 0.091^{+0.02}_{-0.036}$ but without the SNe data or the cutoff of $\ell < 3000$ in the Planck TT spectrum. As all three EDE models provide similar constraints, we simply use the fluid EDE model in future tests unless otherwise specified.

The 2D contours of the posterior are shown in Fig. 3.1, where we compare ΛCDM and fluid EDE constraints using DC1 with and without DES-Y3 data. From the figure it is clear that EDE increased the mean value of H_0 relative to ΛCDM in all cases, bringing the value in closer agreement with local measurements. However, under DC1, EDE also increased the mean value of S_8 from 0.820 ± 0.012 compared to $0.840^{+0.018}_{-0.02}$ in ΛCDM, worsening the S_8 tension relative to the lower values measured by galaxy surveys.

With respect to goodness-of-fit, the contributions to the minimum χ^2 due to the CMB for each model was $\chi^{2(\Lambda{\rm CDM})}_{\rm CMB} = 966.3$ and $\chi^{2({\rm EDE})}_{\rm CMB} = 957.0$, giving a difference $\Delta\chi^2_{\rm CMB} \equiv \chi^{2({\rm EDE})}_{\rm CMB} - \chi^{2(\Lambda{\rm CDM})}_{\rm CMB} = -9.3$. Taking $\Delta\chi^2$ to be χ^2 distributed along with the three EDE parameters as three degrees of freedom, gives a 2.2σ result in favor of EDE.

We can assess tension between two sets of constraints on a given cosmological parameter θ using the following:

$$T \equiv \frac{|\langle\theta_1\rangle - \langle\theta_2\rangle|}{\sqrt{\sigma_1^2 + \sigma_2^2}}\,, \tag{3.9}$$

where $\langle\theta_i\rangle$ are the parameter means and σ_i^2 are the 68% bounds[1]. We refer to this as the "1D tension" as it only accounts for single parameter.

Fig. 3.2 plots the 1D tension for H_0 compared to the SH0ES [89] constraint, and S_8 compared to DES-Y3 [79], for ΛCDM and the three tested EDE models. Using the dataset DC1, all three EDE models successfully brought the H_0 1D tension below 1, while under ΛCDM it is 4.5. However, all three EDE models slightly increased the S_8 1D tension to 2.3-2.5, up from 2.0 under ΛCDM. Similar results were found from other datasets, and are included in Appendix A of [69].

In order to study the effect of LSS on EDE constraints we now consider the previous analysis of the DC1 dataset, but with the addition of DES-Y3 data. Previous studies have shown LSS data to lower the preference for EDE [58, 90]. Due to an internal tension in the DES-Y3 galaxy clustering analysis [35] when using the REDMAGIC lens sample, we not only conduct analyses 3x2pt data, but also using cosmic shear ($\xi_\pm$) only. However, between the 2D contours in Fig. 3.1 and the more complete summary listed in Table 3.3, we do not see

[1]We take the average of the upper and lower limits if the marginalized constraint is skewed.

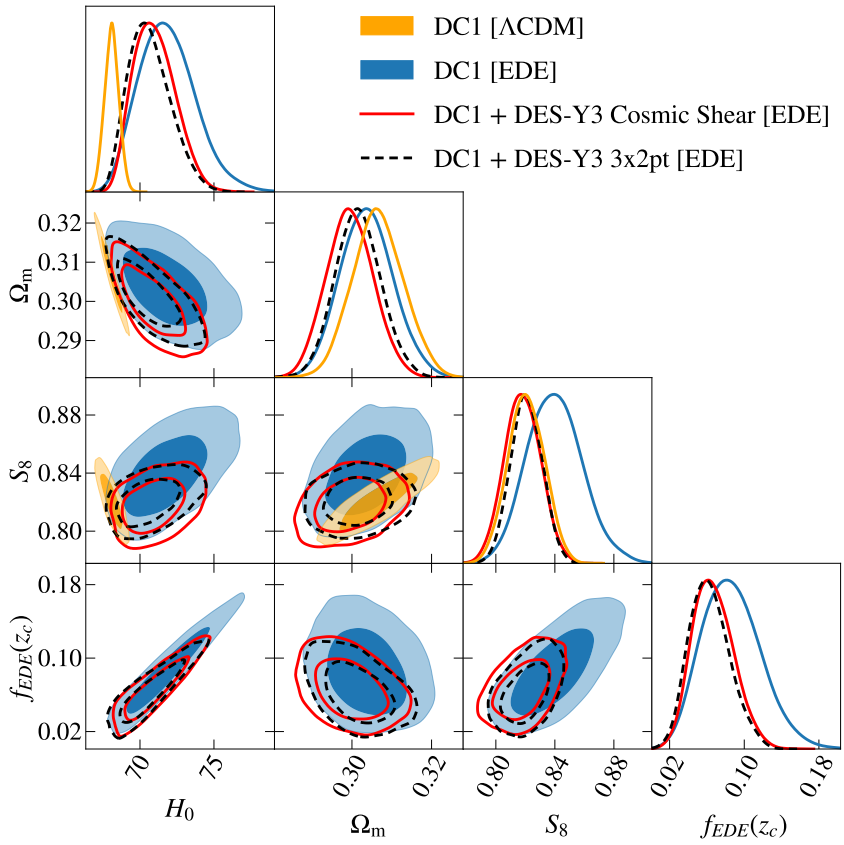


Figure 3.1: ΛCDM and EDE only constraints, when using DC1 and DES-Y3 datasets.

striking differences in the EDE constraints due to REDMAGIC internal tension.

We find using DC1:

$$\begin{aligned} f_{\rm EDE} &= 0.088^{+0.028}_{-0.035}\ ({\rm DC1})\,, \\ f_{\rm EDE} &= 0.067^{+0.019}_{-0.025}\ ({\rm DC1{+}DES\text{-}Y3}\ \xi^{\pm})\,, \\ f_{\rm EDE} &= 0.063^{+0.019}_{-0.024}\ ({\rm DC1{+}DES\text{-}Y3\ 3x2pt})\,. \end{aligned} \tag{3.10}$$

Hence, its clear that the addition of LSS data lowered the preferred amount of EDE at recombination, which would result in an increase of the Hubble tension. The same effect is seen using the DC2 dataset:

$$\begin{aligned} f_{\rm EDE} &= 0.075^{+0.019}_{-0.030}\ ({\rm DC2{+}DES\text{-}Y3}\ \xi^{\pm})\,, \\ f_{\rm EDE} &= 0.068^{+0.020}_{-0.026}\ ({\rm DC2{+}DES\text{-}Y3\ 3x2pt})\,, \end{aligned} \tag{3.11}$$

where CMBL has been omitted. This trend is supported in Fig. 3.2 where

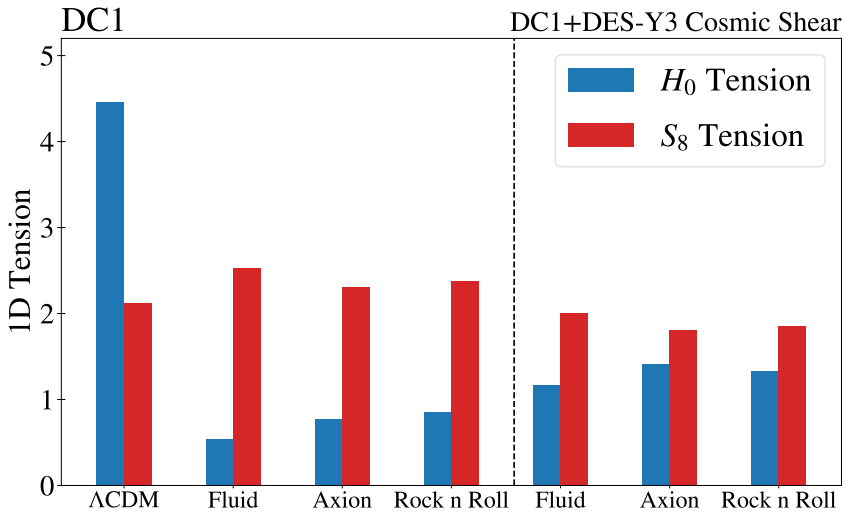


Figure 3.2: The 1D tension metric of Eq. 3.9 under different models, relative to the SH0ES H_0 constraint, and the DES-Y3 S_8 constraint. Under DC1, EDE models lower the H_0 tension to less than 1, while slightly increasing the S_8 tension. However, when DES-Y3 cosmic shear data is added, the S_8 tension lowers slightly at the cost of a lesser reduction in the H_0 tension.

we see the H_0 tension being larger when LSS data is included, though the S_8 tension is slightly lessened. In Fig. 3.3, we show $\chi^2_{\rm CMB}$ histograms both from MCMCs which used LSS data and which omitted it. We see that the inclusion of the DES data also worsened the fit to the CMB.

3.4.2 Adding Late-Time Modifications

We now study whether modifying the late-time behavior of dark energy can allow EDE to simultaneously have a favorable impact on the H_0 and S_8 tensions. We apply the piecewise constant equation of state $w(z)$ described in section Sec. 3.1. For constraints on the values of the $w(z)$ function, see Fig. 7 of our paper [69].

We ran MCMCs sampling over the values of $w(z)$ within each redshift bin, separately testing splitting the redshift range into 3, 5, or 10 bins. Figs. 3.4-3.5 summarize the constraints of the fluid EDE model combined with late-time modification on H_0, S_8, ω_m, and $f_{\rm EDE}$, showing the mean and 68% bounds for each parameter. Results are not only presented with and without the use of DES-Y3 data, but also using DES-Y1 in order to compare the effect of the updated data. We see from the figures that for datasets based on DC1, DC3, DC4, and DC5, the addition of the late-time modification $w(z)$ did not

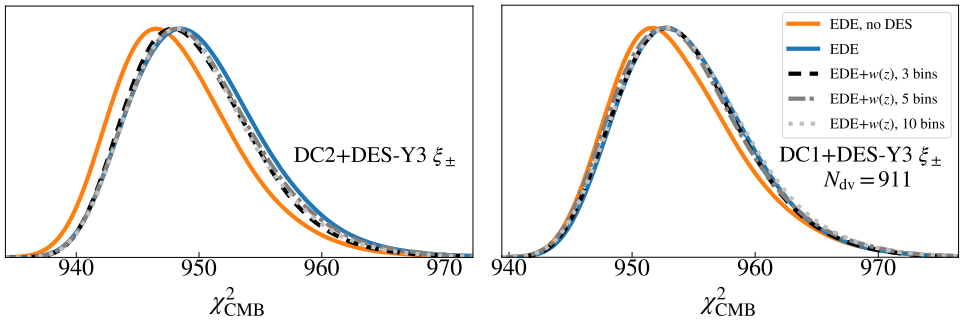


Figure 3.3: Histograms of $\chi^2_{\rm CMB}$ showing the goodness-of-fit of EDE with modified late-time behavior to the CMB.

significantly change the constraint on $f_{\rm EDE}$, using any number of redshift bins. Table 3.3 shows a summary of the constraints on H_0 , S_8, and $f_{\rm EDE}$ using datasets based on DC1 and DC2.

In the case of DC2, which is the DC1 dataset without CMBL, a slight change in the $f_{\rm EDE}$ and S_8 constraints did materialize with the addition of the late-time $w(z)$ modification. For all analyses where DES was included, the mean $f_{\rm EDE}$ increased by roughly 0.01 or approximately 0.5σ, and the mean S_8 decreased by roughly 0.4σ decreasing the S_8 tension. In Fig. 3.3 it is also apparent that under DC2 with DES-Y3 cosmic shear data, the addition of the late-time modification also improved the fit to the CMB. However, these changes in S_8 were not accompanied by an increase in H_0.

Model/Dataset	H_0	$10 \times S_8$	$100 \times f_{\rm EDE}$
DC1			
ΛCDM	$68.09^{+0.49}_{-0.49}$	8.21 ± 0.13	–
EDE	$71.9^{+1.6}_{-2.1}$	$8.40^{+0.18}_{-0.20}$	$8.7^{+2.8}_{-3.5}$
EDE + 3-bin $w(z)$	$71.8^{+1.7}_{-2.3}$	8.41 ± 0.19	$8.7^{+2.9}_{-3.8}$
EDE + 5-bin $w(z)$	$71.8^{+1.7}_{-2.1}$	8.38 ± 0.19	$8.7^{+2.8}_{-3.5}$
EDE + 10-bin $w(z)$	$71.6^{+1.8}_{-2.1}$	$8.41^{+0.18}_{-0.20}$	$8.4^{+3.2}_{-3.6}$
DC1+DES-Y3 $\xi_\pm$			
EDE	$71.0^{+1.2}_{-1.6}$	8.18 ± 0.12	$6.7^{+1.9}_{-2.5}$
EDE + 3-bin $w(z)$	$70.6^{+1.3}_{-1.7}$	8.17 ± 0.13	$6.7^{+1.9}_{-2.7}$
EDE + 5-bin $w(z)$	$71.0^{+1.3}_{-1.9}$	8.17 ± 0.13	$7.2^{+2.0}_{-3.1}$
EDE + 10-bin $w(z)$	$70.9^{+1.4}_{-1.8}$	8.18 ± 0.13	$7.0^{+2.1}_{-2.9}$
DC1+DES-Y3 3x2pt			
EDE	$70.7^{+1.1}_{-1.6}$	8.21 ± 0.10	$6.3^{+1.9}_{-2.4}$
EDE + 3-bin $w(z)$	$70.3^{+1.3}_{-1.6}$	8.19 ± 0.11	$6.3^{+1.9}_{-2.5}$
EDE + 5-bin $w(z)$	$70.7^{+1.2}_{-1.6}$	8.19 ± 0.11	$6.6^{+1.9}_{-2.4}$
EDE + 10-bin $w(z)$	$70.6^{+1.2}_{-1.6}$	8.19 ± 0.11	$6.4^{+2.0}_{-2.6}$
DC2			
ΛCDM	$68.06^{+0.56}_{-0.56}$	8.22 ± 0.17	–
EDE	$73.3^{+2.1}_{-2.5}$	$8.53^{+0.27}_{-0.31}$	$11.2^{+3.6}_{-4.3}$
EDE + 3-bin $w(z)$	$73.0^{+2.1}_{-2.6}$	8.49 ± 0.41	$11.0^{+3.3}_{-4.1}$
EDE + 5-bin $w(z)$	$72.8^{+2.0}_{-2.5}$	8.38 ± 0.39	$10.7^{+3.3}_{-3.9}$
EDE + 10-bin $w(z)$	$72.9^{+2.1}_{-2.5}$	8.46 ± 0.40	$10.9^{+3.4}_{-3.9}$
DC2+DES-Y3 $\xi_\pm$			
EDE	$71.4^{+1.3}_{-2.1}$	8.11 ± 0.17	$7.5^{+1.9}_{-3.0}$
EDE + 3-bin $w(z)$	$71.2^{+1.6}_{-2.0}$	$8.03^{+0.19}_{-0.17}$	$8.6^{+2.4}_{-3.2}$
EDE + 5-bin $w(z)$	$71.2^{+1.6}_{-1.9}$	$8.02^{+0.20}_{-0.17}$	$8.4^{+2.4}_{-3.2}$
EDE + 10-bin $w(z)$	$71.3^{+1.6}_{-2.2}$	8.03 ± 0.19	$8.7^{+2.5}_{-3.5}$
DC2+DES-Y3 3x2pt			
EDE	$70.9^{+1.3}_{-1.9}$	8.15 ± 0.13	$6.8^{+2.0}_{-2.6}$
EDE + 3-bin $w(z)$	$70.9^{+1.5}_{-1.8}$	$8.12^{+0.15}_{-0.13}$	$8.0^{+2.1}_{-2.9}$
EDE + 5-bin $w(z)$	$71.1^{+1.5}_{-1.8}$	8.13 ± 0.14	$7.9^{+2.6}_{-2.6}$
EDE + 10-bin $w(z)$	$71.0^{+1.5}_{-1.9}$	8.12 ± 0.14	$7.9^{+2.2}_{-2.9}$

Table 3.3: Summary of H_0, S_8, and $f_{\rm EDE}$ constraints under the combined EDE and late=time $w(z)$ models, using DC1 and DC2 with and without DES-Y3 data.

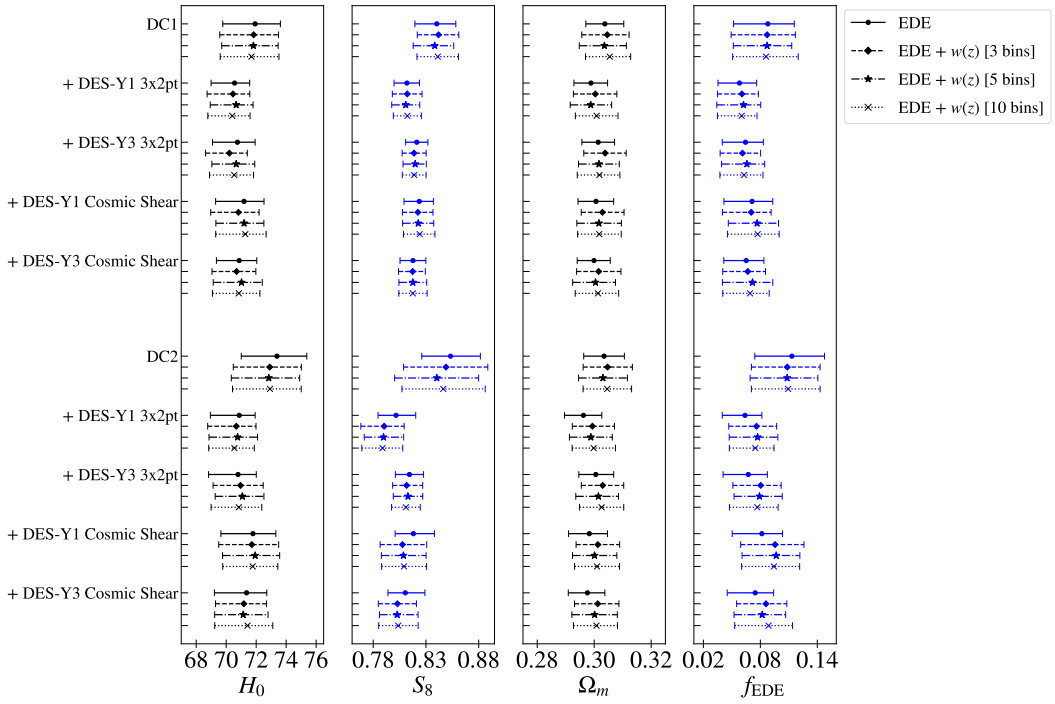


Figure 3.4: Mean and 68% bounds on H_0, S_8, Ω_m, and $f_{\rm EDE}$ using a fluid EDE model with modified late-time behavior $w(z)$. We use datasets DC1 and DC2, and repeat the analysis with DES-Y1 and DES-Y3 cosmic shear and 3x2pt data.

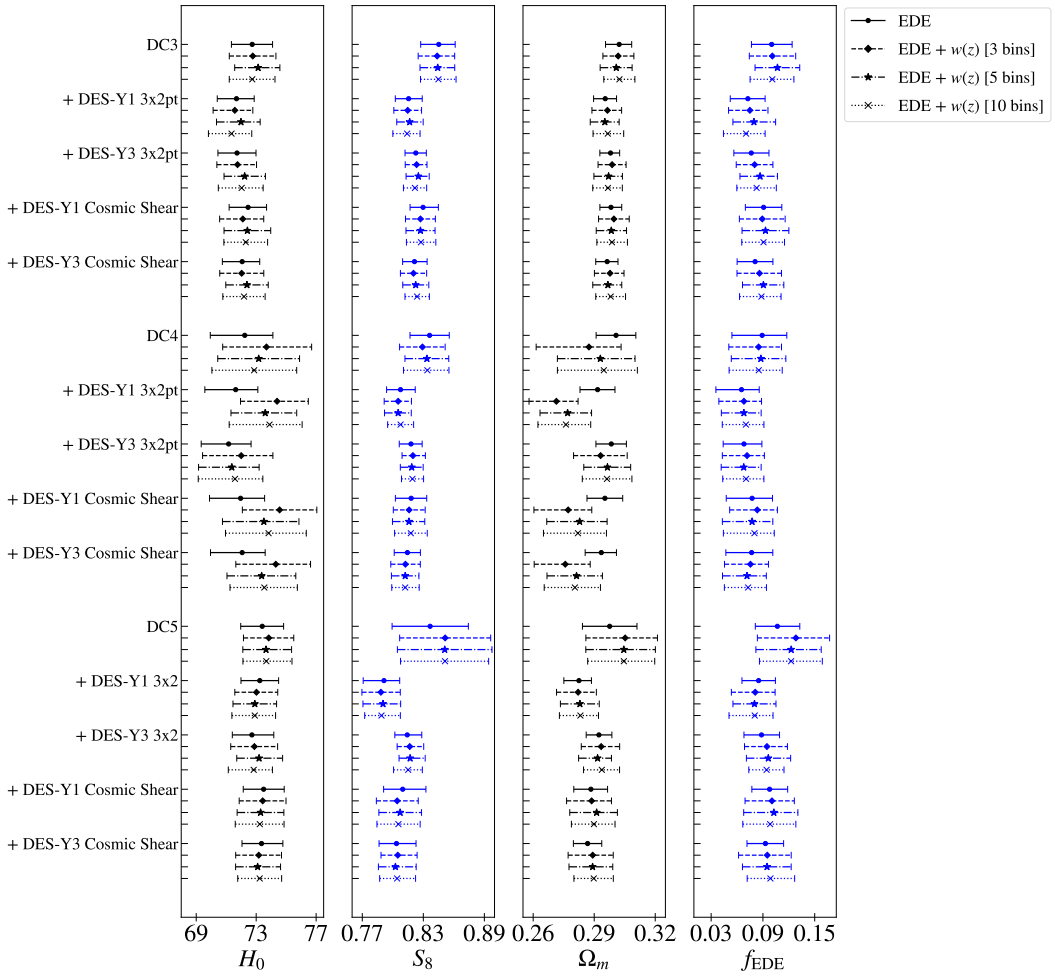


Figure 3.5: Continuation of Fig. 3.4 using the DC3, DC4, and DC5 datasets.

Chapter 4

Nonlinear modeling with COLA

Stage-IV surveys such as the Legacy Survey of Space and Time (LSST) [91] and Euclid [92] will provide a wealth of new information on small scales. This poses both an opportunity and a challenge for the exploration of beyond-ΛCDM models, due to the failure of linear perturbation theory on small scales, as discussed in Sec. 2.2. This is further complicated by the fact that large searches of the parameter space, such as with MCMCs (discussed in Sec. 2.1), require as many $\mathcal{O}(10^6)$ evaluations of the matter power spectrum to converge, placing tight computational constraints on the modeling tools required for Stage-IV analyses.

One straightforward approach to model smaller scales is to simply go to higher order in perturbation theory, however this requires performing computationally intensive convolution integrals. Recent work has gone into more efficiently computing these integrals [93], such as through the Effective Field Theory (EFT) approach [94–101] and its implementation [102–104], as well as its generalizations for some beyond-ΛCDM models [104–111]. However, these approaches only provide accurate predictions up to scales of $k \sim 0.2h\text{Mpc}^{-1}$.

Other methods have tried to utilize the precision of N-body simulations in computationally efficient ways. One approach to this is through the use of the halo model, which provides physically-motivated analytic formulas that can be fit to the results of a low number of simulations, allowing for fast predictions of the power spectrum up to scales of $k \sim 10\,h\text{Mpc}^{-1}$. This includes methods such as HALOFIT [86, 112, 113], HMCODE [114–116], and the halo reaction model approach REACT [117, 118].

In Sec. 2.3 I discussed emulators, which apply machine learning and regression algorithms to $\mathcal{O}(10^2)$ training simulations, allowing for the fast replication of the results of these simulations. Nevertheless, each beyond-ΛCDM model has a different parameter space over which the emulators must be trained, and running the requisite $\mathcal{O}(10^2)$ high-resolution N-body simulations requires com-

putational resources that typically are only available to large collaborations. To build EE2 for instance, required roughly 700,000 *node* hours [53]. Given the variety of cosmological models still of interest in the literature, relegating the production of these nonlinear modeling tools to a handful of collaborations would effectively imply that many models will never be able to make use of much of the new data from Stage-IV surveys.

For this reason, approximate or "fast" N-body techniques have garnered interest to reduce the computational expense of running simulations, at varying costs to their accuracy on small scales when compared to high-resolution simulations. In particular the COLA method, discussed in Sec. 2.2.2, was proposed as a means of generating training sets for emulators of the nonlinear power spectrum in [119]. Therefore, our work originally presented in [120] and reviewed in this section, tested this proposal by applying COLA emulators in a simulated LSST-Y1 cosmic shear analysis. We used the wCDM model as it is a simple extension of ΛCDM in which there is a suitable high-resolution N-body emulator to use as a benchmark, namely EE2. Given this, we take steps to improve the accuracy of the emulator including calibrating it with EE2 predictions, however the procedure serves as a template which can be replicated using other high-resolution prescriptions in other beyond-ΛCDM models.

COLA Simulation Settings

Previous works [121–123] have investigated many of the simulation settings discussed in Sec. 2.2, such as the initial redshift, placement of the time-steps, and force resolution. Many tests at the power spectrum level have been conducted [119, 123–125], where COLA has consistently met benchmark standards in comparisons with high-resolution N-body simulations, including in modified gravity models [123, 124, 126–131].

Therefore, in this investigation we were able to begin with a suite of settings which we dubbed *default-precision* (DP). However, we also tested more expensive settings aimed at improving accuracy on small scales which we dub *enhanced-precision* (EP) settings. These settings are summarized in Table 4.1. In the DP simulations, we used a box-size of $L = 1024\ h^{-1}$Mpc, a total number of particles of $N_{\rm part} = 1024^3$, and $N_{\rm mesh} = 2048^3$ cell grids, resulting in a force resolution $\ell_{\rm force} \equiv L/N_{\rm mesh}^{1/3} = 0.5\ h^{-1}$Mpc. Meanwhile, in the EP simulations we improved the force resolution of our simulations to $\ell_{\rm force} \approx 0.17\ h^{-1}$Mpc, by reducing the simulation box-size to $L = 512\ h^{-1}$Mpc and refining the number of mesh grids to $N_{\rm mesh} = 3072^3$.

The distribution of time-steps in the simulations are motivated by [119], where these time-steps were compared with PM N-body simulations which used the same mass and force resolution as in the EP COLA simulations. We

	Default-precision (DP)	*Enhanced-precision* (EP)
$N_{\rm part}$	1024^3	1024^3
L $[h^{-1}{\rm Mpc}]$	1024	512
$N_{\rm mesh}$	2048^3	3072^3
$M_{\rm part}$ $[h^{-1}M_\odot]$	8.4×10^{10}	1.1×10^{10}
$\ell_{\rm force}$ $[h^{-1}{\rm Mpc}]$	0.5	0.17

Table 4.1: Precision settings in our COLA simulations. We test two sets of precision settings, one dubbed *default-precision* and another dubbed *enhanced-precision* with a refined force-resolution.

began the simulations at an initial redshift of $z_{\rm initial} = 19$, and used 51 time-steps each with a time resolution in the scale factor of $\Delta a \approx 0.02$ as shown in Table 4.2. The initial displacement fields are generated using 2LPT.

We evolved particles using the "forward" approach [132], where the linear transfer functions are provided at each step of the simulation, ensuring the proper large scale dynamics. These transfer functions are provided in the N-body gauge [9, 133–135], as was done in the simulations used to construct EE2. The COLA simulations we run used the public COLA-FML[1] code, and the power spectra were computed using the on-the-fly code ComputePowerSpectra within the COLA-FML library.

The advantage of the COLA method is the reduction in computational expense of these simulations in comparison to a high-resolution simulation, hence we briefly discuss some benchmarks. Using 128 cores, the DP COLA simulations took about 0.7 wall-clock hours on average, and the EP simulations take about 1.5 wall-clock hours, both requiring $\mathcal{O}(100)$ CPU hours per simulation. This is a drastic reduction in comparison to the simulations that EE2 was trained on for example, which took $\mathcal{O}(10^5)$ CPU hours per simulation [53]. Another practical limitation that one must consider using the COLA approach is the memory usage. Our DP and EP simulations were run with 1.5TB and 3TB of total memory respectively, though we also found they are able to run with 1TB and 2TB. For this project, all simulations were run in the SeaWulf cluster at Stony Brook University and the GridUNESP cluster at the State University of São Paulo, demonstrating that our COLA emulator

[1] `https://github.com/HAWinther/FML`

Redshift Range	$N_{\rm steps}$
$19.0 \geq z > 3.0$	12
$3.0 \geq z > 2.0$	5
$2.0 \geq z > 1.0$	8
$1.0 \geq z > 0.5$	9
$0.5 \geq z \geq 0.0$	17

Table 4.2: Number of time-steps used in each redshift interval for all of our simulations, following [119]. The time steps are equally spaced in scale factor, a, for each interval. $N_{\rm steps}$ in each interval is chosen to maintain a step-size of $\Delta a \approx 0.02$.

approach does not require the computational resources of large collaborations.

Defining and Sampling the Parameter Space

In this work, the goal is to benchmark our COLA emulators with EE2, hence we run our simulations such that the EE2 parameter space is the region of validity of our emulators. However, as we are restricting our tests to the wCDM model, we restrict the dark energy energy equation of state parameter by setting $w_a = 0$ so that $w = w_0$ is a constant value. In addition we ran a training set of simulations for ΛCDM only in which we fixed $w_0 = -1$. We also follow the EE2 treatment of neutrinos using three degenerate massive neutrinos, but fixing their summed mass to the EE2 reference value $\Sigma m_\nu = 0.058$ eV. The bounds on region of validity of the emulators is then listed in Tab. 4.3.

While our analysis is restricted to this region of validity, our training simulations are run over a parameter space stretched symmetrically in each parameter sampled by a total of 10%, in order to improve emulation near the boundary of the desired region. Within this space, we utilize Latin Hypercube (LH) sampling to select the training points where we run simulations, ensuring a uniform distribution across each individual cosmological parameter and efficiently filling the space.

Before running COLA simulations, we use HALOFIT to inexpensively build prototypes of our COLA emulators, in order to determine the number of training cosmologies required for our desired accuracy. We also generate validation sets for ΛCDM and wCDM with $N_{\rm val} = 100$ LH points within the EE2 boundaries to measure the emulation errors. We emphasize that the low cost of

Parameter	Min.	Max.	EE2 Ref.
Ω_m	0.24	0.40	0.319
Ω_b	0.04	0.06	0.049
n_s	0.92	1.00	0.96
$A_s \times 10^9$	1.7	2.5	2.1
h	0.61	0.73	0.67
w	-1.3	-0.7	-1.0

Table 4.3: Boundaries of the parameter space in our analysis, based on the limits of EE2. Our emulators are trained to be valid in this region, which also serves as the prior for our MCMCs. We extend these boundaries by 5% in each direction when generating our training LH in order to improve emulation near the EE2 boundary. We also include the EE2 reference values which serve an important role in calibrating many of our COLA simulations, and in conducting our simulated LSST analysis.

COLA allows for a much higher number of training simulations compared to high-resolution N-body emulators. We found that when using $N_{\rm train}^{\Lambda{\rm CDM}} = 400$ training LH points for ΛCDM, and $N_{\rm train}^{w{\rm CDM}} = 500$ points for wCDM, we were able to emulate HALOFIT with an error compared to the validation sets of less than 0.3% for scales $10^{-2}\,h{\rm Mpc}^{-1} \leq k \leq \pi\,h{\rm Mpc}^{-1}$. Hence, these are the number of COLA training simulations run in each model.

4.1 Post-Processing COLA

As mentioned in Sec. 2.3, emulators of the power spectrum typically predict only nonlinear corrections based on the boost factor:

$$B(k, z|\boldsymbol{\theta}) \equiv \frac{P_{\rm NL}(k, z|\boldsymbol{\theta})}{P_{\rm L}(k, z|\boldsymbol{\theta})} \tag{4.1}$$

where here we show explicitly the dependence on the vector of cosmological parameters $\boldsymbol{\theta}$ though we sometimes omit it when the context is clear. The emulators in this work also are based on the boost factor, hence it is necessary to compute it from the training simulations. After subtracting the shot-noise term and computing the average nonlinear power spectrum from the paired-

and-fixed simulations, it is straightforward to directly compute the boost from the simulations $B_{\rm COLA}(k, z|\boldsymbol{\theta})$. However, different nonlinear prescriptions are known to have disagreements due to differences in their methodologies. Hence, it was suggested in the precursor to this work [119] to use a single boost from a high-resolution simulation as a reference to calibrate the boost from COLA:

$$\bar{B}(k, z|\boldsymbol{\theta}, \boldsymbol{\lambda}) \equiv B_{\rm high-res}(k, z|\boldsymbol{\lambda}) \times \left(\frac{B_{\rm COLA}(k, z|\boldsymbol{\theta})}{B_{\rm COLA}(k, z|\boldsymbol{\lambda})} \right) . \tag{4.2}$$

Here $\boldsymbol{\lambda}$, called the "reference cosmology", is the cosmology at which the high-resolution simulation is computed in order to improve the accuracy of the boost at the cosmology of interest $\boldsymbol{\theta}$. In Eq. 4.2 the ratio is taken between the boost from 2 COLA simulations so that any cosmology-independent defects in the boost that are inherent to COLA will cancel. In this way, the role of COLA can be seen as extending the high-resolution prescription from the reference to new cosmologies, which is especially interesting given that the cosmology $\boldsymbol{\theta}$ can contain parameters from a new extended cosmological model.

As EE2 is being used in this work as the benchmark for our emulators, we use it to compute the high-resolution prediction $B_{\rm high-res}(k, z|\boldsymbol{\lambda})$ which we also sometimes refer to as the "anchor". The first approach tested in this work was to use a single reference cosmology to calibrate all the training simulations, hence we used the EE2 reference cosmology listed in Table 4.3 located at the center of the parameter space. The reason for this choice is that in Eq. 4.2 only cosmology-independent COLA signals are canceled, so when a cosmology $\boldsymbol{\theta}$ is very far in the parameter space from the reference $\boldsymbol{\lambda}$, cosmology-dependent signals differ greatly between the two COLA predictions and fail to cancel.

Nevertheless, this problem motivated the idea to test using additional reference cosmologies spread throughout the parameter space, so that all of the training simulations could be calibrated with more proximate cosmologies. This is achieved by generalizing Eq. 4.2 to make use of an arbitrary number $N_{\rm refs}$ of reference cosmologies by taking a weighted sum:

$$\tilde{B}(k, z|\boldsymbol{\theta}, \boldsymbol{\lambda}_1, ..., \boldsymbol{\lambda}_{N_{\rm refs}}) \equiv \sum_{i=1}^{N_{\rm refs}} w_i \bar{B}(k, z|\boldsymbol{\theta}, \boldsymbol{\lambda}_i) . \tag{4.3}$$

The weights

$$w_i = \frac{\exp(-d_i^2/\sigma_d^2)}{\sum_{j=1}^{N_{\rm refs}} \exp(-d_j^2/\sigma_d^2)} , \tag{4.4}$$

are functions of the Euclidean distance in the D-dimensional parameter space

$$d_i^2 \equiv \sum_{j=1}^{D} (\hat{\theta}_j - \hat{\lambda}_{ij})^2 \,, \tag{4.5}$$

between the normalized $\boldsymbol{\theta}$ and the $\boldsymbol{\lambda}_i$ vectors (Eq. 2.20). The parameter σ_d in the weights is chosen during the process of building the emulator, see the discussion at the end of Sec. 4.3.

An essential consideration in the approach of adding multiple reference cosmologies is the added computational cost of running the requisite high-resolution simulation for each reference. After all, the COLA emulator approach is only useful in the context of extended models in which only expensive nonlinear prescriptions exist. Therefore, one approach tested in this work was to spread a limited number of 25 additional reference cosmologies across the wCDM parameter space, which we denote $N_{\rm refs}^{w\rm CDM} = 26$.

However, if one is interested in emulating a cosmological model which is an extension to ΛCDM, it is possible to limit the added cost of additional references by confining them within the ΛCDM subspace of the parameter space. This allows for the use of existing high-resolution emulators, or other fast ΛCDM prescriptions, to compute the anchors inexpensively and therefore allowing for a much greater number. Nevertheless, under the current approach of using Eq. 4.2 and Eq. 4.3 to incorporate the multiple references, each reference also requires the computational expense of a COLA simulation so the number cannot be arbitrarily large. Therefore, another approach tested in this work was to use 100 additional reference anchors confined to the ΛCDM subspace of our wCDM parameter space, an idea we refer to as $N_{\rm refs}^{\Lambda\rm CDM} = 101$.

4.2 Comparisons to EE2 at the Boost Level: 1, 26, 101 references

In this section, we compare the post-processed boost factors from the COLA simulations directly to the corresponding boosts from EE2. These comparisons provide important metrics indicating the scales and the extent to which our COLA approaches lose accuracy, as we are considering EE2 as the benchmark in this work.

Fig. 4.1 displays the disagreement between the post-processed boosts from the COLA simulations, and those from EE2 at $z = 0$ for various training sets. In each panel, we bounds on the lowest error 50%, 90%, and 100% of cosmologies of the respective training sets. Only training points that are

contained inside the EE2 boundary are able to be compared, therefore the ΛCDM panels consider 240 of the $N_{\rm train}^{\Lambda{\rm CDM}} = 400$ LH points, and the wCDM panels consider 279 of the $N_{\rm train}^{w{\rm CDM}} = 500$ LH points. In the left panels we restrict to simulations post-processed with only $N_{\rm refs} = 1$. One striking result is the similarity between the errors in the corresponding ΛCDM and wCDM training sets, indicating that the majority of the error in the COLA simulations are due to the ΛCDM parameters.

For both sets of simulation settings with $N_{\rm refs} = 1$, we see a similar spread of errors below $k \sim 0.5\,h{\rm Mpc}^{-1}$, with only a very slight increase in error on the largest scales for the EP simulations due to the smaller box size. However, there is a clear improvement in the EP simulations on smaller scales, where for $k \lesssim 1\,h{\rm Mpc}^{-1}$ the 90% bands remaining below 3% error. Additionally, for the DP wCDM cosmologies the percentage of runs with errors at $k = 1\,h{\rm Mpc}^{-1}$ outside the 2%, 3%, and 4% error thresholds, was 43.0%, 20.8% and 6.81%, respectively. These percentages more than halved for the EP simulations to 21.2%, 9.0%, and 2.9%.

The right panels of Fig. 4.1 show the effect of using Eq. 4.3 with 26 and 101 references. The top right panel shows the errors of the wCDM DP simulations using $N_{\rm refs}^{w{\rm CDM}} = 26$ anchors, in which 21.9%, 7.2%, and 1.5% of the training points had errors larger than 2%, 3% and 4% at $k = 1\,h{\rm Mpc}^{-1}$.

On the other hand, the third panel on the right of Fig. 4.1 shows the wCDM DP simulations processed with $N_{\rm refs}^{\Lambda{\rm CDM}} = 101$ references contained inside the ΛCDM subspace. Here we see the elimination of all errors above 4% at $k = 1\,h{\rm Mpc}^{-1}$, and only 13.2% and 1.8% of cosmologies outside the 2% and 3% error thresholds. For comparison, we include the second panel on the right the wCDM DP simulations using $N_{\rm refs}^{w{\rm CDM}} = 101$, so that we use the same large number of references but spread them throughout the entire parameter space. In this case 11.1%, 1.8%, and 0.4% of cosmologies had errors above 2%, 3% and 4% at $k = 1\,h{\rm Mpc}^{-1}$, showing similar results to $N_{\rm refs}^{\Lambda{\rm CDM}} = 101$ references. This again suggests that the main source of error introduced by our COLA methodology came in modeling the ΛCDM parameters, supporting the idea of using ΛCDM references.

We then combine the approaches of using the EP simulations with $N_{\rm refs}^{\Lambda{\rm CDM}} = 101$ references, and present the errors in the boost in the bottom right panel of Fig. 4.1. This produced 11.1%, 2.2%, and 1.8% of cosmologies having errors above 2%, 3% and 4% at $k = 1h{\rm Mpc}^{-1}$.

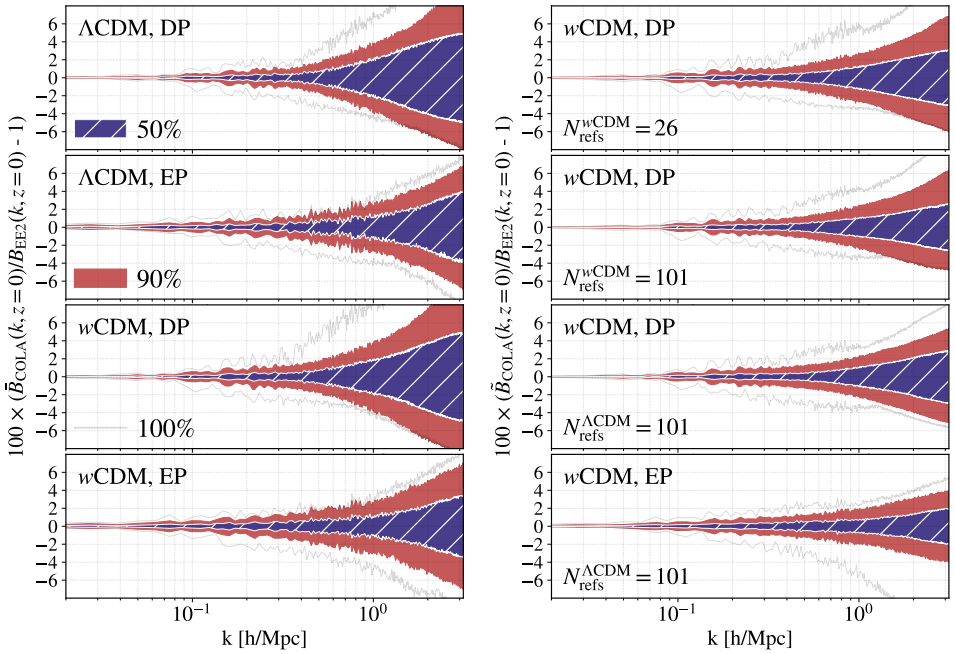


Figure 4.1: Bounds on the lowest error 50%, 90%, and 100% of training simulations, computed at $z = 0$ and each wavenumber k. The error is evaluated as the fractional difference between the post-processed boosts from the COLA simulations and the boosts from EE2. Each panel is identified by the cosmological model in which the simulations span, the precision settings, and the number of references, with the left panels corresponding to $N_{\rm refs} = 1$.

4.3 Emulator Validation

In Sec. 2.3 I discuss techniques used in the construction of emulators of the power spectrum in detail, and introduce GP regression. In this section, I show results from some selected GP emulators, and compare them to other emulators which used Neural Networks (NN), Polynomial Chaos Expansion (PCE), and a combination of the two discovered by a co-author during this project which was dubbed "Neural Polynominal Chaos Expansion" (NPCE).

Emulators were trained for each method using the pre-processing techniques described in Sec. 2.3. Essentially, the post-processed boosts from the simulations were used to compute the emulation variables using Eq. 2.14 or Eq. 2.18, and the dimensionality of the subsequent training data was reduced using PCA. For more details on the choices and parameters used for each emulation method, see [120].

Comparisons of the emulation errors at $z = 0$ are shown in Fig. 4.2. These

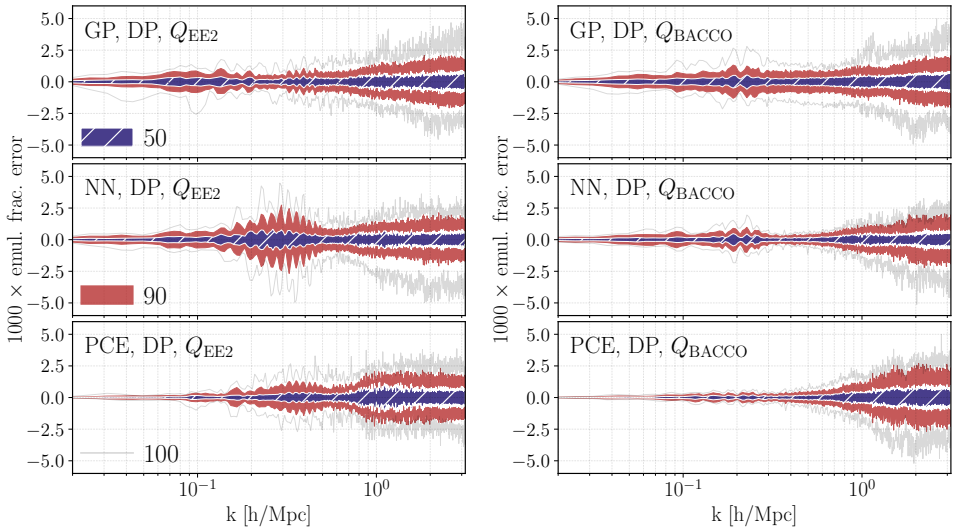


Figure 4.2: Emulation errors at $z = 0$ for our DP simulations with $N_{\rm refs} = 1$. We test three different emulation methods GP, NN, and PCE, while also comparing the effect of using the BAO-smearing procedure of the BACCO emulator.

errors were computed as the percent difference between the boost recovered from the emulator, and those computed directly from our test simulations. We trained the emulators with and without the BAO-smearing of the emulation variable discussed in Eq. 2.15, shown in the right and left panels respectively. The first striking result is that all three emulation methods compared show comparable emulation errors, with the errors staying below 0.5% on the scales shown $k \leq \pi\ h\text{Mpc}^{-1}$. Comparing the two panels, a clear improvement is apparent when the BAO-smearing algorithm is used, particularly for the NN and PCE emulators. Nevertheless, it is important to note that these errors are an order of magnitude smaller than those between the COLA simulations and EE2 as seen in the previous section, hence small emulation differences are not expected to have a severe impact on our final analysis.

However, when the same emulators were trained on the EP simulations, noticeably larger emulation errors resulted, shown in Fig. 4.3. The GP, NN, and PCE emulators all showed a larger emulation error approximately at or above 1% beyond $k \sim 1\ h\text{Mpc}^{-1}$. This increase is due to the increased k-range fed to the emulators from the EP simulations since they maintained better accuracy on small scales, up to $k_{\rm max} = 2\pi h\text{Mpc}^{-1}$ compared to $k_{\rm max} = \pi h\text{Mpc}^{-1}$ for the DP simulations. In order to improve these errors, our group developed the NPCE method, which essentially used a NN to correct the output from the PCE emulator. The NPCE method restored a comparable

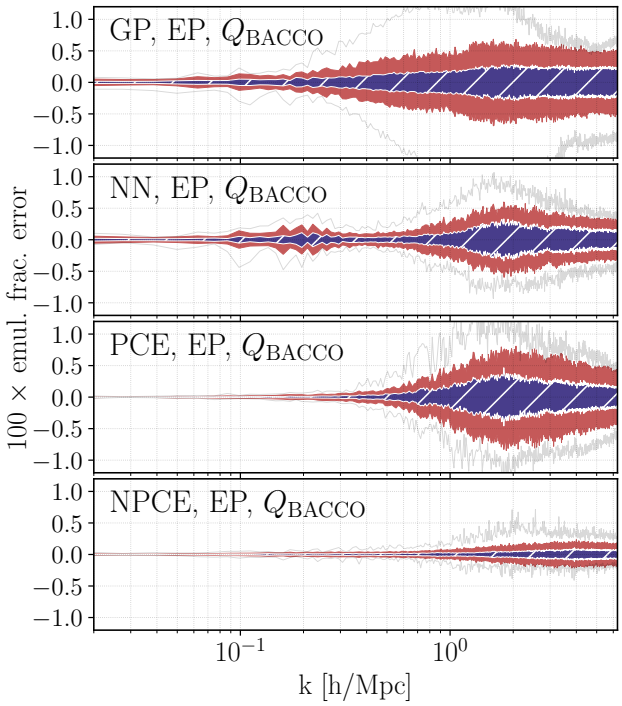


Figure 4.3: Emulation errors at $z = 0$ for our EP simulations with $N_{\rm refs} = 1$. The emulation errors reach about $\sim 1\%$ at $k = 1h{\rm Mpc}^{-1}$, an increase compared to the $\sim 0.5\%$ error in the DP case in Fig. 4.2 for GP, NN, and PCE emulators. However, the NPCE method appears to recover the lower errors.

level of emulation error as seen in the DP emulators, staying well within 0.5% error on all scales used.

As a final consideration regarding emulation, recall the parameter σ_d used in Eq. 4.4, which sets the distance scale at which reference cosmologies are weighted in Eq. 4.3. Figs. 4.2-4.3 only show emulation errors when $N_{\rm refs} = 1$ however pending the value of σ_d, the emulation errors can drastically change when multiple reference cosmologies are used. This is because the multiple references can lead to sudden changes in the modeling of the boost throughout the parameter space as different reference cosmologies become more proximate and thus more heavily weighted. This inconsistent modeling shows up in the emulation errors as the emulator is not explicitly given the location of the reference cosmologies, hence it can disagree with the validation simulations which indeed are calibrated explicitly using the reference cosmologies. Therefore, it is important to have a large enough value of σ_d so that the emulator does not rapidly change modeling throughout the parameter space, yet small enough so as to not contradict the rationale that more proximate reference

cosmologies should dominate the calibration in Eq. 4.3. We determine then the value of σ_d for each emulator by adjusting it and computing the emulation errors. For $N_{\rm refs} = 26$ and $N_{\rm refs} = 101$ we found values of $\sigma_d = 0.5$ and $\sigma_d = 0.3$ respectively maintained emulation errors very similar to the case of a single reference. This procedure can easily be followed in extended models so long as one has a validation set.

4.4 Analysis of LSST-Y1 Simulated Data

In this section I detail the methodology of our LSST-Y1 simulated cosmic shear analysis. In Sec. 1.7.3 I defined the cosmic shear observables $\xi_{\pm}^{ij}(\theta)$ and provided expressions for how to compute them from the power spectrum (Eq. 1.161 and Eq. 1.159). The survey specifications are based on the LSST DESC Science Requirement Document [136], and are shown in [120]. Our analysis is comprised of running MCMCs in the wCDM parameter space described in Table 4.3 using both COLA emulators and EE2 and measuring the bias between their parameter constraints as well as differences in their goodness-of-fit. We repeat these assessments around various regions of the prior and for multiple scale cuts, which we detail below.

In order to generate the fiducial data vectors of our analysis we use EE2 to compute the nonlinear spectrum, and add a Gaussian noise realization which was generated from the covariance matrix. We test the agreement between the emulators throughout the parameter space by generating our synthetic data vectors at various fiducial cosmologies. This is especially insightful due to the sensitivity of our emulators to the proximity of the reference cosmologies. One fiducial cosmology is placed at the EE2 reference cosmology, then four more are obtained by shifting values in the $\Omega_m - A_s$ plane, and four by shifting in the $\Omega_m - n_s$ plane. We denote these shifted cosmologies by only the parameters that are shifted from the reference values, and an arrow for the direction of the shift. The four cosmologies are distributed in each plane as 2×2 grids, consisting of the four combinations of "low" ($\hat{\theta} = 0.25$) and "high" ($\hat{\theta} = 0.75$) values of these parameters. In addition to those nine cosmologies, for the four of those which have a high value of Ω_m, we additionally shift the value of w to low and high values to obtain eight more fiducial cosmologies, for a total of 17. The specific low and high parameter values are listed in Table 4.4.

In order to establish how far into the nonlinear regime EE2 our COLA emulators can accurately probe, we repeat our analysis applying different scale cuts. These cuts are applied to the final data vector, therefore they are specified by the minimum angle considered in ξ_+ and ξ_-. The three cuts, from the most conservative to the most ambitious, are:

θ	$\theta^{\downarrow}$	$\theta^{\uparrow}$
Ω_m	0.28	0.36
$A_s \times 10^9$	1.9	2.3
n_s	0.94	0.98
w	-1.1	-0.9

Table 4.4: Cosmological parameter values used to create the fiducial cosmologies of our analyses. Parameters are labeled as "low" ($\downarrow$) or "high" ($\uparrow$) relative to how they are shifted from the EE2 reference values listed in Table 4.3.

$\langle z \rangle$	0.33	0.54	0.74	1.01	1.62
Cutoff 1	1.4	1.1	0.9	0.9	0.8
Cutoff 2	2.9	2.2	1.9	1.7	1.6
Cutoff 3	5.7	4.3	3.8	3.4	3.3

Table 4.5: Approximate wavenumbers k [hMpc^{-1}], corresponding to the three angular scale cuts in ξ_+ used in our LSST-like cosmic shear analysis, for each galaxy source bin.

- Cutoff 1 (C1): $\theta_{\rm min} = 22.0'$ for ξ_+ and $\theta_{\rm min} = 69.6'$ for ξ_-;
- Cutoff 2 (C2): $\theta_{\rm min} = 11.0'$ for ξ_+ and $\theta_{\rm min} = 34.8'$ for ξ_-;
- Cutoff 3 (C3): $\theta_{\rm min} = 5.5'$ for ξ_+ and $\theta_{\rm min} = 17.4'$ for ξ_-.

Approximate scales in terms of wavenumber k equivalent to these cutoffs can be found in Table 4.5 for a more direct comparison to the power spectrum.

Finally, we define metrics in order to quantify the agreement between our COLA emulators and EE2. We assess bias between constraints on single parameters by taking the difference in the parameter means from the two emulators and dividing by the standard deviation of the parameter difference:

$$\frac{\Delta\theta}{\sigma_\theta} = \frac{\langle\theta\rangle_{\rm COLA} - \langle\theta\rangle_{\rm EE2}}{\sqrt{\sigma^2_{\theta,\rm EE2} + \sigma^2_{\theta,\rm COLA}}} \,. \tag{4.6}$$

We refer to this as the "1D figure of bias", similar to Eq. 3.9, as it measures the bias using only one cosmological parameter. For a more complete figure of

bias we generalize this metric to include multiple parameters, accounting for their degeneracies by:

$$\mathrm{FoB}(\boldsymbol{\theta}) = [\Delta \langle \boldsymbol{\theta} \rangle^{\mathrm{T}} \cdot (C_{\mathrm{COLA}} + C_{\mathrm{EE2}})^{-1} \cdot \Delta \langle \boldsymbol{\theta} \rangle]^{1/2} \,, \tag{4.7}$$

We compute this metric using the six cosmological parameters we sample in the emulator $\boldsymbol{\theta}$=(Ω_m, Ω_b, n_s, A_s, h, w), hence we refer to this as the "6D figure of bias". Following the DES-Y3 analysis [137], we target a value of the 6D FoB < 0.3.

In addition to low bias, another criteria to establish agreement between the emulators is that they maintain the same goodness-of-fit. We measure this by taking a representative sample of points from the EE2 chain and taking the difference in χ^2 values between the two emulators:

$$\Delta\chi^2 = \chi^2_{\mathrm{COLA}} - \chi^2_{\mathrm{EE2}} \,, \tag{4.8}$$

at all points in this sample, checking how many fall within a desired range of $|\Delta\chi^2| < 1$.

4.5 Results of Simulated LSST-Y1 Analysis for $N_{\mathrm{refs}} = 1, 26, 101$

Here I present the results of our LSST-Y1 simulated cosmic shear analysis using COLA emulators with $N_{\mathrm{refs}} = 1$, 26, and 101. Based on the emulation errors presented in Sec. 4.3 we chose the PCE and NPCE methods for DP and EP simulations respectively.

We begin with tests of a baseline emulator in which we use the DP settings and a single reference cosmology to calibrate the COLA simulations. This allows for a controlled exploration of the impact on the positioning of the reference cosmology to the bias of the COLA emulator. As a first test we ran a chain using the most aggressive Cutoff 3 with the EE2 reference cosmology as the fiducial cosmology. Given that Eq. 4.2 calibrates the COLA simulations such that they agree with EE2 near the reference, this emulator should exhibit its lowest bias in this scenario where the reference is the same as the fiducial cosmology. 2D contours from this test are shown in the left panel of Fig. 4.4, where we see excellent agreement between the COLA emulator and EE2. In particular, there was a low FoB= 0.11 which falls well below the desired limit of 0.3, and 66.5% of points fell within $|\Delta\chi^2| < 1$. Therefore, we see that this baseline COLA emulator has the ability to satisfy stringent criteria in terms of bias and goodness-of-fit, on the most aggressive scale cut, in this scenario

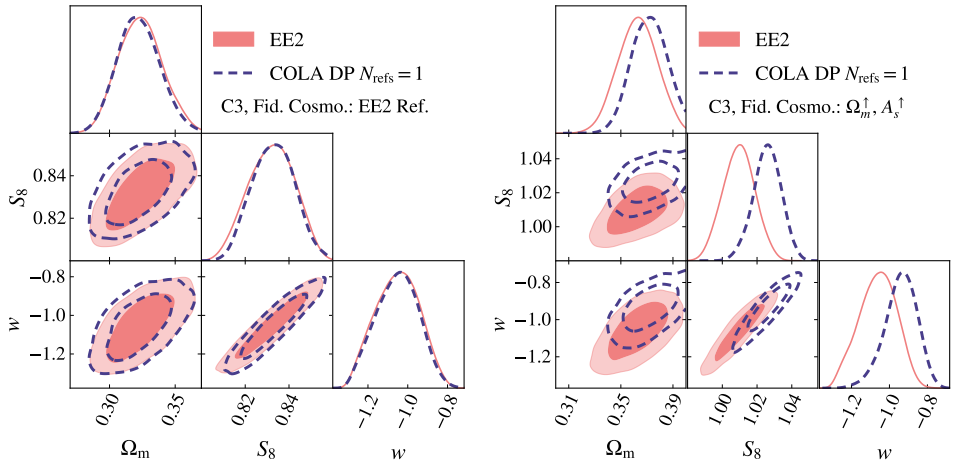


Figure 4.4: 2D contours comparing the DP $N_{\rm refs} = 1$ COLA emulator and EE2 parameter constraints, applying the most aggressive Cutoff 3. In the left panel the fiducial cosmology is equal to the reference cosmology of the emulator, while in the right panel the fiducial cosmology has shifted parameters ($\Omega_m^{\uparrow}$, $A_s^{\uparrow}$) leading to a value of $\sigma_8 = 0.93$ much higher than the reference $\sigma_8 = 0.82$.

where the reference cosmology is ideally placed inside the prior.

However, it is unrealistic to expect that one will be able to predict in advance the location of the best fit cosmologies, which is necessary in order to use it as a reference cosmology. After all, this is the purpose of performing the MCMC[2]. We therefore repeated the tests using the same emulator, but at different fiducial cosmologies around the parameter space. A noticeably different result occurred at the fiducial cosmology ($\Omega_m^{\uparrow}$, $A_s^{\uparrow}$), where we have shown the corresponding 2D contours in the right panel of Fig. 4.4. The baseline emulator shows large bias in this region of the parameter space far form the reference cosmology, with and FoB of 5.37 and only 4.1% of points within $|\Delta\chi^2| < 1$. Interestingly, when a new emulator was trained placing the single reference cosmology at the fiducial ($\Omega_m^{\uparrow}$, $A_s^{\uparrow}$) a low FoB of 0.40 was achieved, near the desired 0.3. Thus, it is clear that the location of reference cosmologies is crucial under our approach, with the potential of achieving the desired agreement with EE2 if one is able to optimally place the reference cosmology.

A more complete summary of these tests of the baseline emulator is presented in Fig. 4.5 which contains the 1D biases for the parameters Ω_m, S_8,

[2]It is possible to perform a preliminary exploration of the parameter space, such as by running an MCMC with linear scale cuts, to better identify a suitable reference cosmology before running the final MCMC.

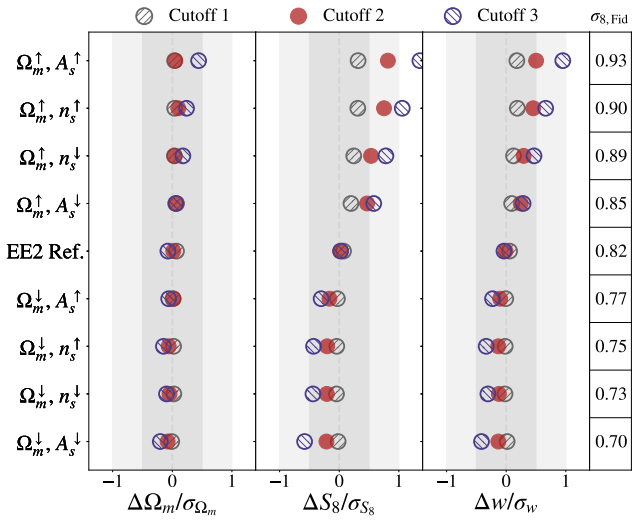


Figure 4.5: 1D biases using the DP $N_{\mathrm{refs}} = 1$ emulator, computed for a variety of fiducial cosmologies and all three scale cuts tested in this project. Fiducial cosmologies are ordered by value of σ_8, showing a clear correlation with bias.

and w for the nine ΛCDM fiducial cosmologies and all three scale cuts. One clear trend is the increase in the bias as more aggressive scale cuts are applied. Additionally, S_8 tends to be the most biased parameter as it is well constrained by cosmic shear measurements. More interestingly, it was found that the COLA biases were highly correlated with the parameter σ_8, therefore we ordered the fiducial cosmologies by their σ_8 values which are also listed in the figure.

In order to investigate whether other techniques can lead to an emulator that is able to deliver accurate modeling throughout the entire prior, we next test upgrading the baseline emulator by using the EP settings instead, maintaining $N_{\mathrm{refs}} = 1$. We repeat the previous tests, evaluating the bias of the emulator on all scale cuts, but restricting now only to the four high Ω_m fiducial cosmologies, which had the largest σ_8 and produced the highest bias. These comparisons are presented in the top panel of Fig. 4.6. We see a slight improvement to the DP emulator however the same trends persist and considerable bias remains in many cases. In particular we have the following biases for the most biased fiducial cosmology ($\Omega_m^\uparrow$, $A_s^\uparrow$):

- DP $N_{\mathrm{refs}} = 1$: $\Delta S_8/\sigma_{S_8} = 0.32$, FoB $= 1.12$ (C1);
- EP $N_{\mathrm{refs}} = 1$: $\Delta S_8/\sigma_{S_8} = 0.30$, FoB $= 0.98$ (C1);
- DP $N_{\mathrm{refs}} = 1$: $\Delta S_8/\sigma_{S_8} = 0.82$, FoB $= 3.18$ (C2);

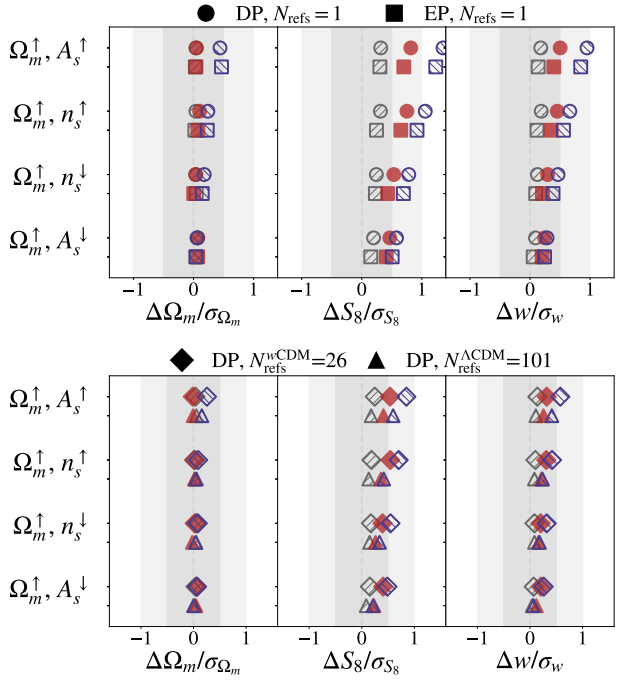


Figure 4.6: 1D biases for selected fiducial cosmologies with high Ω_m. The top panel displays the biases of the emulators trained on DP and EP settings, while the bottom panel displays the biases from the two multiple reference emulators with $N_{\rm refs}^{w\rm CDM} = 26$ and $N_{\rm refs}^{\Lambda\rm CDM} = 101$.

- EP $N_{\rm refs} = 1$: $\Delta S_8/\sigma_{S_8} = 0.70$, FoB $= 2.52$ (C2).

Therefore, while the EP emulator produced a slight decrease in bias, it is still not robust to significant shifts throughout the parameter space away from the reference cosmology. A similar result is seen with regards to goodness-of-fit, with $\Delta\chi^2$ data shown in Table 4.6. For the lower bias ($\Omega_m^\downarrow$, $A_s^\uparrow$) fiducial cosmology, 80.3% and 50.4% of points were within the range $|\Delta\chi^2| < 1$ for Cutoffs 2 and 3 respectively, while for the EP emulator that rose to 92.3% and 58.9%. However for the higher bias ($\Omega_m^\uparrow$, $A_s^\uparrow$) fiducial cosmology, there was negligible difference for all three scale cuts.

Exploring another approach for improving the COLA emulators we repeated the previous analysis using the $N_{\rm refs}^{w\rm CDM} = 26$ and $N_{\rm refs}^{\Lambda\rm CDM} = 101$ emulators, maintaining DP settings. We again test the more biased high Ω_m fiducial cosmologies, separately applying all three scale cuts. The resulting 1D biases are plotted in the bottom panel of Fig. 4.6. A comparison to the top panel shows that both of these approaches with multiple references consistently delivered low bias compared to either emulator which used a single reference.

	DP, 1	EP, 1	DP, 26 (wCDM)	DP, 101 (ΛCDM)
$\Omega_m^{\downarrow}$, $A_s^{\uparrow}$, C1	98.7%	98.9%	99.3%	99.2%
$\Omega_m^{\downarrow}$, $A_s^{\uparrow}$, C2	80.3%	92.3%	92.4%	96.0%
$\Omega_m^{\downarrow}$, $A_s^{\uparrow}$, C3	50.4%	58.9%	80.2%	83.7%
$\Omega_m^{\uparrow}$, $A_s^{\uparrow}$, C1	51.4%	48.2%	71.0%	77.8%
$\Omega_m^{\uparrow}$, $A_s^{\uparrow}$, C2	14.2%	17.0%	28.5%	35.8%
$\Omega_m^{\uparrow}$, $A_s^{\uparrow}$, C3	4.1%	4.3%	10.6%	22.6%

Table 4.6: Percentages of points satisfying the desired criteria of $|\chi^2_{\rm COLA} - \chi^2_{\rm EE2}| < 1$. We compute this for four emulators, at two fiducial cosmologies, and applying all three scale cuts. The points are obtained from thinning the EE2 chain with the corresponding fiducial cosmology and scale cut.

In addition, the approach of using a higher number of references confined to ΛCDM consistently shows lower biases compared to a lower number spread throughout the space. Revisiting the biases at the troublesome fiducial cosmology $(\Omega_m^{\uparrow}, A_s^{\uparrow})$, we now see more substantial improvements for Cutoffs 1 and 2:

- DP $N_{\rm refs}^{w{\rm CDM}} = 26$: $\Delta S_8/\sigma_{S_8} = 0.25$, FoB $= 0.91$ (C1);
- DP $N_{\rm refs}^{\Lambda{\rm CDM}} = 101$: $\Delta S_8/\sigma_{S_8} = 0.18$, FoB $= 0.69$ (C1);
- DP $N_{\rm refs}^{w{\rm CDM}} = 26$: $\Delta S_8/\sigma_{S_8} = 0.54$, FoB $= 2.17$ (C2);
- DP $N_{\rm refs}^{\Lambda{\rm CDM}} = 101$: $\Delta S_8/\sigma_{S_8} = 0.41$, FoB $= 1.61$ (C2).

Therefore, we see much lower biases employing these methods, with the $N_{\rm refs}^{\Lambda{\rm CDM}} = 101$ emulator outperforming the $N_{\rm refs}^{w{\rm CDM}} = 26$ emulator. This is consistent with the goodness-of-fit results for these emulators which are also shown in Table 4.6. These multiple reference emulators were able to make noticeable improvements in meeting the $|\Delta\chi^2| < 1$ criteria for the troublesome $(\Omega_m^{\uparrow}, A_s^{\uparrow})$ fiducial cosmology, improving from $\sim 50\%$ of points for the single reference emulators using Cutoff 1, to 71.0% for the $N_{\rm refs}^{w{\rm CDM}} = 26$ emulator, and 77.8% for the $N_{\rm refs}^{\Lambda{\rm CDM}} = 101$ emulator.

Nevertheless, the promise of these results for the $N_{\rm refs}^{\Lambda{\rm CDM}} = 101$ emulator is undermined by the fact that these fiducial cosmologies are contained inside the

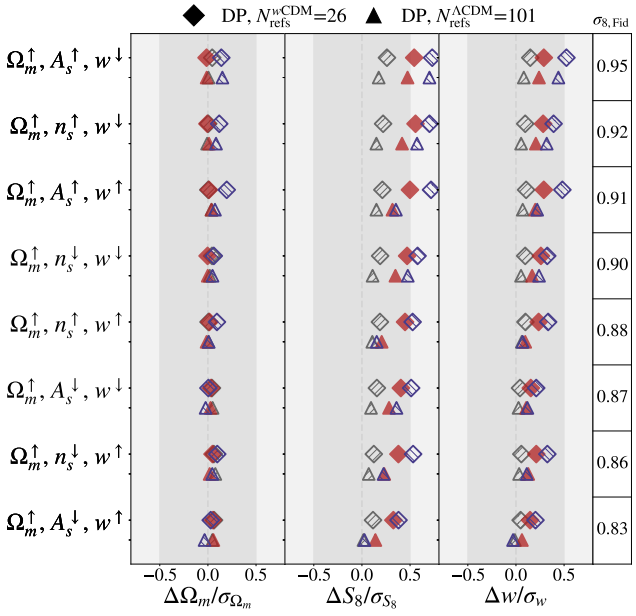


Figure 4.7: 1D biases for the $N_{\rm refs}^{w\rm CDM} = 26$ and $N_{\rm refs}^{\Lambda\rm CDM} = 101$ emulators for fiducial cosmologies outside of the ΛCDM region. These tests are intended to assess whether the previous results showing lower bias from the $N_{\rm refs}^{\Lambda\rm CDM} = 101$ emulator were due to an unfair advantage produced by placing the fiducial cosmologies inside ΛCDM.

ΛCDM subspace with w=-1. Even though the posterior extends far beyond this region, it is possible that this gives the emulator with a large number of ΛCDM references an advantage. In order to test if the ΛCDM references were effective at reducing the COLA emulator bias well outside of the ΛCDM region, we ran MCMCs with fiducial cosmologies shifted so that $w \neq -1$. From the resulting 1D biases summarized in Fig. 4.7, it is clear that the $N_{\rm refs}^{\Lambda\rm CDM} = 101$ emulator delivers the lower bias even in regions of the prior well outside of ΛCDM. From these tests the $(\Omega_m^{\uparrow}, A_s^{\uparrow}, w^{\downarrow})$ fiducial cosmology now produces the highest bias.

4.6 Emulating $B_{\rm COLA}(k, z)$: $N_{\rm refs}^{\Lambda\rm CDM} = 500, \infty$

As the $N_{\rm refs}^{\Lambda\rm CDM} = 101$ emulator is still unable to meet our stringent bias and goodness-of-fit criteria throughout the parameter space, yet has shown that a high number of ΛCDM references is a promising approach, we now consider computationally affordable ways to significantly increase $N_{\rm refs}^{\Lambda\rm CDM}$. From

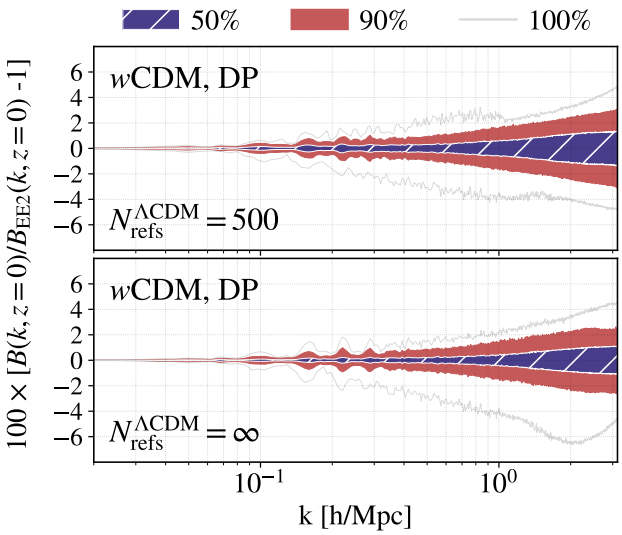


Figure 4.8: Repeating the comparisons shown in Fig. 4.1 between boosts from the post-processed COLA simulations and EE2 at $z = 0$, now using the $N_{\rm refs}^{\Lambda{\rm CDM}} = 500$ and $N_{\rm refs}^{\Lambda{\rm CDM}} = \infty$ approaches. The COLA boost for $N_{\rm refs}^{\Lambda{\rm CDM}} = 500$ is computed using $\tilde{B}(k, z)$ (Eq. 4.3) while for $N_{\rm refs}^{\Lambda{\rm CDM}} = \infty$ it is computed as $\bar{B}(k, z)$ (Eq. 4.9). For these comparisons the COLA boosts at the references are emulated.

Eq. 4.2, under the approach of ΛCDM references, the computational limit is due to the expense of the COLA simulation for each reference $B_{\rm COLA}(k, z|\boldsymbol{\lambda})$, as the anchors $B_{\rm high-res}(k, z|\boldsymbol{\lambda})$ are inexpensively computed with an emulator.

However, in light of our low emulation errors, it becomes feasible to emulate the uncalibrated $B_{\rm COLA}(k, z, |\boldsymbol{\lambda})$ from our training simulations, so that more simulations are not needed to get the COLA prediction for each reference. In that case, there is no significant computational expense for each additional reference allowing us to increase to a much higher number. Given that the references are used to calibrate the training set, we then test picking an optimally placed reference for each of the 500 training points, so we call this idea $N_{\rm refs}^{\Lambda{\rm CDM}} = 500$. Following the previous rationale of placing references to minimize the distance in the parameter space (Eq. 4.5) between the training points and reference points, the clear option is to then choose each reference to be the ΛCDM-projection ($\boldsymbol{\theta}_{\Lambda{\rm CDM}}$) of each training point $\boldsymbol{\theta}$. More specifically, $\boldsymbol{\theta}_{\Lambda{\rm CDM}}$ is obtained by setting the extended model parameters in the cosmology $\boldsymbol{\theta}$ to the values that recover ΛCDM. In the case of our wCDM analysis, this implies setting $w = -1$. Once the COLA predictions at these reference cosmologies are chosen, we compute Eq. 4.3 for every training point and train the emulator,

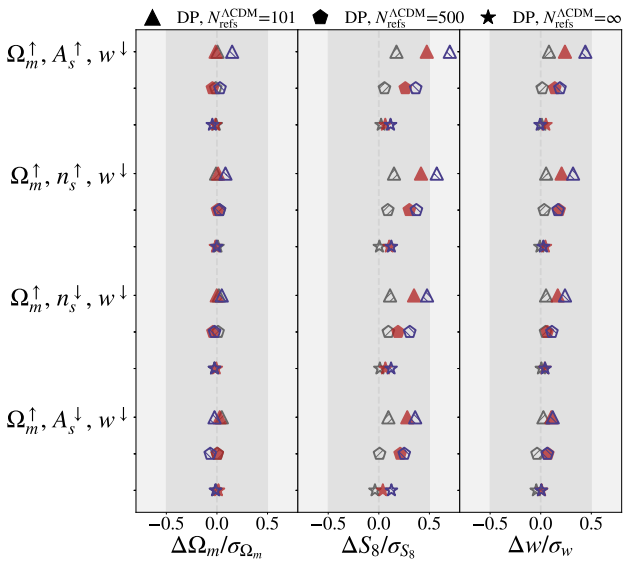


Figure 4.9: 1D biases using the $N_{\rm refs}^{\Lambda{\rm CDM}} = 500$ and $N_{\rm refs}^{\Lambda{\rm CDM}} = \infty$ methods at some of the most biased fiducial cosmologies from previous tests.

following our previous methodology for employing multiple references.

Notwithstanding, another avenue is opened through the use of an accurate emulator of $B_{\rm COLA}(k, z)$. With such an emulator all three boosts in Eq. 4.2 can be emulated separately. Then, instead of using one reference cosmology for each *training* point, it is possible to choose a new reference cosmology for each point one wishes to *predict*. In the context of an MCMC, this allows for the choice of reference cosmology to be optimized for every point sampled, specifically to be the ΛCDM-projection. As this effectively leads to an arbitrarily high number of references, we refer to this as the infinite references approach, $N_{\rm refs}^{\Lambda{\rm CDM}} = \infty$. I rewrite Eq. 4.2 in the current context:

$$\bar{B}(k, z|\boldsymbol{\theta}) = B_{\rm EE2}(k, z|\boldsymbol{\theta}_{\Lambda{\rm CDM}}) \times \left(\frac{B_{\rm COLA}(k, z|\boldsymbol{\theta})}{B_{\rm COLA}(k, z|\boldsymbol{\theta}_{\Lambda{\rm CDM}})} \right), \tag{4.9}$$

where I emphasize that the two COLA predictions are both the output of an emulator. This highlights the necessity of low emulation errors for this approach, as the emulation errors can compound due to the multiple predictions used. At this point, the COLA emulator's role has been minimized to effectively correct the EE2 ΛCDM prediction for only the extended model parameters at each point in the MCMC. Nevertheless, this is a sufficient task in order to perform nonlinear analyses in extensions to ΛCDM.

In Fig. 4.8 we show the comparisons of the COLA and EE2 boosts for the

	DP, 500 (ΛCDM)	DP, ∞ (ΛCDM)
$\Omega_m^{\uparrow}$, $A_s^{\uparrow}$, $w^{\downarrow}$, C1	89.1%	97.2%
$\Omega_m^{\uparrow}$, $A_s^{\uparrow}$, $w^{\downarrow}$, C2	54.4%	87.8%
$\Omega_m^{\uparrow}$, $A_s^{\uparrow}$, $w^{\downarrow}$, C3	35.9%	60.8%
$\Omega_m^{\uparrow}$, $A_s^{\downarrow}$, $w^{\downarrow}$, C1	88.4%	96.5%
$\Omega_m^{\uparrow}$, $A_s^{\downarrow}$, $w^{\downarrow}$, C2	58.4%	92.5%
$\Omega_m^{\uparrow}$, $A_s^{\downarrow}$, $w^{\downarrow}$, C3	43.6%	63.7%
$\Omega_m^{\uparrow}$, $n_s^{\uparrow}$, $w^{\downarrow}$, C1	86.5%	96.1%
$\Omega_m^{\uparrow}$, $n_s^{\uparrow}$, $w^{\downarrow}$, C2	50.2%	87.1%
$\Omega_m^{\uparrow}$, $n_s^{\uparrow}$, $w^{\downarrow}$, C3	32.5%	58.3%
$\Omega_m^{\uparrow}$, $n_s^{\downarrow}$, $w^{\downarrow}$, C1	90.4%	98.2%
$\Omega_m^{\uparrow}$, $n_s^{\downarrow}$, $w^{\downarrow}$, C2	62.4%	91.1%
$\Omega_m^{\uparrow}$, $n_s^{\downarrow}$, $w^{\downarrow}$, C3	43.0%	64.9%

Table 4.7: Repeating the $\Delta\chi^2$ analysis from Table 4.6 using the $N_{\rm refs}^{\Lambda{\rm CDM}} = 500$ and $N_{\rm refs}^{\Lambda{\rm CDM}} = \infty$ approaches.

training set at $z = 0$, as was done in Fig. 4.1, but now under the $N_{\rm refs}^{\Lambda{\rm CDM}} = 500$ and $N_{\rm refs}^{\Lambda{\rm CDM}} = \infty$ approaches. For these comparisons, the COLA prediction at the references are emulated but the direct COLA simulation output is used otherwise. We see a significant improvement in the errors at $k = 1$ for the $N_{\rm refs}^{\Lambda{\rm CDM}} = 500$ approach compared to all previous methods, with only 26.5%, and 2.5% of cosmologies above 1% and 2% error respectively. There is an even more significant improvement using the $N_{\rm refs}^{\Lambda{\rm CDM}} = \infty$ approach, where only 20.8%, and 4.3% of these cosmologies fell outside the 1% and 2% error bounds at $k = 1$.

We then continued our previous MCMC analysis employing these two approaches. As the low w fiducial cosmologies produced higher bias than the high w fiducial cosmologies in Fig. 4.7, we chose only those low w fiducial cosmologies for these tests. 1D biases for the $N_{\rm refs}^{\Lambda{\rm CDM}} = 500$ and $N_{\rm refs}^{\Lambda{\rm CDM}} = \infty$ approaches are shown in Fig. 4.9, where we now see significantly lower biases

using these methods when compared to $N_{\rm refs}^{\Lambda{\rm CDM}} = 101$. In particular, the $N_{\rm refs}^{\Lambda{\rm CDM}} = \infty$ method shows consistently low bias for all scale cuts and fiducial cosmologies tested. The highest biases obtained occurred at various fiducial cosmologies, and were:

- DP $N_{\rm refs}^{\Lambda{\rm CDM}} = 500$: $\Delta S_8/\sigma_{S_8} = 0.09$, FoB $= 0.31$ (C1);
- DP $N_{\rm refs}^{\Lambda{\rm CDM}} = \infty$: $\Delta S_8/\sigma_{S_8} = 0.04$, FoB $= 0.29$ (C1);
- DP $N_{\rm refs}^{\Lambda{\rm CDM}} = 500$: $\Delta S_8/\sigma_{S_8} = 0.26$, FoB $= 1.08$ (C2);
- DP $N_{\rm refs}^{\Lambda{\rm CDM}} = \infty$: $\Delta S_8/\sigma_{S_8} = 0.06$, FoB $= 0.29$ (C2);
- DP $N_{\rm refs}^{\Lambda{\rm CDM}} = 500$: $\Delta S_8/\sigma_{S_8} = 0.36$, FoB $= 1.26$ (C3);
- DP $N_{\rm refs}^{\Lambda{\rm CDM}} = \infty$: $\Delta S_8/\sigma_{S_8} = 0.12$, FoB $= 0.33$ (C3).

Whereas the $N_{\rm refs}^{\Lambda{\rm CDM}} = 500$ method only stayed near the bias requirement on Cutoff 1, the $N_{\rm refs}^{\Lambda{\rm CDM}} = \infty$ approach was on the border of meeting the desired FoB on Cutoff 3.

Furthermore, Table 4.7 shows much improved $\Delta\chi^2$ results for the $N_{\rm refs}^{\Lambda{\rm CDM}} = 500$ and $N_{\rm refs}^{\Lambda{\rm CDM}} = \infty$ methods. The $N_{\rm refs}^{\Lambda{\rm CDM}} = 500$ emulator maintained at least 86.5%, 50.2% and 32.5% of points within the desired $|\Delta\chi^2| < 1$ bounds for Cutoffs 1, 2, and 3 respectively. Meanwhile, the $N_{\rm refs}^{\Lambda{\rm CDM}} = \infty$ approach resulted in at least 96.1%, 87.1%, and 58.3% of points with the desired goodness-of-fit relative to EE2 for Cutoffs 1, 2, and 3. Therefore, the $N_{\rm refs}^{\Lambda{\rm CDM}} = \infty$ approach in particular essentially meets the stringent criteria we desired for Cutoffs 1 and 2, and does not stray far form these criteria even on Cutoff 3.

Chapter 5

Conclusion

In conclusion, there are a great number of models beyond-ΛCDM that need to be constrained, in order to pin down whether existing inconsistencies in ΛCDM, such as the H_0 and S_8 tensions, are clues of new physics. Early Dark Energy, for instance, has been put forth as a possible candidate to resolve the H_0 tension and has shown promise [56, 57]. However, LSS data has been shown to disfavor it due to its slight aggravation of the S_8 tension [58, 90]. In [69], our group explored whether adding a general smooth dark energy characterized by equation of state $w(z)$ could be used to modify the late-time behavior to mitigate this aggravation of the S_8 tension. We also expanded on previous EDE-only results, using new datasets and including the newly released DES-Y3 data.

Our analysis confirmed previous results showing that EDE can increase the value of H_0 and is preferred by datasets excluding LSS data. However, including LSS data lowered the preferred EDE contribution under a variety of different dataset combinations, due to the S_8 tension between LSS and CMB data. For instance, under the DC1 dataset we obtained $f_{\rm EDE} = 0.087^{+0.028}_{-0.035}$, compared to $f_{\rm EDE} = 0.067^{+0.019}_{-0.025}$ when DES-Y3 cosmic shear data is added, and $f_{\rm EDE} = 0.063^{+0.019}_{-0.023}$ using DES-Y3 3x2-point data.

These results persisted when marginalizing over late-time dark energy behavior. When marginalizing over as many as 10 bins in $w(z)$, using the DC1 dataset combined with DES-Y3 cosmic shear data, we found $f_{\rm EDE} = 0.070^{+0.021}_{-0.029}$, similar to the value without late-time modifications. This implies that more than a simple change to the background dark energy evolution is needed to restore the preference for EDE when LSS data is included, relative to when it is omitted. For EDE to resolve the Hubble tension, other models must be considered to suppress late-time growth of structure, such as using interacting dark energy [138, 139], or changing the clustering of matter [59, 140, 141].

Regarding the second project presented in [120], we tested COLA emula-

tors as a possible prescription for modeling the nonlinear power spectrum in beyond-ΛCDM models for upcoming Stage-IV surveys. Such analyses require modeling tools that are computationally affordable, accurate, and are straightforwardly generalizable to each cosmological model of interest. Without such tools, beyond-ΛCDM analyses will be forced to apply linear scale cuts, wasting the additional constraining power being provided by these surveys.

In order to test the COLA emulators, we conducted an LSST-Y1 simulated analysis of the wCDM model using them to model the nonlinear matter spectrum, comparing to the same analysis using EE2 as a benchmark. We assessed agreement between the two emulators by computing bias in the parameter constraints as well as comparing goodness-of-fit, applying three different nonlinear scale cuts, and repeating the analysis in various regions of the prior. We explored two primary methods to improve the accuracy of the COLA emulators, by increasing the force and mass resolutions of the emulators, and by calibrating the COLA predictions using EE2 predictions at reference cosmologies. The choice to calibrate with EE2 was solely intended for consistency with our use of EE2 as a benchmark, and we encourage investigations into the use of other high-resolution prescriptions to calibrate the COLA emulators.

We found that even the simplest COLA emulator tested, the *default-precision* settings together with 1 reference cosmology, was fairly consistent with EE2 on the most aggressive scale cut when tested in regions near that single reference cosmology. This result alone is of practical utility as often times researchers have information about the high-likelihood region of the posterior beforehand from previous analyses. It is also possible to investigate the posterior with a preliminary analysis, for example by using linear scale cuts, in order to identify an ideal location for the reference cosmology. However, this emulator exhibits strong bias in regions far from the reference, indicating other improvements are needed to have an emulator that is accurate throughout the prior.

Our results showed that the *enhanced-precision* settings we used provided only marginally better agreement with EE2 than did the *default-precision* settings, both in terms of bias and goodness-of-fit. We found greater improvement through the use of a limited number of reference cosmologies spread throughout the extended model parameter space $N_{\rm refs}^{w\rm CDM} = 26$, however, it still did not achieve the stringent criteria we desired. The approach of spreading a high number of reference cosmologies throughout the ΛCDM subspace proved much more effective at mitigating bias and improving goodness-of-fit, even in regions significantly outside of ΛCDM. While this idea is only able to be implemented in models that are strict *extensions* of ΛCDM, this is of great interest as this tends to be true of many beyond-ΛCDM models being studied.

The logical extreme of this idea, the $N_{\rm refs}^{\Lambda{\rm CDM}} = \infty$ approach, proved the most effective emulation approach, and was the only one tested to have met or come extremely close to passing our bias and goodness-of-fit criteria all throughout the prior. It is worth emphasizing that this idea was only made possible due to the low emulation errors we managed to achieve, which in turn was made possible due to the high number of training points afforded by the low computational expense of the COLA simulations. This is because the $N_{\rm refs}^{\Lambda{\rm CDM}} = \infty$ approach requires two calls of the COLA emulator, compounding the emulation error. While the role of COLA under this approach has effectively been reduced from modeling all parameters in the parameter space, to only the beyond-ΛCDM parameters, this is nevertheless a sufficient achievement for Stage-IV analyses of extensions to ΛCDM.

It is important to note that wCDM is only a mild extension to ΛCDM, containing only one additional parameter. Therefore, it is possible that even the $N_{\rm refs}^{\Lambda{\rm CDM}} = \infty$ method could degrade in performance for more exotic models with several additional parameters. Hence, there is reason to be conservative in applying the most aggressive scale cuts.

Bibliography

[1] N. Aghanim et al. Planck 2018 results. VI. Cosmological parameters. *Astron. Astrophys.*, 641:A6, September 2020. doi: 10.1051/0004-6361/201833910.

[2] Eleonora Di Valentino, Olga Mena, Supriya Pan, Luca Visinelli, Weiqiang Yang, Alessandro Melchiorri, David F Mota, Adam G Riess, and Joseph Silk. In the realm of the hubble tension—a review of solutions *. *Classical and Quantum Gravity*, 38(15):153001, July 2021. ISSN 1361-6382. doi: 10.1088/1361-6382/ac086d. URL `http://dx.doi.org/10.1088/1361-6382/ac086d`.

[3] Adam G. Riess, Stefano Casertano, Wenlong Yuan, J. Bradley Bowers, Lucas Macri, Joel C. Zinn, and Dan Scolnic. Cosmic distances calibrated to 1and hubble space telescope photometry of 75 milky way cepheids confirm tension with cdm. *The Astrophysical Journal Letters*, 908(1): L6, February 2021. ISSN 2041-8213. doi: 10.3847/2041-8213/abdbaf. URL `http://dx.doi.org/10.3847/2041-8213/abdbaf`.

[4] Elcio Abdalla, Guillermo Franco Abellán, Amin Aboubrahim, Adriano Agnello, Özgür Akarsu, Yashar Akrami, George Alestas, Daniel Aloni, Luca Amendola, Luis A. Anchordoqui, Richard I. Anderson, Nikki Arendse, Marika Asgari, Mario Ballardini, Vernon Barger, Spyros Basilakos, Ronaldo C. Batista, Elia S. Battistelli, Richard Battye, Micol Benetti, David Benisty, Asher Berlin, Paolo de Bernardis, Emanuele Berti, Bohdan Bidenko, Simon Birrer, John P. Blakeslee, Kimberly K. Boddy, Clecio R. Bom, Alexander Bonilla, Nicola Borghi, François R. Bouchet, Matteo Braglia, Thomas Buchert, Elizabeth Buckley-Geer, Erminia Calabrese, Robert R. Caldwell, David Camarena, Salvatore Capozziello, Stefano Casertano, Geoff C.-F. Chen, Jens Chluba, Angela Chen, Hsin-Yu Chen, Anton Chudaykin, Michele Cicoli, Craig J. Copi, Fred Courbin, Francis-Yan Cyr-Racine, Bożena Czerny, Maria Dainotti, Guido D'Amico, Anne-Christine Davis, Javier

de Cruz Pérez, Jaume de Haro, Jacques Delabrouille, Peter B. Denton, Suhail Dhawan, Keith R. Dienes, Eleonora Di Valentino, Pu Du, Dominique Eckert, Celia Escamilla-Rivera, Agnès Ferté, Fabio Finelli, Pablo Fosalba, Wendy L. Freedman, Noemi Frusciante, Enrique Gaztañaga, William Giarè, Elena Giusarma, Adrià Gómez-Valent, Will Handley, Ian Harrison, Luke Hart, Dhiraj Kumar Hazra, Alan Heavens, Asta Heinesen, Hendrik Hildebrandt, J. Colin Hill, Natalie B. Hogg, Daniel E. Holz, Deanna C. Hooper, Nikoo Hosseininejad, Dragan Huterer, Mustapha Ishak, Mikhail M. Ivanov, Andrew H. Jaffe, In Sung Jang, Karsten Jedamzik, Raul Jimenez, Melissa Joseph, Shahab Joudaki, Marc Kamionkowski, Tanvi Karwal, Lavrentios Kazantzidis, Ryan E. Keeley, Michael Klasen, Eiichiro Komatsu, Léon V.E. Koopmans, Suresh Kumar, Luca Lamagna, Ruth Lazkoz, Chung-Chi Lee, Julien Lesgourgues, Jackson Levi Said, Tiffany R. Lewis, Benjamin L'Huillier, Matteo Lucca, Roy Maartens, Lucas M. Macri, Danny Marfatia, Valerio Marra, Carlos J.A.P. Martins, Silvia Masi, Sabino Matarrese, Arindam Mazumdar, Alessandro Melchiorri, Olga Mena, Laura Mersini-Houghton, James Mertens, Dinko Milaković, Yuto Minami, Vivian Miranda, Cristian Moreno-Pulido, Michele Moresco, David F. Mota, Emil Mottola, Simone Mozzon, Jessica Muir, Ankan Mukherjee, Suvodip Mukherjee, Pavel Naselsky, Pran Nath, Savvas Nesseris, Florian Niedermann, Alessio Notari, Rafael C. Nunes, Eoin Ó Colgáin, Kayla A. Owens, Emre Özülker, Francesco Pace, Andronikos Paliathanasis, Antonella Palmese, Supriya Pan, Daniela Paoletti, Santiago E. Perez Bergliaffa, Leandros Perivolaropoulos, Dominic W. Pesce, Valeria Pettorino, Oliver H.E. Philcox, Levon Pogosian, Vivian Poulin, Gaspard Poulot, Marco Raveri, Mark J. Reid, Fabrizio Renzi, Adam G. Riess, Vivian I. Sabla, Paolo Salucci, Vincenzo Salzano, Emmanuel N. Saridakis, Bangalore S. Sathyaprakash, Martin Schmaltz, Nils Schöneberg, Dan Scolnic, Anjan A. Sen, Neelima Sehgal, Arman Shafieloo, M.M. Sheikh-Jabbari, Joseph Silk, Alessandra Silvestri, Foteini Skara, Martin S. Sloth, Marcelle Soares-Santos, Joan Solà Peracaula, Yu-Yang Songsheng, Jorge F. Soriano, Denitsa Staicova, Glenn D. Starkman, István Szapudi, Elsa M. Teixeira, Brooks Thomas, Tommaso Treu, Emery Trott, Carsten van de Bruck, J. Alberto Vazquez, Licia Verde, Luca Visinelli, Deng Wang, Jian-Min Wang, Shao-Jiang Wang, Richard Watkins, Scott Watson, John K. Webb, Neal Weiner, Amanda Weltman, Samuel J. Witte, Radosław Wojtak, Anil Kumar Yadav, Weiqiang Yang, Gong-Bo Zhao, and Miguel Zumalacárregui. Cosmology intertwined: A review of the particle physics, astrophysics, and cosmology associated with the cosmolog-

ical tensions and anomalies. *Journal of High Energy Astrophysics*, 34: 49–211, June 2022. ISSN 2214-4048. doi: 10.1016/j.jheap.2022.04.002. URL http://dx.doi.org/10.1016/j.jheap.2022.04.002.

[5] Daniel Baumann. *Cosmology*. Cambridge University Press, Cambridge, United Kingdom, 2022. ISBN 978-1-108-83807-8. doi: 10.1017/9781108937092. URL https://doi.org/10.1017/9781108937092.

[6] Michel Chevallier and David Polarski. Accelerating universes with scaling dark matter. *Int. J. Mod. Phys. D*, 10:213–224, 2001. doi: 10.1142/S0218271801000822.

[7] Eric V. Linder. Exploring the expansion history of the universe. *Phys. Rev. Lett.*, 90:091301, 2003. doi: 10.1103/PhysRevLett.90.091301.

[8] Wayne Hu and Daniel J. Eisenstein. Structure of structure formation theories. *Physical Review D*, 59(8), March 1999. ISSN 1089-4918. doi: 10.1103/physrevd.59.083509. URL http://dx.doi.org/10.1103/PhysRevD.59.083509.

[9] Christian Fidler, Cornelius Rampf, Thomas Tram, Robert Crittenden, Kazuya Koyama, et al. General relativistic corrections to N-body simulations and the Zel'dovich approximation. *Phys. Rev. D*, 92(12):123517, 2015. doi: 10.1103/PhysRevD.92.123517.

[10] Guilherme Brando, Kazuya Koyama, David Wands, Miguel Zumalacárregui, Ignacy Sawicki, and Emilio Bellini. Fully relativistic predictions in horndeski gravity from standard newtonian n-body simulations. *Journal of Cosmology and Astroparticle Physics*, 2021(09):024, September 2021. ISSN 1475-7516. doi: 10.1088/1475-7516/2021/09/024. URL http://dx.doi.org/10.1088/1475-7516/2021/09/024.

[11] F. R. Bouchet. Introductory overview of eulerian and lagrangian perturbation theories, 1996. URL https://arxiv.org/abs/astro-ph/9603013.

[12] Hans A. Winther. Nonlinear growth of structure: Lagrangian perturbation theory, 2024. URL https://cmb.wintherscoming.no/theory_nonlinear.php#lpt. Lecture notes, Theory of Nonlinear Growth of Structure.

[13] M. M. Phillips. The Absolute Magnitudes of Type IA Supernovae. , 413: L105, August 1993. doi: 10.1086/186970.

[14] S. Perlmutter, G. Aldering, G. Goldhaber, R. A. Knop, P. Nugent, P. G. Castro, S. Deustua, S. Fabbro, A. Goobar, D. E. Groom, I. M. Hook, A. G. Kim, M. Y. Kim, J. C. Lee, N. J. Nunes, R. Pain, C. R. Pennypacker, R. Quimby, C. Lidman, R. S. Ellis, M. Irwin, R. G. McMahon, P. Ruiz-Lapuente, N. Walton, B. Schaefer, B. J. Boyle, A. V. Filippenko, T. Matheson, A. S. Fruchter, N. Panagia, H. J. M. Newberg, W. J. Couch, and The Supernova Cosmology Project. Measurements of and from 42 high-redshift supernovae. *The Astrophysical Journal*, 517 (2):565–586, June 1999. ISSN 1538-4357. doi: 10.1086/307221. URL http://dx.doi.org/10.1086/307221.

[15] Adam G. Riess, Alexei V. Filippenko, Peter Challis, Alejandro Clocchiatti, Alan Diercks, Peter M. Garnavich, Ron L. Gilliland, Craig J. Hogan, Saurabh Jha, Robert P. Kirshner, B. Leibundgut, M. M. Phillips, David Reiss, Brian P. Schmidt, Robert A. Schommer, R. Chris Smith, J. Spyromilio, Christopher Stubbs, Nicholas B. Suntzeff, and John Tonry. Observational evidence from supernovae for an accelerating universe and a cosmological constant. *The Astronomical Journal*, 116(3): 1009–1038, September 1998. ISSN 0004-6256. doi: 10.1086/300499. URL http://dx.doi.org/10.1086/300499.

[16] Louise Breuval, Adam G. Riess, Stefano Casertano, Wenlong Yuan, Lucas M. Macri, Martino Romaniello, Yukei S. Murakami, Daniel Scolnic, Gagandeep S. Anand, and Igor Soszyński. Small magellanic cloud cepheids observed with the hubble space telescope provide a new anchor for the sh0es distance ladder. *The Astrophysical Journal*, 973(1): 30, September 2024. ISSN 1538-4357. doi: 10.3847/1538-4357/ad630e. URL http://dx.doi.org/10.3847/1538-4357/ad630e.

[17] Dillon Brout, Dan Scolnic, Brodie Popovic, Adam G. Riess, Anthony Carr, Joe Zuntz, Rick Kessler, Tamara M. Davis, Samuel Hinton, David Jones, W. D'Arcy Kenworthy, Erik R. Peterson, Khaled Said, Georgie Taylor, Noor Ali, Patrick Armstrong, Pranav Charvu, Arianna Dwomoh, Cole Meldorf, Antonella Palmese, Helen Qu, Benjamin M. Rose, Bruno Sanchez, Christopher W. Stubbs, Maria Vincenzi, Charlotte M. Wood, Peter J. Brown, Rebecca Chen, Ken Chambers, David A. Coulter, Mi Dai, Georgios Dimitriadis, Alexei V. Filippenko, Ryan J. Foley, Saurabh W. Jha, Lisa Kelsey, Robert P. Kirshner, Anais Möller, Jessie Muir, Seshadri Nadathur, Yen-Chen Pan, Armin Rest, Cesar Rojas-Bravo, Masao Sako, Matthew R. Siebert, Mat Smith, Benjamin E. Stahl, and Phil Wiseman. The pantheon+ analysis: Cosmological constraints. *The Astrophysical Journal*, 938(2):110,

October 2022. ISSN 1538-4357. doi: 10.3847/1538-4357/ac8e04. URL http://dx.doi.org/10.3847/1538-4357/ac8e04.

[18] D. S. Salopek. Consequences of the cobe satellite results for the inflationary scenario. *Phys. Rev. Lett.*, 69:3602–3605, Dec 1992. doi: 10.1103/PhysRevLett.69.3602. URL https://link.aps.org/doi/10.1103/PhysRevLett.69.3602.

[19] C. L. Bennett, M. Halpern, G. Hinshaw, N. Jarosik, A. Kogut, M. Limon, S. S. Meyer, L. Page, D. N. Spergel, G. S. Tucker, E. Wollack, E. L. Wright, C. Barnes, M. R. Greason, R. S. Hill, E. Komatsu, M. R. Nolta, N. Odegard, H. V. Peiris, L. Verde, and J. L. Weiland. First-year wilkinson microwave anisotropy probe (wmap) observations: Preliminary maps and basic results. *The Astrophysical Journal Supplement Series*, 148(1):1–27, September 2003. ISSN 1538-4365. doi: 10.1086/377253. URL http://dx.doi.org/10.1086/377253.

[20] Simone Aiola, Erminia Calabrese, Loïc Maurin, Sigurd Naess, Benjamin L. Schmitt, Maximilian H. Abitbol, Graeme E. Addison, Peter A. R. Ade, David Alonso, Mandana Amiri, Stefania Amodeo, Elio Angile, Jason E. Austermann, Taylor Baildon, Nick Battaglia, James A. Beall, Rachel Bean, Daniel T. Becker, J Richard Bond, Sarah Marie Bruno, Victoria Calafut, Luis E. Campusano, Felipe Carrero, Grace E. Chesmore, Hsiao mei Cho, Steve K. Choi, Susan E. Clark, Nicholas F. Cothard, Devin Crichton, Kevin T. Crowley, Omar Darwish, Rahul Datta, Edward V. Denison, Mark J. Devlin, Cody J. Duell, Shannon M. Duff, Adriaan J. Duivenvoorden, Jo Dunkley, Rolando Dünner, Thomas Essinger-Hileman, Max Fankhanel, Simone Ferraro, Anna E. Fox, Brittany Fuzia, Patricio A. Gallardo, Vera Gluscevic, Joseph E. Golec, Emily Grace, Megan Gralla, Yilun Guan, Kirsten Hall, Mark Halpern, Dongwon Han, Peter Hargrave, Matthew Hasselfield, Jakob M. Helton, Shawn Henderson, Brandon Hensley, J. Colin Hill, Gene C. Hilton, Matt Hilton, Adam D. Hincks, René e Hložek, Shuay-Pwu Patty Ho, Johannes Hubmayr, Kevin M. Huffenberger, John P. Hughes, Leopoldo Infante, Kent Irwin, Rebecca Jackson, Jeff Klein, Kenda Knowles, Brian Koopman, Arthur Kosowsky, Vincent Lakey, Dale Li, Yaqiong Li, Zack Li, Martine Lokken, Thibaut Louis, Marius Lungu, Amanda MacInnis, Mathew Madhavacheril, Felipe Maldonado, Maya Mallaby-Kay, Danica Marsden, Jeff McMahon, Felipe Menanteau, Kavilan Moodley, Tim Morton, Toshiya Namikawa, Federico Nati, Laura Newburgh, John P. Nibarger, Andrina Nicola, Michael D. Niemack, Michael R. Nolta, John Orlowski-Sherer, Lyman A. Page, Christine G. Pappas, Bruce Partridge, Phumlani

Phakathi, Giampaolo Pisano, Heather Prince, Roberto Puddu, Frank J. Qu, Jesus Rivera, Naomi Robertson, Felipe Rojas, Maria Salatino, Emmanuel Schaan, Alessandro Schillaci, Neelima Sehgal, Blake D. Sherwin, Carlos Sierra, Jon Sievers, Cristobal Sifon, Precious Sikhosana, Sara Simon, David N. Spergel, Suzanne T. Staggs, Jason Stevens, Emilie Storer, Dhaneshwar D. Sunder, Eric R. Switzer, Ben Thorne, Robert Thornton, Hy Trac, Jesse Treu, Carole Tucker, Leila R. Vale, Alexander Van Engelen, Jeff Van Lanen, Eve M. Vavagiakis, Kasey Wagoner, Yuhan Wang, Jonathan T. Ward, Edward J. Wollack, Zhilei Xu, Fernando Zago, and Ningfeng Zhu. The atacama cosmology telescope: DR4 maps and cosmological parameters. *Journal of Cosmology and Astroparticle Physics*, 2020(12):047–047, dec 2020. doi: 10.1088/1475-7516/2020/12/047. URL `https://doi.org/10.1088%2F1475-7516%2F2020%2F12%2F047`.

[21] J. E. Austermann, K. A. Aird, J. A. Beall, D. Becker, A. Bender, B. A. Benson, L. E. Bleem, J. Britton, J. E. Carlstrom, C. L. Chang, H. C. Chiang, H.-M. Cho, T. M. Crawford, A. T. Crites, A. Datesman, T. de Haan, M. A. Dobbs, E. M. George, N. W. Halverson, N. Harrington, J. W. Henning, G. C. Hilton, G. P. Holder, W. L. Holzapfel, S. Hoover, N. Huang, J. Hubmayr, K. D. Irwin, R. Keisler, J. Kennedy, L. Knox, A. T. Lee, E. Leitch, D. Li, M. Lueker, D. P. Marrone, J. J. McMahon, J. Mehl, S. S. Meyer, T. E. Montroy, T. Natoli, J. P. Nibarger, M. D. Niemack, V. Novosad, S. Padin, C. Pryke, C. L. Reichardt, J. E. Ruhl, B. R. Saliwanchik, J. T. Sayre, K. K. Schaffer, E. Shirokoff, A. A. Stark, K. Story, K. Vanderlinde, J. D. Vieira, G. Wang, R. Williamson, V. Yefremenko, K. W. Yoon, and O. Zahn. Sptpol: an instrument for cmb polarization measurements with the south pole telescope. In Wayne S. Holland, editor, *Millimeter, Submillimeter, and Far-Infrared Detectors and Instrumentation for Astronomy VI*. SPIE, September 2012. doi: 10.1117/12.927286. URL `http://dx.doi.org/10.1117/12.927286`.

[22] T. Schrabback, J. Hartlap, B. Joachimi, M. Kilbinger, P. Simon, et al. Evidence of the accelerated expansion of the Universe from weak lensing tomography with COSMOS. *Astron. Astrophys.*, 516:A63, June 2010. doi: 10.1051/0004-6361/200913577.

[23] Catherine Heymans, Emma Grocutt, Alan Heavens, Martin Kilbinger, Thomas D. Kitching, et al. CFHTLenS tomographic weak lensing cosmological parameter constraints: Mitigating the impact of intrinsic galaxy alignments. *Mon. Not. Roy. Astron. Soc.*, 432(3):2433–2453, July 2013. doi: 10.1093/mnras/stt601.

[24] Kyle S. Dawson, Jean-Paul Kneib, Will J. Percival, Shadab Alam, Franco D. Albareti, et al. The SDSS-IV Extended Baryon Oscillation Spectroscopic Survey: Overview and Early Data. *Astronomical Journal*, 151(2):44, February 2016. doi: 10.3847/0004-6256/151/2/44.

[25] M. James Jee, J. Anthony Tyson, Stefan Hilbert, Michael D. Schneider, Samuel Schmidt, and David Wittman. Cosmic Shear Results from the Deep Lens Survey. II. Full Cosmological Parameter Constraints from Tomography. , 824(2):77, June 2016. doi: 10.3847/0004-637X/824/2/77.

[26] M. A. Troxel, N. MacCrann, J. Zuntz, T. F. Eifler, E. Krause, et al. Dark Energy Survey Year 1 results: Cosmological constraints from cosmic shear. *Phys. Rev. D*, 98(4):043528, August 2018. doi: 10.1103/PhysRevD.98.043528.

[27] T. M. C. Abbott, F. B. Abdalla, A. Alarcon, J. Aleksić, S. Allam, et al. Dark Energy Survey year 1 results: Cosmological constraints from galaxy clustering and weak lensing. *Phys. Rev. D*, 98(4):043526, August 2018. doi: 10.1103/PhysRevD.98.043526.

[28] Chiaki Hikage, Masamune Oguri, Takashi Hamana, Surhud More, Rachel Mandelbaum, et al. Cosmology from cosmic shear power spectra with Subaru Hyper Suprime-Cam first-year data. *Publications of the Astronomical Society of Japan*, 71(2):43, April 2019. doi: 10.1093/pasj/psz010.

[29] Takashi Hamana, Masato Shirasaki, Satoshi Miyazaki, Chiaki Hikage, Masamune Oguri, et al. Cosmological constraints from cosmic shear two-point correlation functions with HSC survey first-year data. *Publications of the Astronomical Society of Japan*, 72(1):16, February 2020. doi: 10.1093/pasj/psz138.

[30] Catherine Heymans, Tilman Tröster, Marika Asgari, Chris Blake, Hendrik Hildebrandt, et al. KiDS-1000 Cosmology: Multi-probe weak gravitational lensing and spectroscopic galaxy clustering constraints. *Astronomy and Astrophysics*, 646:A140, February 2021. doi: 10.1051/0004-6361/202039063.

[31] T. M. C. Abbott, M. Aguena, A. Alarcon, S. Allam, O. Alves, et al. Dark Energy Survey Year 3 results: Cosmological constraints from galaxy clustering and weak lensing. *Phys. Rev. D*, 105(2):023520, January 2022. doi: 10.1103/PhysRevD.105.023520.

[32] A. Amon, D. Gruen, M. A. Troxel, N. MacCrann, S. Dodelson, et al. Dark Energy Survey Year 3 results: Cosmology from cosmic shear and robustness to data calibration. *Phys. Rev. D*, 105(2):023514, January 2022. doi: 10.1103/PhysRevD.105.023514.

[33] L. F. Secco, S. Samuroff, E. Krause, B. Jain, J. Blazek, et al. Dark Energy Survey Year 3 results: Cosmology from cosmic shear and robustness to modeling uncertainty. *Phys. Rev. D*, 105(2):023515, January 2022. doi: 10.1103/PhysRevD.105.023515.

[34] A. Porredon, M. Crocce, J. Elvin-Poole, R. Cawthon, G. Giannini, et al. Dark Energy Survey Year 3 results: Cosmological constraints from galaxy clustering and galaxy-galaxy lensing using the MAGLIM lens sample. *Phys. Rev. D*, 106(10):103530, November 2022. doi: 10.1103/PhysRevD.106.103530.

[35] S. Pandey, E. Krause, J. DeRose, N. MacCrann, B. Jain, et al. Dark Energy Survey year 3 results: Constraints on cosmological parameters and galaxy-bias models from galaxy clustering and galaxy-galaxy lensing using the redMaGiC sample. *Phys. Rev. D*, 106(4):043520, August 2022. doi: 10.1103/PhysRevD.106.043520.

[36] Rachel Mandelbaum. Weak Lensing for Precision Cosmology. *Annual Review of Astronomy and Astrophysics*, 56:393–433, September 2018. doi: 10.1146/annurev-astro-081817-051928.

[37] Eduardo J. Ruiz and Dragan Huterer. Testing the dark energy consistency with geometry and growth. *Physical Review D*, 91(6), March 2015. ISSN 1550-2368. doi: 10.1103/physrevd.91.063009. URL `http://dx.doi.org/10.1103/PhysRevD.91.063009`.

[38] Kunhao Zhong, Evan Saraivanov, Vivian Miranda, Jiachuan Xu, Tim Eifler, et al. Growth and geometry split in light of the des-y3 survey. *Physical Review D*, 107(12), June 2023. ISSN 2470-0029. doi: 10.1103/physrevd.107.123529. URL `http://dx.doi.org/10.1103/PhysRevD.107.123529`.

[39] D. N. Limber. The analysis of counts of the extragalactic nebulae in terms of a fluctuating density field. *The Astrophysical Journal*, 117: 134–139, 1953. doi: 10.1086/145672.

[40] Martin Kilbinger. Cosmology with cosmic shear observations: a review. *Reports on Progress in Physics*, 78(8):086901, July 2015. ISSN 1361-

6633. doi: 10.1088/0034-4885/78/8/086901. URL http://dx.doi.org/10.1088/0034-4885/78/8/086901.

[41] E. Krause, T. F. Eifler, J. Zuntz, O. Friedrich, M. A. Troxel, S. Dodelson, J. Blazek, L. F. Secco, N. MacCrann, E. Baxter, C. Chang, N. Chen, M. Crocce, J. DeRose, A. Ferte, N. Kokron, F. Lacasa, V. Miranda, Y. Omori, A. Porredon, R. Rosenfeld, S. Samuroff, M. Wang, R. H. Wechsler, T. M. C. Abbott, F. B. Abdalla, S. Allam, J. Annis, K. Bechtol, A. Benoit-Levy, G. M. Bernstein, D. Brooks, D. L. Burke, D. Capozzi, M. Carrasco Kind, J. Carretero, C. B. D'Andrea, L. N. da Costa, C. Davis, D. L. DePoy, S. Desai, H. T. Diehl, J. P. Dietrich, A. E. Evrard, B. Flaugher, P. Fosalba, J. Frieman, J. Garcia-Bellido, E. Gaztanaga, T. Giannantonio, D. Gruen, R. A. Gruendl, J. Gschwend, G. Gutierrez, K. Honscheid, D. J. James, T. Jeltema, K. Kuehn, S. Kuhlmann, O. Lahav, M. Lima, M. A. G. Maia, M. March, J. L. Marshall, P. Martini, F. Menanteau, R. Miquel, R. C. Nichol, A. A. Plazas, A. K. Romer, E. S. Rykoff, E. Sanchez, V. Scarpine, R. Schindler, M. Schubnell, I. Sevilla-Noarbe, M. Smith, M. Soares-Santos, F. Sobreira, E. Suchyta, M. E. C. Swanson, G. Tarle, D. L. Tucker, V. Vikram, A. R. Walker, and J. Weller. Dark Energy Survey Year 1 Results: Multi-Probe Methodology and Simulated Likelihood Analyses. *arXiv e-prints*, art. arXiv:1706.09359, June 2017.

[42] O. Friedrich, F. Andrade-Oliveira, H. Camacho, O. Alves, R. Rosenfeld, et al. Dark Energy Survey year 3 results: covariance modelling and its impact on parameter estimation and quality of fit. *Mon. Not. of the Royal Astron. Soc.*, 508(3):3125–3165, December 2021. doi: 10.1093/mnras/stab2384.

[43] DESI Collaboration, A. G. Adame, J. Aguilar, S. Ahlen, S. Alam, D. M. Alexander, C. Allende Prieto, M. Alvarez, O. Alves, A. Anand, U. Andrade, E. Armengaud, S. Avila, A. Aviles, H. Awan, B. Bahr-Kalus, S. Bailey, C. Baltay, A. Bault, J. Behera, S. BenZvi, F. Beutler, D. Bianchi, C. Blake, R. Blum, M. Bonici, S. Brieden, A. Brodzeller, D. Brooks, E. Buckley-Geer, E. Burtin, R. Calderon, R. Canning, A. Carnero Rosell, R. Cereskaite, J. L. Cervantes-Cota, S. Chabanier, E. Chaussidon, J. Chaves-Montero, D. Chebat, S. Chen, X. Chen, T. Claybaugh, S. Cole, A. Cuceu, T. M. Davis, K. Dawson, A. de la Macorra, A. de Mattia, N. Deiosso, A. Dey, B. Dey, Z. Ding, P. Doel, J. Edelstein, S. Eftekharzadeh, D. J. Eisenstein, W. Elbers, A. Elliott, P. Fagrelius, K. Fanning, S. Ferraro, J. Ereza, N. Findlay, B. Flaugher, A. Font-Ribera, D. Forero-Sánchez, J. E. Forero-Romero, C. S. Frenk,

C. Garcia-Quintero, L. H. Garrison, E. Gaztañaga, H. Gil-Marín, S. Gontcho A Gontcho, A. X. Gonzalez-Morales, V. Gonzalez-Perez, C. Gordon, D. Green, D. Gruen, R. Gsponer, G. Gutierrez, J. Guy, B. Hadzhiyska, C. Hahn, M. M. S Hanif, H. K. Herrera-Alcantar, K. Honscheid, C. Howlett, D. Huterer, V. Iršič, M. Ishak, R. Joyce, S. Juneau, N. G. Karaçaylı, R. Kehoe, S. Kent, D. Kirkby, H. Kong, S. E. Koposov, A. Kremin, A. Krolewski, O. Lahav, Y. Lai, T. W. Lan, M. Landriau, D. Lang, J. Lasker, J. M. Le Goff, L. Le Guillou, A. Leauthaud, M. E. Levi, T. S. Li, K. Lodha, C. Magneville, M. Manera, D. Margala, P. Martini, W. Matthewson, M. Maus, P. McDonald, L. Medina-Varela, A. Meisner, J. Mena-Fernández, R. Miquel, J. Moon, S. Moore, J. Moustakas, N. Mudur, E. Mueller, A. Muñoz-Gutiérrez, A. D. Myers, S. Nadathur, L. Napolitano, R. Neveux, J. A. Newman, N. M. Nguyen, J. Nie, G. Niz, H. E. Noriega, N. Padmanabhan, E. Paillas, N. Palanque-Delabrouille, J. Pan, S. Penmetsa, W. J. Percival, M. M. Pieri, M. Pinon, C. Poppett, A. Porredon, F. Prada, A. Pérez-Fernández, I. Pérez-Ràfols, D. Rabinowitz, A. Raichoor, C. Ramírez-Pérez, S. Ramirez-Solano, M. Rashkovetskyi, C. Ravoux, M. Rezaie, J. Rich, A. Rocher, C. Rockosi, N. A. Roe, A. Rosado-Marin, A. J. Ross, G. Rossi, R. Ruggeri, V. Ruhlmann-Kleider, L. Samushia, E. Sanchez, C. Saulder, E. F. Schlafly, D. Schlegel, M. Schubnell, H. Seo, A. Shafieloo, R. Sharples, J. Silber, A. Slosar, A. Smith, D. Sprayberry, T. Tan, G. Tarlé, P. Taylor, S. Trusov, R. Vaisakh, D. Valcin, F. Valdes, G. Valogiannis, M. Vargas-Magaña, L. Verde, M. Walther, B. Wang, M. S. Wang, B. A. Weaver, N. Weaverdyck, R. H. Wechsler, D. H. Weinberg, M. White, M. J. Wilson, L. Yi, J. Yu, Y. Yu, S. Yuan, C. Yèche, E. A. Zaborowski, P. Zarrouk, H. Zhang, C. Zhao, R. Zhao, R. Zhou, T. Zhuang, and H. Zou. Desi 2024 vii: Cosmological constraints from the full-shape modeling of clustering measurements, 2024. URL `https://arxiv.org/abs/2411.12022`.

[44] Andrew Gelman and Donald B. Rubin. Inference from Iterative Simulation Using Multiple Sequences. *Statistical Science*, 7:457–472, January 1992. doi: 10.1214/ss/1177011136.

[45] Diego Blas, Julien Lesgourgues, and Thomas Tram. The Cosmic Linear Anisotropy Solving System (CLASS). Part II: Approximation schemes. *Journal of Cosmology and Astroparticle Physics*, 2011(7):034, July 2011. doi: 10.1088/1475-7516/2011/07/034.

[46] J. S. Bagla. Cosmological n-body simulation: Techniques, scope and status, 2004. URL `https://arxiv.org/abs/astro-ph/0411043`.

[47] Ryuichi Takahashi, Naoki Yoshida, Masahiro Takada, Takahiko Matsubara, Naoshi Sugiyama, Issha Kayo, Atsushi J. Nishizawa, Takahiro Nishimichi, Shun Saito, and Atsushi Taruya. Simulations of baryon acoustic oscillations. ii. covariance matrix of the matter power spectrum. *The Astrophysical Journal*, 700(1):479–490, July 2009. ISSN 1538-4357. doi: 10.1088/0004-637x/700/1/479. URL `http://dx.doi.org/10.1088/0004-637X/700/1/479`.

[48] Francisco Villaescusa-Navarro, Sigurd Naess, Shy Genel, Andrew Pontzen, Benjamin Wandelt, et al. Statistical properties of paired fixed fields. *The Astrophysical Journal*, 867(2):137, nov 2018. doi: 10.3847/1538-4357/aae52b. URL `https://doi.org/10.3847%2F1538-4357%2Faae52b`.

[49] Raul E. Angulo and Andrew Pontzen. Cosmological N-body simulations with suppressed variance. *Mon. Not. Roy. Astron. Soc.*, 462(1):L1–L5, 2016. doi: 10.1093/mnrasl/slw098.

[50] Svetlin Tassev, Matias Zaldarriaga, and Daniel Eisenstein. Solving Large Scale Structure in Ten Easy Steps with COLA. *JCAP*, 06:036, 2013. doi: 10.1088/1475-7516/2013/06/036.

[51] Svetlin Tassev, Daniel J. Eisenstein, Benjamin D. Wandelt, and Matias Zaldarriaga. sCOLA: The N-body COLA Method Extended to the Spatial Domain. *arXiv e-prints*, art. arXiv:1502.07751, February 2015. doi: 10.48550/arXiv.1502.07751.

[52] Aurel Schneider, Romain Teyssier, Doug Potter, Joachim Stadel, Julian Onions, et al. Matter power spectrum and the challenge of percent accuracy. *JCAP*, 04:047, 2016. doi: 10.1088/1475-7516/2016/04/047.

[53] Euclid Collaboration, M. Knabenhans, J. Stadel, D. Potter, J. Dakin, et al. Euclid preparation: IX. EuclidEmulator2 - power spectrum emulation with massive neutrinos and self-consistent dark energy perturbations. *Mon. Not. Royal Astron. Soc.*, 505(2):2840–2869, August 2021. doi: 10.1093/mnras/stab1366.

[54] Raul E. Angulo, Matteo Zennaro, Sergio Contreras, Giovanni Aricò, Marcos Pellejero-Ibañez, and Jens Stücker. The BACCO simulation project: exploiting the full power of large-scale structure for cosmology. *Mon. Notices Royal Astron. Soc.*, 507(4):5869–5881, November 2021. doi: 10.1093/mnras/stab2018.

[55] Daniel Baumann, Daniel Green, and Benjamin Wallisch. Searching for light relics with large-scale structure. *Journal of Cosmology and Astroparticle Physics*, 2018(8):029, August 2018. doi: 10.1088/1475-7516/2018/08/029.

[56] Vivian Poulin, Tristan L. Smith, Tanvi Karwal, and Marc Kamionkowski. Early dark energy can resolve the hubble tension. *Physical Review Letters*, 122(22), jun 2019. doi: 10.1103/physrevlett.122.221301. URL https://doi.org/10.1103%2Fphysrevlett.122.221301.

[57] J. Colin Hill, Erminia Calabrese, Simone Aiola, Nicholas Battaglia, Boris Bolliet, Steve K. Choi, Mark J. Devlin, Adriaan J. Duivenvoorden, Jo Dunkley, Simone Ferraro, Patricio A. Gallardo, Vera Gluscevic, Matthew Hasselfield, Matt Hilton, Adam D. Hincks, René e Hložek, Brian J. Koopman, Arthur Kosowsky, Adrien La Posta, Thibaut Louis, Mathew S. Madhavacheril, Jeff McMahon, Kavilan Moodley, Sigurd Naess, Umberto Natale, Federico Nati, Laura Newburgh, Michael D. Niemack, Lyman A. Page, Bruce Partridge, Frank J. Qu, Maria Salatino, Alessandro Schillaci, Neelima Sehgal, Blake D. Sherwin, Cristóbal Sifón, David N. Spergel, Suzanne T. Staggs, Emilie R. Storer, Alexander van Engelen, Eve M. Vavagiakis, Edward J. Wollack, and Zhilei Xu. Atacama cosmology telescope: Constraints on prerecombination early dark energy. *Physical Review D*, 105(12), jun 2022. doi: 10.1103/physrevd.105.123536. URL https://doi.org/10.1103%2Fphysrevd.105.123536.

[58] J. Colin Hill, Evan McDonough, Michael W. Toomey, and Stephon Alexander. Early dark energy does not restore cosmological concordance. *Physical Review D*, 102(4), aug 2020. doi: 10.1103/physrevd.102.043507. URL https://doi.org/10.1103%2Fphysrevd.102.043507.

[59] Steven J. Clark, Kyriakos Vattis, JiJi Fan, and Savvas M. Koushiappas. The H_0 and S_8 tensions necessitate early and late time changes to ΛCDM. *arXiv e-prints*, art. arXiv:2110.09562, October 2021.

[60] Eleonora Di Valentino, Alessandro Melchiorri, Olga Mena, and Sunny Vagnozzi. Interacting dark energy in the early 2020s: A promising solution to the H_0 and cosmic shear tensions. *Physics of the Dark Universe*, 30:100666, dec 2020. doi: 10.1016/j.dark.2020.100666. URL https://doi.org/10.1016%2Fj.dark.2020.100666.

[61] Tanvi Karwal, Marco Raveri, Bhuvnesh Jain, Justin Khoury, and Mark Trodden. Chameleon early dark energy and the hubble tension. *Physical*

Review D, 105(6), mar 2022. doi: 10.1103/physrevd.105.063535. URL https://doi.org/10.1103%2Fphysrevd.105.063535.

[62] Jordan Stevens, Hasti Khoraminezhad, and Shun Saito. Constraining the spatial curvature with cosmic expansion history in a cosmological model with a non-standard sound horizon. *arXiv e-prints*, art. arXiv:2212.09804, December 2022. doi: 10.48550/arXiv.2212.09804.

[63] Emanuele Fondi, Alessandro Melchiorri, and Luca Pagano. No evidence for EDE from Planck data in extended scenarios. *arXiv e-prints*, art. arXiv:2203.12930, March 2022. doi: 10.48550/arXiv.2203.12930.

[64] Hao Wang and Yun-Song Piao. Testing dark energy after pre-recombination early dark energy. *Physics Letters B*, 832:137244, sep 2022. doi: 10.1016/j.physletb.2022.137244. URL https://doi.org/10.1016%2Fj.physletb.2022.137244.

[65] Alexander Reeves, Laura Herold, Sunny Vagnozzi, Blake D. Sherwin, and Elisa G. M. Ferreira. Restoring cosmological concordance with early dark energy and massive neutrinos?, 2022. URL https://arxiv.org/abs/2207.01501.

[66] Adrià Gómez-Valent, Ziyang Zheng, Luca Amendola, Christof Wetterich, and Valeria Pettorino. Coupled and uncoupled early dark energy, massive neutrinos, and the cosmological tensions. , 106(10):103522, November 2022. doi: 10.1103/PhysRevD.106.103522.

[67] Gen Ye and Yun-Song Piao. Is the Hubble tension a hint of AdS phase around recombination? *Phys. Rev. D*, 101(8):083507, April 2020. doi: 10.1103/PhysRevD.101.083507.

[68] Gen Ye, Jun Zhang, and Yun-Song Piao. Alleviating both H_0 and S_8 tensions: early dark energy lifts the CMB-lockdown on ultralight axion. *arXiv e-prints*, art. arXiv:2107.13391, July 2021. doi: 10.48550/arXiv.2107.13391.

[69] João Rebouças, Jonathan Gordon, Diogo H.F. de Souza, Kunhao Zhong, Vivian Miranda, Rogerio Rosenfeld, Tim Eifler, and Elisabeth Krause. Early dark energy constraints with late-time expansion marginalization. *Journal of Cosmology and Astroparticle Physics*, 2024(02):042, February 2024. ISSN 1475-7516. doi: 10.1088/1475-7516/2024/02/042. URL http://dx.doi.org/10.1088/1475-7516/2024/02/042.

[70] Vivian Poulin, Tristan L. Smith, Daniel Grin, Tanvi Karwal, and Marc Kamionkowski. Cosmological implications of ultralight axionlike fields. *Physical Review D*, 98(8), oct 2018. doi: 10.1103/physrevd.98.083525. URL https://doi.org/10.1103%2Fphysrevd.98.083525.

[71] Anton Chudaykin, Dmitry Gorbunov, and Nikita Nedelko. Combined analysis of planck and SPTPol data favors the early dark energy models. *Journal of Cosmology and Astroparticle Physics*, 2020(08):013–013, aug 2020. doi: 10.1088/1475-7516/2020/08/013. URL https://doi.org/10.1088%2F1475-7516%2F2020%2F08%2F013.

[72] Wayne Hu. Parametrized post-friedmann signatures of acceleration in the CMB. *Physical Review D*, 77(10), may 2008. doi: 10.1103/physrevd.77.103524. URL https://doi.org/10.1103%2Fphysrevd.77.103524.

[73] N. Aghanim, Y. Akrami, M. Ashdown, J. Aumont, C. Baccigalupi, M. Ballardini, A. J. Banday, R. B. Barreiro, N. Bartolo, S. Basak, R. Battye, K. Benabed, J.-P. Bernard, M. Bersanelli, P. Bielewicz, J. J. Bock, J. R. Bond, J. Borrill, F. R. Bouchet, F. Boulanger, M. Bucher, C. Burigana, R. C. Butler, E. Calabrese, J.-F. Cardoso, J. Carron, A. Challinor, H. C. Chiang, J. Chluba, L. P. L. Colombo, C. Combet, D. Contreras, B. P. Crill, F. Cuttaia, P. de Bernardis, G. de Zotti, J. Delabrouille, J.-M. Delouis, E. Di Valentino, J. M. Diego, O. Doré , M. Douspis, A. Ducout, X. Dupac, S. Dusini, G. Efstathiou, F. Elsner, T. A. Enßlin, H. K. Eriksen, Y. Fantaye, M. Farhang, J. Fergusson, R. Fernandez-Cobos, F. Finelli, F. Forastieri, M. Frailis, A. A. Fraisse, E. Franceschi, A. Frolov, S. Galeotta, S. Galli, K. Ganga, R. T. Génova-Santos, M. Gerbino, T. Ghosh, J. González-Nuevo, K. M. Górski, S. Gratton, A. Gruppuso, J. E. Gudmundsson, J. Hamann, W. Handley, F. K. Hansen, D. Herranz, S. R. Hildebrandt, E. Hivon, Z. Huang, A. H. Jaffe, W. C. Jones, A. Karakci, E. Keihänen, R. Keskitalo, K. Kiiveri, J. Kim, T. S. Kisner, L. Knox, N. Krachmalnicoff, M. Kunz, H. Kurki-Suonio, G. Lagache, J.-M. Lamarre, A. Lasenby, M. Lattanzi, C. R. Lawrence, M. Le Jeune, P. Lemos, J. Lesgourgues, F. Levrier, A. Lewis, M. Liguori, P. B. Lilje, M. Lilley, V. Lindholm, M. López-Caniego, P. M. Lubin, Y.-Z. Ma, J. F. Macías-Pérez, G. Maggio, D. Maino, N. Mandolesi, A. Mangilli, A. Marcos-Caballero, M. Maris, P. G. Martin, M. Martinelli, E. Martínez-González, S. Matarrese, N. Mauri, J. D. McEwen, P. R. Meinhold, A. Melchiorri, A. Mennella, M. Migliaccio, M. Millea, S. Mitra, M.-A. Miville-Deschênes, D. Molinari, L. Montier, G. Morgante, A. Moss, P. Natoli, H. U. Nørgaard-Nielsen, L. Pagano, D. Paoletti, B. Partridge, G. Patanchon, H. V. Peiris, F. Perrotta, V. Pet-

torino, F. Piacentini, L. Polastri, G. Polenta, J.-L. Puget, J. P. Rachen, M. Reinecke, M. Remazeilles, A. Renzi, G. Rocha, C. Rosset, G. Roudier, J. A. Rubiño-Martín, B. Ruiz-Granados, L. Salvati, M. Sandri, M. Savelainen, D. Scott, E. P. S. Shellard, C. Sirignano, G. Sirri, L. D. Spencer, R. Sunyaev, A.-S. Suur-Uski, J. A. Tauber, D. Tavagnacco, M. Tenti, L. Toffolatti, M. Tomasi, T. Trombetti, L. Valenziano, J. Valiviita, B. Van Tent, L. Vibert, P. Vielva, F. Villa, N. Vittorio, B. D. Wandelt, I. K. Wehus, M. White, S. D. M. White, A. Zacchei, and A. Zonca. Planck 2018 results. vi. cosmological parameters. *Astronomy & Astrophysics*, 641:A6, sep 2020. doi: 10.1051/0004-6361/201833910. URL https://doi.org/10.1051%2F0004-6361%2F201833910.

[74] D. M. Scolnic, D. O. Jones, A. Rest, Y. C. Pan, R. Chornock, R. J. Foley, M. E. Huber, R. Kessler, G. Narayan, A. G. Riess, S. Rodney, E. Berger, D. J. Brout, P. J. Challis, M. Drout, D. Finkbeiner, R. Lunnan, R. P. Kirshner, N. E. Sanders, E. Schlafly, S. Smartt, C. W. Stubbs, J. Tonry, W. M. Wood-Vasey, M. Foley, J. Hand, E. Johnson, W. S. Burgett, K. C. Chambers, P. W. Draper, K. W. Hodapp, N. Kaiser, R. P. Kudritzki, E. A. Magnier, N. Metcalfe, F. Bresolin, E. Gall, R. Kotak, M. McCrum, and K. W. Smith. The complete light-curve sample of spectroscopically confirmed SNe ia from pan-STARRS1 and cosmological constraints from the combined pantheon sample. *The Astrophysical Journal*, 859(2):101, may 2018. doi: 10.3847/1538-4357/aab9bb. URL https://doi.org/10.3847%2F1538-4357%2Faab9bb.

[75] Florian Beutler, Chris Blake, Matthew Colless, D. Heath Jones, Lister Staveley-Smith, Lachlan Campbell, Quentin Parker, Will Saunders, and Fred Watson. The 6df galaxy survey: baryon acoustic oscillations and the local hubble constant. *Monthly Notices of the Royal Astronomical Society*, 416(4):3017–3032, jul 2011. doi: 10.1111/j.1365-2966.2011.19250.x. URL https://doi.org/10.1111%2Fj.1365-2966.2011.19250.x.

[76] Ashley J. Ross, Lado Samushia, Cullan Howlett, Will J. Percival, Angela Burden, and Marc Manera. The clustering of the SDSS DR7 main galaxy sample – i. a 4 per cent distance measure at z = 0.15. *Monthly Notices of the Royal Astronomical Society*, 449(1):835–847, mar 2015. doi: 10.1093/mnras/stv154. URL https://doi.org/10.1093%2Fmnras%2Fstv154.

[77] Shadab Alam, Metin Ata, Stephen Bailey, Florian Beutler, Dmitry Bizyaev, Jonathan A. Blazek, Adam S. Bolton, Joel R. Brownstein, Angela Burden, Chia-Hsun Chuang, Johan Comparat, Antonio J. Cuesta, Kyle S. Dawson, Daniel J. Eisenstein, Stephanie Escoffier, Hé ctor

Gil-Marín, Jan Niklas Grieb, Nick Hand, Shirley Ho, Karen Kinemuchi, David Kirkby, Francisco Kitaura, Elena Malanushenko, Viktor Malanushenko, Claudia Maraston, Cameron K. McBride, Robert C. Nichol, Matthew D. Olmstead, Daniel Oravetz, Nikhil Padmanabhan, Nathalie Palanque-Delabrouille, Kaike Pan, Marcos Pellejero-Ibanez, Will J. Percival, Patrick Petitjean, Francisco Prada, Adrian M. Price-Whelan, Beth A. Reid, Sergio A. Rodríguez-Torres, Natalie A. Roe, Ashley J. Ross, Nicholas P. Ross, Graziano Rossi, Jose Alberto Rubiño-Martín, Shun Saito, Salvador Salazar-Albornoz, Lado Samushia, Ariel G. Sánchez, Siddharth Satpathy, David J. Schlegel, Donald P. Schneider, Claudia G. Scóccola, Hee-Jong Seo, Erin S. Sheldon, Audrey Simmons, Anže Slosar, Michael A. Strauss, Molly E. C. Swanson, Daniel Thomas, Jeremy L. Tinker, Rita Tojeiro, Mariana Vargas Magaña, Jose Alberto Vazquez, Licia Verde, David A. Wake, Yuting Wang, David H. Weinberg, Martin White, W. Michael Wood-Vasey, Christophe Yèche, Idit Zehavi, Zhongxu Zhai, and Gong-Bo Zhao. The clustering of galaxies in the completed SDSS-III baryon oscillation spectroscopic survey: cosmological analysis of the DR12 galaxy sample. *Monthly Notices of the Royal Astronomical Society*, 470(3):2617–2652, mar 2017. doi: 10.1093/mnras/stx721. URL `https://doi.org/10.1093%2Fmnras%2Fstx721`.

[78] T. M. C. Abbott, F. B. Abdalla, A. Alarcon, J. Aleksić, S. Allam, S. Allen, A. Amara, J. Annis, J. Asorey, S. Avila, D. Bacon, E. Balbinot, M. Banerji, N. Banik, W. Barkhouse, M. Baumer, E. Baxter, K. Bechtol, M. R. Becker, A. Benoit-Lévy, B. A. Benson, G. M. Bernstein, E. Bertin, J. Blazek, S. L. Bridle, D. Brooks, D. Brout, E. Buckley-Geer, D. L. Burke, M. T. Busha, A. Campos, D. Capozzi, A. Carnero Rosell, M. Carrasco Kind, J. Carretero, F. J. Castander, R. Cawthon, C. Chang, N. Chen, M. Childress, A. Choi, C. Conselice, R. Crittenden, M. Crocce, C. E. Cunha, C. B. D'Andrea, L. N. da Costa, R. Das, T. M. Davis, C. Davis, J. De Vicente, D. L. DePoy, J. DeRose, S. Desai, H. T. Diehl, J. P. Dietrich, S. Dodelson, P. Doel, A. Drlica-Wagner, T. F. Eifler, A. E. Elliott, F. Elsner, J. Elvin-Poole, J. Estrada, A. E. Evrard, Y. Fang, E. Fernandez, A. Ferté, D. A. Finley, B. Flaugher, P. Fosalba, O. Friedrich, J. Frieman, J. García-Bellido, M. Garcia-Fernandez, M. Gatti, E. Gaztanaga, D. W. Gerdes, T. Giannantonio, M. S. S. Gill, K. Glazebrook, D. A. Goldstein, D. Gruen, R. A. Gruendl, J. Gschwend, G. Gutierrez, S. Hamilton, W. G. Hartley, S. R. Hinton, K. Honscheid, B. Hoyle, D. Huterer, B. Jain, D. J. James, M. Jarvis, T. Jeltema, M. D. Johnson, M. W. G. Johnson, T. Kacprzak, S. Kent, A. G. Kim, A. King, D. Kirk, N. Kokron, A. Kovacs, E. Krause, C. Krawiec, A. Kremin,

K. Kuehn, S. Kuhlmann, N. Kuropatkin, F. Lacasa, O. Lahav, T. S. Li, A. R. Liddle, C. Lidman, M. Lima, H. Lin, N. MacCrann, M. A. G. Maia, M. Makler, M. Manera, M. March, J. L. Marshall, P. Martini, R. G. McMahon, P. Melchior, F. Menanteau, R. Miquel, V. Miranda, D. Mudd, J. Muir, A. Möller, E. Neilsen, R. C. Nichol, B. Nord, P. Nugent, R. L. C. Ogando, A. Palmese, J. Peacock, H. V. Peiris, J. Peoples, W. J. Percival, D. Petravick, A. A. Plazas, A. Porredon, J. Prat, A. Pujol, M. M. Rau, A. Refregier, P. M. Ricker, N. Roe, R. P. Rollins, A. K. Romer, A. Roodman, R. Rosenfeld, A. J. Ross, E. Rozo, E. S. Rykoff, M. Sako, A. I. Salvador, S. Samuroff, C. Sánchez, E. Sanchez, B. Santiago, V. Scarpine, R. Schindler, D. Scolnic, L. F. Secco, S. Serrano, I. Sevilla-Noarbe, E. Sheldon, R. C. Smith, M. Smith, J. Smith, M. Soares-Santos, F. Sobreira, E. Suchyta, G. Tarle, D. Thomas, M. A. Troxel, D. L. Tucker, B. E. Tucker, S. A. Uddin, T. N. Varga, P. Vielzeuf, V. Vikram, A. K. Vivas, A. R. Walker, M. Wang, R. H. Wechsler, J. Weller, W. Wester, R. C. Wolf, B. Yanny, F. Yuan, A. Zenteno, B. Zhang, Y. Zhang, J. Zuntz, and Dark Energy Survey Collaboration. Dark Energy Survey year 1 results: Cosmological constraints from galaxy clustering and weak lensing. , 98 (4):043526, August 2018. doi: 10.1103/PhysRevD.98.043526.

[79] T. M. C. Abbott, M. Aguena, A. Alarcon, S. Allam, O. Alves, A. Amon, F. Andrade-Oliveira, J. Annis, S. Avila, D. Bacon, E. Baxter, K. Bechtol, M. R. Becker, G. M. Bernstein, S. Bhargava, S. Birrer, J. Blazek, A. Brandao-Souza, S. L. Bridle, D. Brooks, E. Buckley-Geer, D. L. Burke, H. Camacho, A. Campos, A. Carnero Rosell, M. Carrasco Kind, J. Carretero, F. J. Castander, R. Cawthon, C. Chang, A. Chen, R. Chen, A. Choi, C. Conselice, J. Cordero, M. Costanzi, M. Crocce, L. N. da Costa, M. E. da Silva Pereira, C. Davis, T. M. Davis, J. De Vicente, J. DeRose, S. Desai, E. Di Valentino, H. T. Diehl, J. P. Dietrich, S. Dodelson, P. Doel, C. Doux, A. Drlica-Wagner, K. Eckert, T. F. Eifler, F. Elsner, J. Elvin-Poole, S. Everett, A. E. Evrard, X. Fang, A. Farahi, E. Fernandez, I. Ferrero, A. Ferté, P. Fosalba, O. Friedrich, J. Frieman, J. García-Bellido, M. Gatti, E. Gaztanaga, D. W. Gerdes, T. Giannantonio, G. Giannini, D. Gruen, R. A. Gruendl, J. Gschwend, G. Gutierrez, I. Harrison, W. G. Hartley, K. Herner, S. R. Hinton, D. L. Hollowood, K. Honscheid, B. Hoyle, E. M. Huff, D. Huterer, B. Jain, D. J. James, M. Jarvis, N. Jeffrey, T. Jeltema, A. Kovacs, E. Krause, R. Kron, K. Kuehn, N. Kuropatkin, O. Lahav, P.-F. Leget, P. Lemos, A. R. Liddle, C. Lidman, M. Lima, H. Lin, N. MacCrann, M. A. G. Maia, J. L. Marshall, P. Martini, J. McCullough, P. Melchior, J. Mena-Fernández, F. Menanteau, R. Miquel, J. J. Mohr, R. Morgan,

J. Muir, J. Myles, S. Nadathur, A. Navarro-Alsina, R. C. Nichol, R. L. C. Ogando, Y. Omori, A. Palmese, S. Pandey, Y. Park, F. Paz-Chinchón, D. Petravick, A. Pieres, A. A. Plazas Malagón, A. Porredon, J. Prat, M. Raveri, M. Rodriguez-Monroy, R. P. Rollins, A. K. Romer, A. Roodman, R. Rosenfeld, A. J. Ross, E. S. Rykoff, S. Samuroff, C. Sánchez, E. Sanchez, J. Sanchez, D. Sanchez Cid, V. Scarpine, M. Schubnell, D. Scolnic, L. F. Secco, S. Serrano, I. Sevilla-Noarbe, E. Sheldon, T. Shin, M. Smith, M. Soares-Santos, E. Suchyta, M. E. C. Swanson, M. Tabbutt, G. Tarle, D. Thomas, C. To, A. Troja, M. A. Troxel, D. L. Tucker, I. Tutusaus, T. N. Varga, A. R. Walker, N. Weaverdyck, R. Wechsler, J. Weller, B. Yanny, B. Yin, Y. Zhang, and J. Zuntz and. Dark energy survey year 3 results: Cosmological constraints from galaxy clustering and weak lensing. *Physical Review D*, 105(2), jan 2022. doi: 10.1103/physrevd.105.023520. URL `https://doi.org/10.1103%2Fphysrevd.105.023520`.

[80] S. H. Suyu, V. Bonvin, F. Courbin, C. D. Fassnacht, C. E. Rusu, D. Sluse, T. Treu, K. C. Wong, M. W. Auger, X. Ding, S. Hilbert, P. J. Marshall, N. Rumbaugh, A. Sonnenfeld, M. Tewes, O. Tihhonova, A. Agnello, R. D. Blandford, G. C. F. Chen, T. Collett, L. V. E. Koopmans, K. Liao, G. Meylan, and C. Spiniello. H0LiCOW - I. H_0 Lenses in COSMOGRAIL's Wellspring: program overview. *Mon. Not. of the R. Astron. Soc.*, 468(3):2590–2604, July 2017. doi: 10.1093/mnras/stx483.

[81] V. Bonvin, F. Courbin, S. H. Suyu, P. J. Marshall, C. E. Rusu, D. Sluse, M. Tewes, K. C. Wong, T. Collett, C. D. Fassnacht, T. Treu, M. W. Auger, S. Hilbert, L. V. E. Koopmans, G. Meylan, N. Rumbaugh, A. Sonnenfeld, and C. Spiniello. H0LiCOW - V. New COSMOGRAIL time delays of HE 0435-1223: H_0 to 3.8 per cent precision from strong lensing in a flat ΛCDM model. *Mon. Not. of the R. Astron. Soc.*, 465 (4):4914–4930, March 2017. doi: 10.1093/mnras/stw3006.

[82] Kenneth C Wong, Sherry H Suyu, Geoff C-F Chen, Cristian E Rusu, Martin Millon, Dominique Sluse, Vivien Bonvin, Christopher D Fassnacht, Stefan Taubenberger, Matthew W Auger, Simon Birrer, James H H Chan, Frederic Courbin, Stefan Hilbert, Olga Tihhonova, Tommaso Treu, Adriano Agnello, Xuheng Ding, Inh Jee, Eiichiro Komatsu, Anowar J Shajib, Alessandro Sonnenfeld, Roger D Blandford, Lé on V E Koopmans, Philip J Marshall, and Georges Meylan. H0licow – XIII. a 2.4 per cent measurement of h0 from lensed quasars: 5.3σ tension between early- and late-universe probes. *Monthly Notices of the Royal Astronom-*

ical Society, 498(1):1420–1439, sep 2019. doi: 10.1093/mnras/stz3094. URL https://doi.org/10.1093%2Fmnras%2Fstz3094.

[83] V Miranda, P Rogozenski, and E Krause. Interpreting internal consistency of DES measurements. *Monthly Notices of the Royal Astronomical Society*, 509(4):5218–5230, oct 2021. doi: 10.1093/mnras/stab3068. URL https://doi.org/10.1093%2Fmnras%2Fstab3068.

[84] Jesú s Torrado and Antony Lewis. Cobaya: code for bayesian analysis of hierarchical physical models. *Journal of Cosmology and Astroparticle Physics*, 2021(05):057, may 2021. doi: 10.1088/1475-7516/2021/05/057. URL https://doi.org/10.1088%2F1475-7516%2F2021%2F05%2F057.

[85] Elisabeth Krause and Tim Eifler. cosmolike - cosmological likelihood analyses for photometric galaxy surveys. *Monthly Notices of the Royal Astronomical Society*, 470(2):2100–2112, may 2017. doi: 10.1093/mnras/stx1261. URL https://doi.org/10.1093%2Fmnras%2Fstx1261.

[86] Ryuichi Takahashi, Masanori Sato, Takahiro Nishimichi, Atsushi Taruya, and Masamune Oguri. Revising the Halofit Model for the Nonlinear Matter Power Spectrum. *Astrophys. J.*, 761:152, 2012. doi: 10.1088/0004-637X/761/2/152.

[87] L. Casarini, S.A. Bonometto, E. Tessarotto, and P.-S. Corasaniti. Extending the coyote emulator to dark energy models with standard $w_0 - w_a$ parametrization of the equation of state. *Journal of Cosmology and Astroparticle Physics*, 2016(08):008–008, aug 2016. doi: 10.1088/1475-7516/2016/08/008. URL https://doi.org/10.1088%2F1475-7516%2F2016%2F08%2F008.

[88] Luciano Casarini, Andrea V Macciò , and Silvio A Bonometto. Dynamical dark energy simulations: high accuracy power spectra at high redshift. *Journal of Cosmology and Astroparticle Physics*, 2009(03):014–014, mar 2009. doi: 10.1088/1475-7516/2009/03/014. URL https://doi.org/10.1088%2F1475-7516%2F2009%2F03%2F014.

[89] Adam G. Riess, Louise Breuval, Wenlong Yuan, Stefano Casertano, Lucas M. Macri, Dan Scolnic, Tristan Cantat-Gaudin, Richard I. Anderson, and Mauricio Cruz Reyes. Cluster cepheids with high precision gaia parallaxes, low zeropoint uncertainties, and hubble space telescope photometry, 2022. URL https://arxiv.org/abs/2208.01045.

[90] Mikhail M. Ivanov, Evan McDonough, J. Colin Hill, Marko Simonović , Michael W. Toomey, Stephon Alexander, and Matias Zaldarriaga. Constraining early dark energy with large-scale structure. *Physical Review D*, 102(10), nov 2020. doi: 10.1103/physrevd.102.103502. URL `https://doi.org/10.1103%2Fphysrevd.102.103502`.

[91] LSST Science Collaboration, Paul A. Abell, Julius Allison, Scott F. Anderson, John R. Andrew, et al. LSST Science Book, Version 2.0. *arXiv e-prints*, art. arXiv:0912.0201, December 2009. doi: 10.48550/arXiv.0912.0201.

[92] Luca Amendola, Stephen Appleby, Anastasios Avgoustidis, David Bacon, Tessa Baker, et al. Cosmology and fundamental physics with the Euclid satellite. *Living Reviews in Relativity*, 21(1):2, April 2018. doi: 10.1007/s41114-017-0010-3.

[93] F. Bernardeau, S. Colombi, E. Gaztañaga, and R. Scoccimarro. Large-scale structure of the Universe and cosmological perturbation theory. *Physics Reports*, 367(1-3):1–248, September 2002. doi: 10.1016/S0370-1573(02)00135-7.

[94] Patrick McDonald. Clustering of dark matter tracers: Renormalizing the bias parameters. , 74(10):103512, November 2006. doi: 10.1103/PhysRevD.74.103512.

[95] Patrick McDonald and Arabindo Roy. Clustering of dark matter tracers: generalizing bias for the coming era of precision LSS. *Journal of Cosmology and Astroparticle Physics*, 2009(8):020, August 2009. doi: 10.1088/1475-7516/2009/08/020.

[96] Daniel Baumann, Alberto Nicolis, Leonardo Senatore, and Matias Zaldarriaga. Cosmological non-linearities as an effective fluid. *Journal of Cosmology and Astroparticle Physics*, 2012(7):051, July 2012. doi: 10.1088/1475-7516/2012/07/051.

[97] John Joseph M. Carrasco, Mark P. Hertzberg, and Leonardo Senatore. The effective field theory of cosmological large scale structures. *Journal of High Energy Physics*, 2012:82, September 2012. doi: 10.1007/JHEP09(2012)082.

[98] Zvonimir Vlah, Martin White, and Alejandro Aviles. A Lagrangian effective field theory. *Journal of Cosmology and Astroparticle Physics*, 2015 (9):014–014, September 2015. doi: 10.1088/1475-7516/2015/09/014.

[99] Leonardo Senatore and Matias Zaldarriaga. The IR-resummed Effective Field Theory of Large Scale Structures. *Journal of Cosmology and Astroparticle Physics*, 2015(2):013–013, February 2015. doi: 10.1088/1475-7516/2015/02/013.

[100] Tobias Baldauf, Mehrdad Mirbabayi, Marko Simonović, and Matias Zaldarriaga. Equivalence principle and the baryon acoustic peak. , 92(4): 043514, August 2015. doi: 10.1103/PhysRevD.92.043514.

[101] Matthew Lewandowski and Leonardo Senatore. An analytic implementation of the IR-resummation for the BAO peak. *Journal of Cosmology and Astroparticle Physics*, 2020(3):018, March 2020. doi: 10.1088/1475-7516/2020/03/018.

[102] Anton Chudaykin, Mikhail M. Ivanov, Oliver H. E. Philcox, and Marko Simonović. Nonlinear perturbation theory extension of the Boltzmann code CLASS. *Phys. Rev. D*, 102(6):063533, 2020. doi: 10.1103/PhysRevD.102.063533.

[103] Shi-Fan Chen, Zvonimir Vlah, and Martin White. Consistent Modeling of Velocity Statistics and Redshift-Space Distortions in One-Loop Perturbation Theory. *JCAP*, 07:062, 2020. doi: 10.1088/1475-7516/2020/07/062.

[104] Guido D'Amico, Leonardo Senatore, and Pierre Zhang. Limits on wCDM from the EFTofLSS with the PyBird code. *Journal of Cosmology and Astroparticle Physics*, 2021(1):006, January 2021. doi: 10.1088/1475-7516/2021/01/006.

[105] Alejandro Aviles, Arka Banerjee, Gustavo Niz, and Zachary Slepian. Clustering in massive neutrino cosmologies via Eulerian Perturbation Theory. *JCAP*, 11:028, 2021. doi: 10.1088/1475-7516/2021/11/028.

[106] Hernán E. Noriega, Alejandro Aviles, Sebastien Fromenteau, and Mariana Vargas-Magaña. Fast computation of non-linear power spectrum in cosmologies with massive neutrinos. *JCAP*, 11:038, 2022. doi: 10.1088/1475-7516/2022/11/038.

[107] Chiara Moretti, Maria Tsedrik, Pedro Carrilho, and Alkistis Pourtsidou. Modified gravity and massive neutrinos: constraints from the full shape analysis of BOSS galaxies and forecasts for Stage IV surveys. *JCAP*, 12: 025, 2023. doi: 10.1088/1475-7516/2023/12/025.

[108] Anton Chudaykin, Konstantin Dolgikh, and Mikhail M. Ivanov. Constraints on the curvature of the Universe and dynamical dark energy from the Full-shape and BAO data. *Phys. Rev. D*, 103(2):023507, 2021. doi: 10.1103/PhysRevD.103.023507.

[109] Guido D'Amico, Yaniv Donath, Leonardo Senatore, and Pierre Zhang. Limits on Clustering and Smooth Quintessence from the EFTofLSS. *arXiv e-prints*, art. arXiv:2012.07554, December 2020. doi: 10.48550/arXiv.2012.07554.

[110] Aaron Glanville, Cullan Howlett, and Tamara M. Davis. Full-shape galaxy power spectra and the curvature tension. *Mon. Not. Roy. Astron. Soc.*, 517(2):3087–3100, 2022. doi: 10.1093/mnras/stac2891.

[111] Lorenzo Piga, Marco Marinucci, Guido D'Amico, Massimo Pietroni, Filippo Vernizzi, and Bill S. Wright. Constraints on modified gravity from the BOSS galaxy survey. *JCAP*, 04:038, 2023. doi: 10.1088/1475-7516/2023/04/038.

[112] R. E. Smith, J. A. Peacock, A. Jenkins, S. D. M. White, C. S. Frenk, et al. Stable clustering, the halo model and nonlinear cosmological power spectra. *Mon. Not. Roy. Astron. Soc.*, 341:1311, 2003. doi: 10.1046/j.1365-8711.2003.06503.x.

[113] Simeon Bird, Matteo Viel, and Martin G. Haehnelt. Massive Neutrinos and the Non-linear Matter Power Spectrum. *Mon. Not. Roy. Astron. Soc.*, 420:2551–2561, 2012. doi: 10.1111/j.1365-2966.2011.20222.x.

[114] Alexander Mead, John Peacock, Catherine Heymans, Shahab Joudaki, and Alan Heavens. An accurate halo model for fitting non-linear cosmological power spectra and baryonic feedback models. *Mon. Not. Roy. Astron. Soc.*, 454(2):1958–1975, 2015. doi: 10.1093/mnras/stv2036.

[115] Alexander Mead, Catherine Heymans, Lucas Lombriser, John Peacock, Olivia Steele, et al. Accurate halo-model matter power spectra with dark energy, massive neutrinos and modified gravitational forces. *Mon. Not. Roy. Astron. Soc.*, 459(2):1468–1488, 2016. doi: 10.1093/mnras/stw681.

[116] A. J. Mead, S. Brieden, T. Tröster, and C. Heymans. HMCODE-2020: improved modelling of non-linear cosmological power spectra with baryonic feedback. *Monthly Notices of the Royal Astronomical Society*, 502 (1):1401–1422, March 2021. doi: 10.1093/mnras/stab082.

[117] M. Cataneo, L. Lombriser, C. Heymans, A. J. Mead, A. Barreira, et al. On the road to percent accuracy: non-linear reaction of the matter power spectrum to dark energy and modified gravity. *Mon. Not. of the Royal Astron. Soc*, 488(2):2121–2142, September 2019. doi: 10.1093/mnras/stz1836.

[118] Benjamin Bose, Bill S. Wright, Matteo Cataneo, Alkistis Pourtsidou, Carlo Giocoli, et al. On the road to per cent accuracy - V. The non-linear power spectrum beyond ΛCDM with massive neutrinos and baryonic feedback. *Mon. Not. of the Royal Astron. Soc*, 508(2):2479–2491, December 2021. doi: 10.1093/mnras/stab2731.

[119] Guilherme Brando, Bartolomeo Fiorini, Kazuya Koyama, and Hans A. Winther. Enabling matter power spectrum emulation in beyond-ΛCDM cosmologies with COLA. *Journal of Cosmology and Astroparticle Physics*, 2022(9):051, September 2022. doi: 10.1088/1475-7516/2022/09/051.

[120] Jonathan Gordon, Bernardo F. de Aguiar, João Rebouças, Guilherme Brando, Felipe Falciano, Vivian Miranda, Kazuya Koyama, and Hans A. Winther. Modeling nonlinear scales with cola: preparing for lsst-y1, 2024. URL `https://arxiv.org/abs/2404.12344`.

[121] Albert Izard, Martin Crocce, and Pablo Fosalba. ICE-COLA: Towards fast and accurate synthetic galaxy catalogues optimizing a quasi N-body method. *Mon. Not. Roy. Astron. Soc.*, 459(3):2327–2341, 2016. doi: 10.1093/mnras/stw797.

[122] Jun Koda, Chris Blake, Florian Beutler, Eyal Kazin, and Felipe Marin. Fast and accurate mock catalogue generation for low-mass galaxies. *Mon. Not. Roy. Astron. Soc.*, 459(2):2118–2129, 2016. doi: 10.1093/mnras/stw763.

[123] Bartolomeo Fiorini, Kazuya Koyama, and Tessa Baker. Fast production of cosmological emulators in modified gravity: the matter power spectrum. *JCAP*, 12:045, 2023. doi: 10.1088/1475-7516/2023/12/045.

[124] Hans A. Winther, Kazuya Koyama, Marc Manera, Bill S. Wright, and Gong-Bo Zhao. COLA with scale-dependent growth: applications to screened modified gravity models. *JCAP*, 08:006, 2017. doi: 10.1088/1475-7516/2017/08/006.

[125] J. Adamek et al. Euclid: Modelling massive neutrinos in cosmology – a code comparison. *JCAP*, 06:035, 2023. doi: 10.1088/1475-7516/2023/06/035.

[126] Georgios Valogiannis and Rachel Bean. Efficient simulations of large scale structure in modified gravity cosmologies with comoving Lagrangian acceleration. *Phys. Rev. D*, 95(10):103515, 2017. doi: 10.1103/PhysRevD.95.103515.

[127] Hans Winther, Santiago Casas, Marco Baldi, Kazuya Koyama, Baojiu Li, et al. Emulators for the nonlinear matter power spectrum beyond ΛCDM. *Phys. Rev. D*, 100(12):123540, 2019. doi: 10.1103/PhysRevD.100.123540.

[128] Guilherme Brando, Kazuya Koyama, and Hans A. Winther. Revisiting Vainshtein screening for fast N-body simulations. *JCAP*, 06:045, 2023. doi: 10.1088/1475-7516/2023/06/045.

[129] Renate Mauland, Hans A. Winther, and Cheng-Zong Ruan. Sesame: A power spectrum emulator pipeline for beyond-ΛCDM models. *arXiv e-prints*, 9 2023.

[130] Nesar Ramachandra, Georgios Valogiannis, Mustapha Ishak, and Katrin Heitmann. Matter Power Spectrum Emulator for f(R) Modified Gravity Cosmologies. *Phys. Rev. D*, 103(12):123525, 2021. doi: 10.1103/PhysRevD.103.123525.

[131] Bill S. Wright, Ashim Sen Gupta, Tessa Baker, Georgios Valogiannis, Bartolomeo Fiorini, and LSST Dark Energy Science Collaboration. Hi-COLA: fast, approximate simulations of structure formation in Horndeski gravity. *Journal of Cosmology and Astroparticle Physics*, 2023(3):040, March 2023. doi: 10.1088/1475-7516/2023/03/040.

[132] Raul E. Angulo and Oliver Hahn. Large-scale dark matter simulations. *Living Reviews in Computational Astrophysics*, 8(1), feb 2022. doi: 10.1007/s41115-021-00013-z. URL `https://doi.org/10.1007%2Fs41115-021-00013-z`.

[133] Christian Fidler, Thomas Tram, Cornelius Rampf, Robert Crittenden, Kazuya Koyama, et al. Relativistic initial conditions for N-body simulations. *JCAP*, 06:043, 2017. doi: 10.1088/1475-7516/2017/06/043.

[134] Thomas Tram, Jacob Brandbyge, Jeppe Dakin, and Steen Hannestad. Fully relativistic treatment of light neutrinos in N-body simulations. *JCAP*, 03:022, 2019. doi: 10.1088/1475-7516/2019/03/022.

[135] Guilherme Brando, Kazuya Koyama, and David Wands. Relativistic Corrections to the Growth of Structure in Modified Gravity. *JCAP*, 01: 013, 2021. doi: 10.1088/1475-7516/2021/01/013.

[136] The LSST Dark Energy Science Collaboration, Rachel Mandelbaum, Tim Eifler, Renée Hložek, Thomas Collett, et al. The LSST Dark Energy Science Collaboration (DESC) Science Requirements Document. *arXiv e-prints*, art. arXiv:1809.01669, September 2018. doi: 10.48550/arXiv.1809.01669.

[137] E. Krause, X. Fang, S. Pandey, L. F. Secco, O. Alves, et al. Dark energy survey year 3 results: Multi-probe modeling strategy and validation, 2021.

[138] Pedro Carrilho, Chiara Moretti, and Maria Tsedrik. Probing solutions to the s_8 tension with galaxy clustering, 2023. URL `https://arxiv.org/abs/2310.07344`.

[139] Vivian Poulin, José Luis Bernal, Ely D. Kovetz, and Marc Kamionkowski. Sigma-8 tension is a drag. *Physical Review D*, 107(12), June 2023. ISSN 2470-0029. doi: 10.1103/physrevd.107.123538. URL `http://dx.doi.org/10.1103/PhysRevD.107.123538`.

[140] Itamar J. Allali, Mark P. Hertzberg, and Fabrizio Rompineve. Dark sector to restore cosmological concordance. *Phys. Rev. D*, 104:L081303, Oct 2021. doi: 10.1103/PhysRevD.104.L081303. URL `https://link.aps.org/doi/10.1103/PhysRevD.104.L081303`.

[141] Melissa Joseph, Daniel Aloni, Martin Schmaltz, Eashwar N. Sivarajan, and Neal Weiner. A Step in Understanding the S_8 Tension. *arXiv e-prints*, art. arXiv:2207.03500, July 2022.